AN ABSTRACT OF THE THESIS OF

Hilary F. Stockdon for the degree of Master of Science in Oceanography. Presented on August 15, 1997. Title: Estimation of Wave Phase Speed and Nearshore Bathymetry Using Video Techniques.

Redacted for privacy

Abstract approved:___

Robert A. Holman

The beach profile is a very important part of the nearshore system in that it serves as the bottom boundary condition for all fluid dynamics in the region. Nonlinear evolution of the incident wave field, the forcing of mean currents in the longshore and cross-shore directions, and the generation of low frequency infragravity waves are all dependent on the details of the nearshore bathymetry. In addition, the offshore profile represents the sediment response to overlying fluid motions.

The nature of the offshore bathymetry has been shown to be complex and unstable in both time and space. In order to resolve this detail, accurate, frequent, and long-term measurements are needed of offshore water depths. Historically, the collection of bathymetric profiles in the nearshore has been logistically difficult and even dangerous due to high wave conditions. In this paper, a video technique for the estimation of offshore bathymetry is offered as an alternative to the more traditional surveying approaches. Ideally, this technique would be capable of easily providing much needed bathymetric data for accurate modeling of nearshore fluid dynamics and measuring of profile response.

In this technique, video data are digitally collected in the form of pixel intensity time series at locations evenly spaced in the cross-shore. Phase relationships for the propagating wave signal are obtained from the intensity time series using a frequency domain EOF analysis over the incident band. Based on the phase lag and the distance

between pixel sensors spaced in both the cross-shore and longshore directions, the vector wavenumber is calculated. Phase speed is then determined at the incident frequency, and bathymetry is inferred along the array using linear wave theory's dispersion relationship. Weekly averaged profiles were calculated from a suite of estimates made along a cross-shore transect. The median water depth at each point provided the most accurate single representation of the multiple estimates at each cross-shore location. Error bars around the estimates were determined from the standard deviation of all the estimates at each location in the profile.

The technique was used to estimated nearshore bathymetry at two beaches in Duck, North Carolina and Agate Beach, Oregon. The weighted, mean RMS difference error for the estimated profile at Duck was 0.67 m over an eleven week period of study. The time-averaged mean ratio error was 1.34 over the eleven week period indicating that the results of the video technique are accurate to within approximately 34% of the true water depth. At Agate Beach, the estimated profiles were remarkably consistent and stable throughout the eleven week study period. Estimated beach slopes were very reasonable and consistent with beach slopes previously observed at the site ($\beta = 0.01$). While ground truth is not available for this site, a comparison of an estimated sand bar location to video time exposures of waves breaking over a sand bar indicate that the profiles may serve as a good first order approximation of the bathymetry at this high energy beach.

Estimation of Wave Phase Speed and Nearshore Bathymetry Using Video Techniques

by

Hilary F. Stockdon

A Thesis

submitted to

Oregon State University

In partial fulfillment of
the requirements for the
degree of

Master of Science

Completed August 15, 1997
Commencement June 1998

Master of Science thesis of Hilary F. Stockdon presented on August 15, 1997

Approved:

Redacted for privacy

Major Professor, representing Oceanography

Redacted for privacy

Dean of College of Oceanic and Atmospheric Sciences

Redacted for privacy

Dean of Graduate School

I understand that my thesis will become part of the permanent collection of Oregon State University Libraries. My signature below authorizes release of my thesis to any reader upon request.

Redacted for privacy

Hilary F. Stockdon, Author

ACKNOWLEDGMENTS

This research would not have been possible without the support, patience, guidance, and encouragement of many people. I would first like to thank my major professor Rob Holman. He gave me the chance of a lifetime - to study the beach, to do good science, to see the world, and to make some wonderful friends. Through Rob, I have really learned how to think - something that is much harder to do than I had previously imagined. I will never forget the importance of "using first principles" or "being gutsy." I would also like to thank the other members of my committee, Jim Good, Paul Komar, and Richard Daniels, for their reviews of my thesis and their insightful comments on my research.

I would like to extend my gratitude to all of the CIL family - past and present. All of you have touched my life in so many ways. Thank you to Peter Howd for introducing me to the study of beaches and waves and for getting me hooked. Diane has always been a wonderful role model. She has been so amazingly supportive and has helped me through some rough and scary times. Todd has also been a good friend and has given me much needed encouragement. He helped me to understand the basics of all this video stuff that we do. And Tom, the other video genius, has given me tons of technical and scientific advice, helping me to work through many confusing details during the development of this technique. Nathaniel has always been there to talk about science and statistics. He is always full of good ideas - sometimes, more ideas that I can handle at one time! He has been a calming presence on our lab, helping us to relax and reminding us to go to the beach more often than we do. I would also like to thank John for getting me out of many a predicament, for fixing everything that broke, choked, died or "got lost." I appreciate him not only for his computer wizardry but also for his songs, jokes, and occasional magic tricks. A huge thanks go out to the extremely dedicated undergrads - Eric, Amanda, Justin and Adam - who have helped us all out in CIL and kept me laughing and having fun. I would especially like to thank Amanda for she has been so helpful and sweet during the last few months and has always been there for me when I needed her. The Weniger crowd - Babs, Jack, Kathelijne, and Kathy - have given me much moral support and scientific

advice and kept me smiling through some of the hardest times. Thank you all for being such good friends. I know for a fact that this CIL family is one of the strongest groups around - I will never forget any of you or how you all have helped me over the last three years.

My friends here in Corvallis have added tremendously to my life. I would first like to thank Katie and Kathy. They have been such dear friends to me and have really taken care of me when things got tough. They are the sweetest, most genuine friends anyone could ever ask for. I would also like to thank Julie, Carrie, Maren, and Lynne for a longstanding tradition that gave me something to look forward to every week - getting together with all of you for good food and lively conversation. Rob, Emily, Peter, Brendan, Pete, Dave, and Barbara - thank you, for being so much fun to be around! I will certainly never forget all of the wonderful people I have met during my time in Corvallis.

I extend a heartfelt thanks to Greg for being so supportive of everything I have done. He has been a best friend to me through thick and thin. He has taught me some very important "lessons for life" that have made me a stronger person - believe in yourself, believe in others, stay cool, and good things are bound to happen. Thank you, Greg, for helping me to see the best in everything!

I would finally like thank my wonderful family because without them, I never would have made it this far. They have always provided me with a strong foundation and encouraged me to pursue my dreams. Through them I have learned to find worth and value in each little success, and then use it to help you through the more difficult times. All of their love and support have made me the person I am today. So I dedicate this thesis to them - Kathy, Peter, Ben, and Max – one amazing family!

This work was funded by a grant from the Office of Naval Research Coastal Dynamics Program (Grant #N00014-9610237). Survey and wave data from Duck, NC were provided by the staff at the U.S. Army Corps of Engineers Field Research Facility.

TABLE OF CONTENTS

Page

1. INTRODUCTION 1

1.1 The Importance of the Offshore Profile 2

1.2 Temporal and Spatial Variability of the Profile 4

1.3 Collection of Bathymetric Data 8

2. BACKGROUND 12

2.1 Measurement of Wave Phase Speed 13

2.2 Video Techniques 15

3. VIDEO TECHNIQUE FOR BATHYMETRY ESTIMATION 25

3.1 Estimation of Frequency 27

3.2 Estimation of Cross-shore Wavenumber 29

3.3 Estimation of Longshore Wavenumber 31

4. FIELD TESTS 33

4.1 The Delilah Experiment - Duck, North Carolina 33

4.1.1 Sampling Design 36
4.1.2 Results of Video Technique 39

4.2 Duck, North Carolina Argus Station 52

4.2.1 Water Depth Analysis 53
4.2.2 Definitions of Statistics Describing Performance 57
4.2.3 Evaluation of Depth Estimators 62
4.2.4 Algorithm Performance 69

4.3 Agate Beach, Oregon Argus Station 75

4.3.1 Estimated Depths 78
4.3.2 Evaluation of Consistency of Estimates 78

5. DISCUSSION 87

TABLE OF CONTENTS (Continued)

Page

5.1 When to Expect Reliable Depth Estimates 87

5.2 Possible Explanations for Incorrect Estimates 89

5.2.1 Video Related Error 89
5.2.2 CEOF Related Error 90
5.2.3 Discrepancies Between Estimated and Theoretical Phase Speed 92

5.3 Future Work 93

6. CONCLUSION 95

BIBLIOGRAPHY 97

LIST OF FIGURES

Figure		Page
1.1	Winter/Summer profile (from Komar, 1976)	5
1.2	Plan and profile schematics of six beach morpho-dynamic beach states proposed by Wright and Short (1984).	6
1.3	Eleven time exposures representing the offshore morphology observed during the spring in Duck, North Carolina from 1987-1997.	9
2.1	Energy density, coherence, and phase calculated from two spatially separated current meters as a part of the Nearshore Sediment Transport Study, November 4, 1978 (from Thornton and Guza, 1982).	16
2.2	Energy density, coherence, and celerity spectra for current meters C22 (light line) and C23 (heavy line), November 20, 1978 (from Thornton and Guza, 1982).	17
2.3	Celerity spectra at different water depths for narrow banded waves on November 20, 1978 (from Thornton and Guza, 1982).	18
2.4	Example co-located pressure (top) and video intensity (bottom) time series from October 12, 1990 (from Lippmann and Holman, 1991).	21
2.5	Cross-spectrum between a video intensity time series and an in-situ pressure gauge from the mid-surf zone (from Lippmann and Holman, 1991).	22
2.6	Amplitude, coherence, phase, and celerity spectra between time series collected from sensors separated 18m in the cross-shore for both pressure (left column) and intensity data (right column) (from Lippmann and Holman, 1991).	23
3.1	Sensitivity analysis of the dispersion relation based on deep water wavelength	26
3.2	Timestack of a synthetic time series for a shoaling 10 second wave.	28
3.3	Synthetic series test for the extraction of cross-shore wavenumber.	32
4.1	Offshore profile surveyed at Duck, North Carolina on October 8, 1990.	34
4.2	Map of the field site in Duck, North Carolina..	35
4.3	Pixel array for the Delilah experiment, Duck, North Carolina	37

LIST OF FIGURES (Continued)

Figure		Page
4.4	Intensity timestack from Duck, North Carolina, October 8, 1990 at 1612 GMT..	38
4.5	Frequency-space spectra of intensity data from October 8, 1990 at 1612 GMT.	40
4.6	Frequency-space coherence between adjacent pixel sensors from October 8, 1997 at 1612 GMT.	41
4.7	Frequency-space celerity spectra between adjacent pixel sensors from October 8, 1997 at 1612 GMT..	43
4.8	Cross-spectra between two pixels located over the trough, October 8, 1990 at 1612 GMT: log spectral density (a), coherence (b), phase (c), and celerity spectrum (d).	44
4.9	Cross-spectra between two pixels located over the sand bar, October 8, 1990 at 1612 GMT: log spectral density (a), coherence (b), phase (c), and celerity spectra (d).	46
4.10	CEOF results for October 8, 1997 at 1612 GMT	47
4.11	Wave angle (a) and water depth (b) estimates for October 8, 1990 at 1612 GMT.	48
4.12	Mean (a) and variance (b) of pixel intensity at each cross-shore position for October 8, 1990 at 1612 GMT.	50
4.13	Variations of depth estimates from October 8, 1990 at x = 142.5 m (a) and x = 152.5 m (b) through a tidal cycle	51
4.14	CRAB surveyed profiles at Duck, North Carolina from April 4, 1997 to June 17, 1997	54
4.15	Significant wave height, wave period, and wave angle measured in 8 m water depth in Duck, North Carolina from April 1 to June 17, 1997.	55
4.16	Pixel array for the Argus Station in Duck, North Carolina.	56
4.17	Estimated offshore profile at Duck, North Carolina for April 8, 1997.	63
4.18	Estimated offshore profile at Duck, North Carolina for May 6, 1997.	64

LIST OF FIGURES (Continued)

Figure		Page
4.19	Estimated depth error versus true water depth	70
4.20	Estimated depth error versus beach slope.	71
4.21	Estimated depths error versus the cross-shore gradient in mean intensity.	73
4.22	Estimated depth error versus standard deviation of intensity, std(I)	74
4.23	Oblique (a) and rectified (b) time exposure from Agate Beach, Oregon on April 4, 1997	76
4.24	Pixel array for the Argus station in Agate Beach, Oregon	77
4.25	Estimated profiles at Agate Beach, Oregon from April 11 to June 6, 1997	79
4.26	Time-space map of estimated profiles at Agate Beach, Oregon from April 1 to June 16, 1997	80
4.27	Rectified time exposure (a) and estimated profile (b) from Agate Beach, Oregon on April 11, 1997	82
4.28	Rectified time exposure (a) and estimated profile (b) from Agate Beach, Oregon on April 25, 1997	83
4.29	Time series of depth estimates at six cross-shore positions at Agate Beach, Oregon	84
4.30	Time-space map of estimated confidence intervals at Agate Beach, Oregon from April 4 – June 13, 1997	86
5.1	Amplitudes from the cross-spectral matrix of intensity data for October 8, 1990 in Duck, North Carolina	91

LIST OF TABLES

Table — Page

4.1.a. Mean Ratio ($\overline{R}$) 66

4.1.b. Weighted Mean Ratio ($\overline{R_w}$) 66

4.2.a. Mean Difference Error ($\overline{D}$) 67

4.2.b. Weighted Mean Difference Error ($\overline{D}_w$) 67

4.3.a. RMS Difference Errors (D_{rms}) 68

4.3.b. Weighted RMS Difference Errors (D_{w_rms}) 68

ESTIMATION OF WAVE PHASE SPEED AND NEARSHORE BATHYMETRY USING VIDEO TECHNIQUES

1. INTRODUCTION

The nearshore zone is the energetic area of the coastal environment where ocean waves shoal and interact with local morphology. It is an area of dramatic and rapid change as seen by our ever-varying eroding and accreting shorelines. This region is very important to many different groups for a variety of reasons ranging from recreational opportunities to economic investments to coastal zone management to national defense. Problems associated with coastal erosion impacts coupled with increased development along the oceans have created a strong need for knowledge of how this complex system behaves. Effective coastal management policy and sound, sustainable coastal development rely on a detailed understanding of the processes at work in this region in addition to accurate measurements of the specific changes in morphology occurring at a particular site. The measurement of bathymetry is critical to achieving both of the above goals. In a more applied sense, a collection of bathymetric surveys in one specific area can provide a measure of profile adjustment (i.e. erosion and accretion). Theoretically and scientifically, bathymetry measurements are essential for studying the fluid processes that are responsible for the movement of sand. The objective of the work presented in this paper is to develop an accurate and simple tool for collecting bathymetric survey data that can later be used for coastal management studies or as input into theoretical models of nearshore processes.

The dynamics of nearshore processes is composed of the interdependency of an evolving wave field over a shoaling bathymetry and the changes in that bathymetry as a result of those waves. As deep ocean waves propagate towards the shallow nearshore, their initially sinusoidal form become strongly nonlinear. As waves steepen and break, energy is shifted into higher frequencies [*Elgar and Guza*, 1985] associated with turbulent

motions and into lower frequencies associated with mean currents, undertow and infragravity waves (low frequency waves with periods on the order of 60 seconds). The evolution of the wave field and the types of fluid motions forced during wave shoaling are completely dependent on the existence and the shape of the local bathymetry since bathymetry acts as the bottom boundary condition for nearshore flows [*Holman, et al.*, 1993].

The bathymetry itself is constantly in flux, moving from one state to another depending on the wave conditions. Turbulent motions near the sediment-water interface and superimposed low frequency flows result in sediment suspension and transport in the surf zone. Subsequent changes in bathymetry can occur on time scales as short as hours to days (such as in the presence of large storm waves and increased infragravity energy) and on spatial scales on the order of meters to kilometers. The relationship becomes very complex as the evolution of the wave field now responds to an altered bathymetry.

Nonlinear feedback is associated with the potential for chaos and the development of complexity in the system (which is, in fact, observed). To understand naturally occurring nonlinear systems, the collection of a long time series of system behavior is required. This includes measurements of both the fluids and the sediments.

1.1 The Importance of the Offshore Profile

The offshore beach profile forms the bottom boundary condition for all fluid motions in the nearshore. The shoaling profile causes waves to steepen and eventually break, moving energy into higher frequencies and turbulence. Details of this breaking depend on the nature of the beach profile. On a planar beach, breaking will be distributed over a broad region while on a barred beach, breaking will be focused over the sand bar and on the shoreline with a quiet region between. Waves breaking at an angle to the beach carry with them a shoreward flux of longshore directed momentum, termed radiation stress, that

drives the longshore current [*Longuet-Higgins*, 1970]. Since longshore currents are driven by breaking waves, the predicted structure of the current will depend on the distribution of breaking. On barred beaches, this would imply that the largest longshore currents would be found along the sand bar where breaking is initiated. However, field experiments have shown that the greatest magnitudes of the current actually occur shoreward of the bar within the trough [*Whitford and Thornton*, 1988]. Thus, the profile is important in determining, in part, the location and strength of the longshore current.

The formation and characteristics of edge waves is also highly dependent on the local morphology. Edge waves are low frequency gravity waves that propagate parallel to the shoreline. They are the result refractive trapping of wave energy near the shoreline. The sloping profile acts as a wave guide that traps the edge wave within the surf zone [*Oltman-Shay and Howd*, 1993]. The characteristics of an edge wave are different depending on the types or slopes of the beach profile [*Holman and Bowen*, 1979]. On planar beaches, the amplitude of the edge wave is a maximum at the shoreline and decreases offshore. However, on complex topographies, studies have revealed that edge waves may also become trapped over offshore sand bars, concentrating energy along the bar rather than along the shore [*Bryan and Bowen*, 1996]. It is the offshore profile that determines the formation, location and persistence of edge waves. Theories and models involving mechanisms for edge wave growth and for the behavior of edge waves are heavily dependent on accurate measurements of the bathymetry.

Not only is the profile critical for all nearshore fluid dynamics, it is also important to sediment suspension and transport. For example, rip channels and offshore canyons act as conduits for the movement of sand offshore. Low lying rip and cusp embayments on the shoreline allow increased run-up [*Holland, et al.*, 1995] and, in turn, cause increased erosion in these areas. The presence of shallow depths over a sand bar cause increased breaking, turbulence and corresponding sediment suspension that could reinforce growth of the sand bar form. Finally, the profile is the actual quantitative measure of the beach response to overlying fluid motion. For many applications, such as coastal zone

management, the erosion and accretion of beach topography is the most important measure of beach response.

1.2 Temporal and Spatial Variability of the Profile

The beach profile is always in a state of flux in response to varying wave conditions. The shape of the profile acts to dissipate wave energy by causing waves to break. This then serves as a natural buffer for the shoreline from the action of waves. Early studies of profiles focused on an annual winter/summer cycle. In the winter, large storm waves remove sand from the shoreline and move it offshore to form sand bars (Figure 1.1). These sand bars serve to dissipate storm energy by making waves break further offshore. In the summer, gentle swell waves bring the sand back onshore to form a profile characterized by a wide berm and smooth offshore gradient [*Bascom*, 1954]. The transition between the two states has been found to be dependent on wave steepness, sediment settling rates and beach slope.

Wright and Short introduced more detailed descriptions of six beach states in which the shape of the profile was dependent upon not only wave conditions but also the pre-existing beach state since bathymetry plays a large role in altering fluid motions in the surf zone [*Wright and Short*, 1984]. The six beach states show morphology response to variations in incident waves, subharmonic oscillations, infragravity motions, mean currents and rip currents. The first state is that of a low sloping, dissipative beach on which incident waves are dissipated by breaking and low frequency infragravity motions are dominant. The other extreme state is a steeply sloping reflective beach which is dominated by incident wave energy. The intermediate states are characterized by a more complex offshore bathymetry marked by longshore variability, offshore bars, rips channels and beach cusps. Figure 1.2 presents the classical plan and profile diagrams of the beach states defined by Wright and Short. It includes brief descriptions of the wave conditions

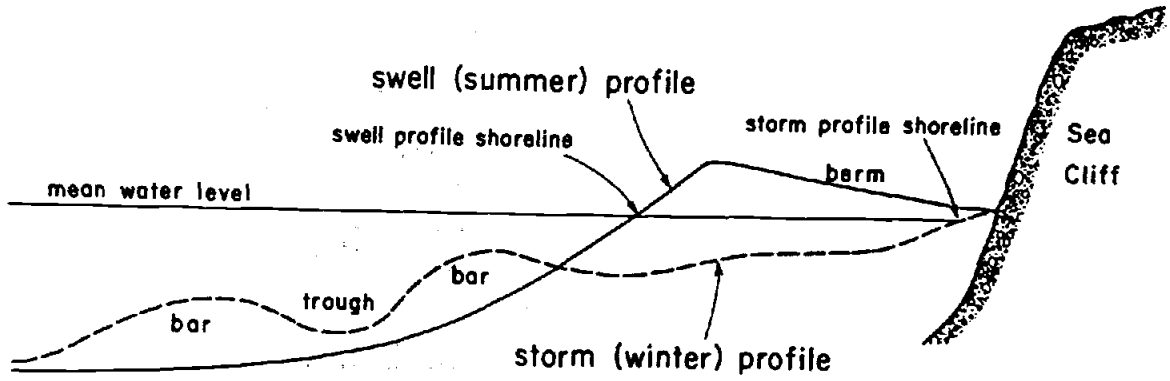

Figure 1.1 Winter/Summer profile (from Komar, 1976).

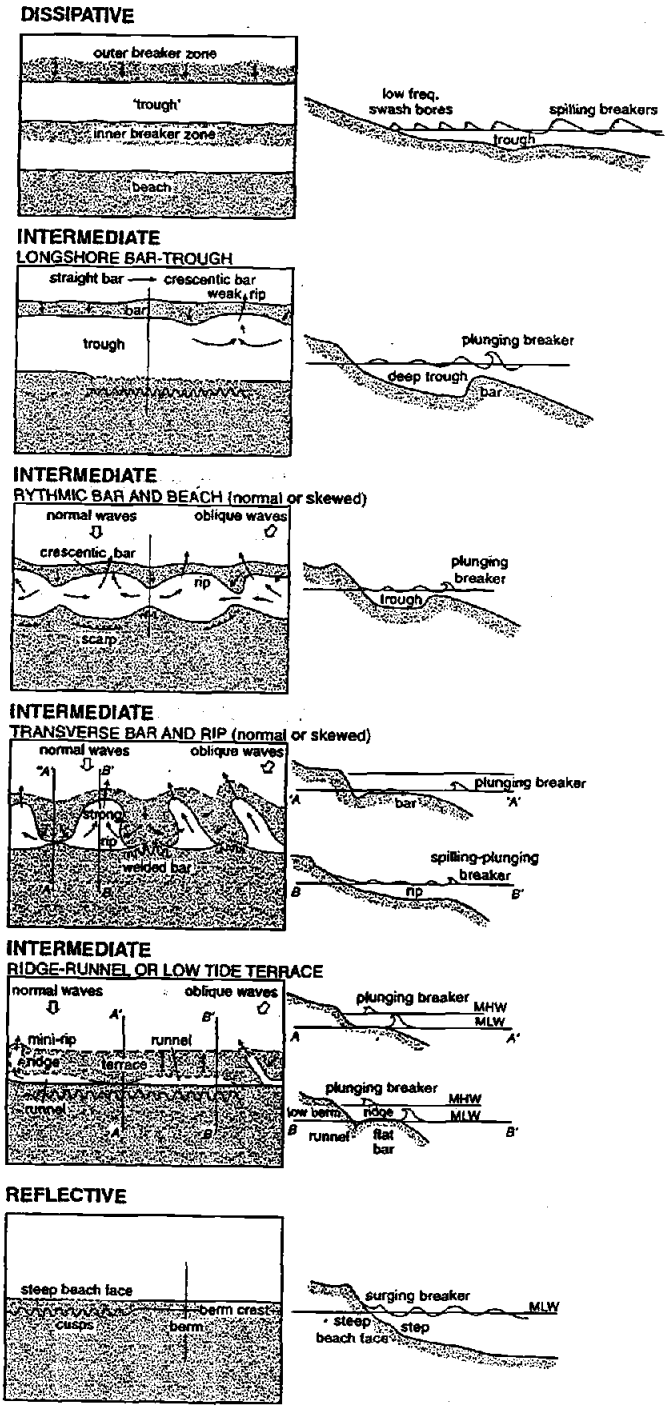

Figure 1.2 Plan and profile schematics of six beach morpho-dynamic beach states proposed by Wright and Short (1984).

generally observed for each state, as well as typical beach slopes and cross-shore scalings. This method of classification was intended to be used a type of 'yardstick' by which all beaches could be measured and compared. While this method of description of beach states is much more extensive than the summer/winter profile terminology, it is still limited in its abilities to classify beaches with more complex sand bar systems.

Lippmann and Holman devised an slightly modified classification scheme which allowed for a more objective quantification of both the temporal and spatial complexity of sand bar morphology [*Lippmann and Holman*, 1990]. Eight beach states were identified based on four objective criteria: absence/presence of a sand bar, incident/infragravity scaling of the sand bar, the presence and rhythmicity of longshore variability, and the existence of a continuous versus discontinuous trough. These process-driven states were then closely studied with respect to their stability and natural transition sequence (i.e., the ordering of states in erosional and accretional sequences). While this study resulted in an improved assessment of beach states, it also visually identified the complexity of the nearshore morphology.

In field experiments at the U.S. Army Corps of Engineer's Field Research Facility (FRF) in Duck, North Carolina, the complexity of the spatial and temporal scales of the offshore sand bars has been revealed through detailed three-dimensional offshore surveys conducted by the Coastal Research Amphibious Buggy (CRAB) [*Birkemeier and Mason*, 1984]. The CRAB is capable of resolving both cross-shore and longshore variability through densely spaced surveys covering a large area of the nearshore. For example, during the Delilah experiment in 1990, the CRAB performed daily surveys of a 525 m by 375 m region north of the pier [*Birkemeier, et al.*, 1991]. The detailed surveys conducted at the FRF provide proof that the system changes on a variety of temporal and spatial scales and also reveal the need for more detailed and long term studies at other sites. Unfortunately, the surveys conducted with the CRAB require a tremendous logistical effort and can only be conducted at the FRF.

The complexity of the offshore profile has been further revealed through video time exposures of the nearshore region at Duck, NC. The collection of ten-minute time exposures has allowed the visualization and quantification of nearshore morphology based on the breaking patterns of incident waves over shallow areas of the profile such as offshore sand bars [*Lippmann and Holman*, 1989]. Figure 1.3 presents eleven time exposures collected in using an Argus Station which consists of an unmanned video camera connected to a PC-based image processor [*Holman, et al.*, 1993]. The time exposures in this figure were all collected during the spring at Duck and represent eleven years of complex morphological changes. This series illustrates the interannual variability of the profile and provides further evidence of the nonlinear complexity of the system. The images suggest that the common assumption of an alongshore uniform profile may not be correct on all beaches. Since an accurate representation of bathymetry is critical to the understanding of nearshore processes, the three dimensional variability of the profile should be included in models to obtain a more complete representation of the system.

The interdependency between the fluid forcing and the sediment response is a topic of great importance in our understanding of the dynamics of the nearshore and the processes that cause accretion and erosion of beaches. In order to obtain a better understanding of the large scale interactions between the waves and sediment/morphology, it is necessary to have accurate measurements of both the wave field and the underlying topography. Previous studies of the offshore profile indicate that in order to resolve the complex nonlinear morphological changes observed in the nearshore region, large-scale, long-term data sets of bathymetry are desperately needed.

1.3 Collection of Bathymetric Data

Historically, the collection of offshore bathymetric profiles has been a costly and labor intensive task. This data may be difficult to collect during periods of large waves or strong currents. However, these conditions often represent the most energetic periods of

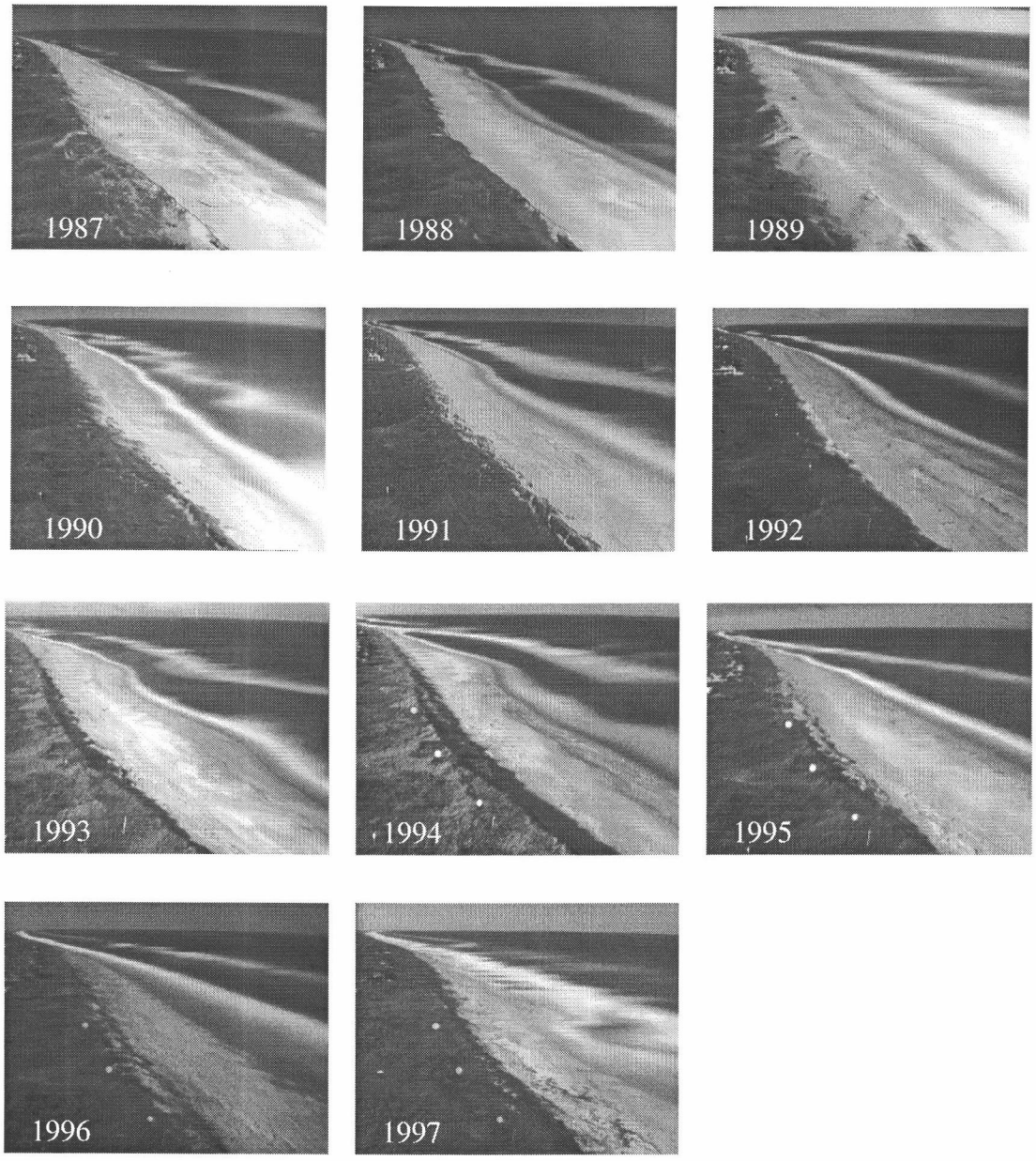

Figure 1.3 Eleven time exposures representing the offshore morphology observed during the spring in Duck, North Carolina from 1987-1997.

sediment transport and profile adjustment. Because of various difficulties in conducting nearshore bathymetric surveys, profile information is sparse and the depth data needed to test models for shoreline change and wave evolution, and even to reveal the range of natural complexity present, have not been available.

Here we present a technique that will allow for the regular and automatic collection of profile data over long periods of time. This paper describes a method for remotely measuring the underwater topography of the surf zone using data collected from video cameras. First, wave celerity, or wave phase speed, is measured from remotely collected video intensity data and then local water depth is inferred based on linear wave theory. The measurement of wave phase speed and associated water depths made at a series of cross-shore positions provides us with a cross-shore profile of beach morphology. These remotely collected profiles may create a long and complete record of the large scale morphology changes at a particular site, in addition to providing depth data for testing of various nearshore process models. Incorporation of the technique into the automated sampling routine of the well-established Argus Stations will allow for a more comprehensive and long-term sampling of nearshore bathymetry, a pre-requisite to the study of the large-scale behavior of profile response.

The collection of nearshore data using remote sensing video techniques has proven to be a valuable alternative to sampling using fixed instruments located within the surf zone. For example, Lippmann and Holman [1989] developed a video time exposure technique for quantifying morphological scales of sand bars based on wave breaking and dissipation. Holland et al. [1995] found a sensible relationship between observations of run-up measured using video techniques and those measured using the more traditional resistance-wire run-up method. Plant and Holman [in press] measured the slope of the foreshore by mapping video estimates of the shoreline position throughout the tidal cycle. These are just a few of the techniques that have shown video to be an accurate and appealing technique for measuring nearshore processes.

Remote sensing techniques are an attractive tool for measuring physical processes because they allow for sampling over large spatial (centimeters to kilometers) and temporal scales (seconds to years) [*Holland, et al.*, 1997]. Video techniques also have the advantage over traditional in-situ instrumentation in that they do not involve the deployment of any instruments into the surf zone and can be used to investigate a large range of wave conditions over a long period of time at a low cost [*Holman, et al.*, 1993]. Breaking waves and strong currents make in-situ sampling logistically difficult and may create a damaging environment to sensitive instrumentation. Another advantage of the remote sensing techniques is that the design of the spatial sampling arrays can be created or modified any time to suit the needs of the user. Hence, video techniques for bathymetry estimation allow more complete data sets to be used for the study of large-scale, long term profile change.

This thesis has two primary objectives. The first is to introduce a video-based technique for the estimation of bottom bathymetry. The second objective is to test estimates against ground truth data, describe the conditions under which accurate depth estimates are expected, and determine the confidence interval for that estimate. Chapter 2 provides a general background on wave phase speed and on the techniques that have been used to measure this quantity in the nearshore. In Chapter 3 the video technique for estimating bathymetry is discussed in detail. Chapter 4 presents the results of the video depth analysis from the Delilah experiment in Duck, North Carolina and from Argus Stations located at Duck, North Carolina and Agate Beach, Oregon. Chapter 5 presents a discussion of the accuracy of the technique and of the conditions under which it can best be applied. Chapter 6 contains a brief summary of the final conclusions of this research.

2. BACKGROUND

The phase speed of a wave is the speed with which a wave form propagates. It is distinct from the speed of propagation of wave energy, known as the group velocity. Phase speed can be calculated from the phase difference between wave records collected at two different points along the wave form [*Brillouin*, 1960]. For example, in the case of surface gravity waves, this signal can be sea surface elevation measurements from surface piercing wave staffs or sea level pressure measurements from pressure transducers.

The phase speed, or celerity, c, is defined as the wavelength, L, divided by the wave period, T, or equivalently,

$$c = \frac{\sigma}{k} \tag{2.1}$$

where the wavenumber, k, is defined as $2\pi/L$, and the radial frequency, σ, is defined as $2\pi/T$.

Airy wave theory, or linear wave theory, is the simplest small amplitude solution of a wave form. In this theory the wavenumber and frequency are related through the dispersion equation,

$$\sigma^2 = gk\tanh(kh) \tag{2.2}$$

where g is the acceleration of gravity and h is the local water depth. From equations (2.1) and (2.2) the celerity of a wave based on linear wave theory is

$$c = \frac{\sigma}{k} = \frac{g}{\sigma}\tanh(kh). \tag{2.3}$$

Approximations to the exact solution exist for wave propagating in deep and shallow water. As the depth becomes very large ($\tanh(kh) \sim 1$), we can define a simple deep water wavelength, L_o, to be

$$L_o = \frac{gT^2}{2\pi}. \tag{2.4}$$

The deep water approximations for phase speed is expressed as

$$c = \frac{g}{\sigma} = \frac{gT}{2\pi}, \tag{2.5}$$

which is valid for $h/L_o > 0.25$. In shallow water ($h/L_o < 0.05$), $\tanh(kh)$ is approximately equal to the argument (kh) and the phase speed of a wave simplifies to

$$c^2 = \frac{\sigma^2}{k^2} = gh \tag{2.6}$$

which is no longer dependent on the wave period but is solely a function of the depth of water through which the wave is propagating.

Linear theory is generally an adequate solution for wave propagation in the surf zone. However, higher order theories that account for finite amplitude effects may be more appropriate under large wave conditions [*Komar*, 1976]. Solitary wave theory is one example of a number of higher order theories. It is based on an asymptotic solution for the higher order Cnoidal wave theory in which the wave period approaches infinity. This solution describes a single progressive crest that has no oscillatory motions, no wave period and no wavelength [*Komar*, 1976]. The equation for the prediction of the phase speed of a solitary wave is

$$c = \sqrt{g(h+H)} \tag{2.7}$$

which accounts for finite amplitude by the inclusion of wave height, H. Local wave heights effectively increase the water depth causing waves to travel faster than would be predicted by simple linear theory. Waves traveling at the solitary phase speed are frequency non-dispersive and their phase speed is a function of local water depth and wave height.

2.1 Measurement of Wave Phase Speed

During W.W.II, scientists began to take a greater interest in studying wave propagation and phase speed in order to predict surf conditions in landing operations. In

the 1950's, techniques for measuring phase speed in the field were employed that were based on the movement of an identifiable feature of the wave, for example, a wave crest, past fixed points. Early measurements obtained using time-lapse aerial photography were based on the observation of individual wave crests passing a fixed point such as pilings at the end of a pier [*Fuchs*, 1953]. Long crested, high amplitude waves were critical to this study in that they created a well defined wave crest. It was found that super-imposed wind waves obscured smaller amplitude waves, making individual crests more difficult to identify [*Wiegel and Fuchs*, 1953].

A later technique involved the use of incremented wave poles placed across the breaker zone. Suhayda and Pettigrew [1977] investigated the phase speeds of individual breaking waves across the surf zone using photographs of the crests that were taken over a specified sampling interval. The average wave crest speed was then approximated by measuring the distance a particular wave crest had moved over the interval of time. The ratio of measured celerity to that predicted by solitary theory was found to increase as waves progressed from offshore towards the break point. Maximum discrepancies were observed at the break point where measured celerities were approximately 20% greater than those predicted by solitary theory and in the mid-surf zone where measured values were approximately 20% less than predicted values. Problems were noted in the visual determination of the wave crest due to the evolving shape of the wave. Errors in the calculation were also attributed to the fact that the speed of the crest does not represent the speed of the wave as a whole. This study alluded to the benefits of data collection using continually recording wave staffs and set the stage for more advanced measurement techniques which soon followed.

Eventually, wave phase speed calculations were made from data automatically collected from wave staffs or pressure sensors. As a part of the Nearshore Sediment Transport Study, Thornton and Guza [1982] used time series collected from current meters and pressure sensors to study wave phase speeds inside the surf zone. Using pairs of wave gauges aligned perpendicular to the beach, cross-spectra were calculated to

obtain information on the frequency dependent relative phase difference, $\phi(f)$, between the wave at the two sensor locations. The phase speed was then calculated between two adjacent sensors using the relationship

$$c_x = \frac{2\pi f \Delta x}{\phi(f)} \tag{2.8}$$

where c_x is the cross-shore component of phase speed and Δx is the spatial separation between sensor [*Thornton and Guza*, 1982]. For this particular study, the incident wave approach was approximately shore-normal, therefore the longshore component of phase speed could be ignored.

Example power, coherence, phase and celerity spectra calculated between adjacent sensor pairs are shown in Figures 2.1 and 2.2. From equation (2.8), it is seen that for shallow water non-dispersive shoreward propagating waves (constant c_x), wave phase must increase linearly with frequency (Figure 2.1, lower panel). The slope of this line could then be a robust estimate of celerity. The calculation of phase speed using this constant sloped phase ramp produces a constant speed at a particular cross-shore location across all frequencies in shallow water depths, indicating that the waves are frequency non-dispersive (Figure 2.2). Figure 2.3 present the celerity spectra calculated at various depths across the surf zone. Again, the estimated celerities are consistent with linear theory in that the phase speeds were frequency non-dispersive and traveled as a function of water depth. Some effects of finite amplitude can be observed in the measured phase speeds as some values are slightly greater than that predicted by linear theory.

2.2 Video Techniques

The speed of progressive waves may potentially be observable using video-based techniques. For this technique to be successful, two things must be true. First, waves must have a measurable visible signature. Second, the relationship of the visible signature

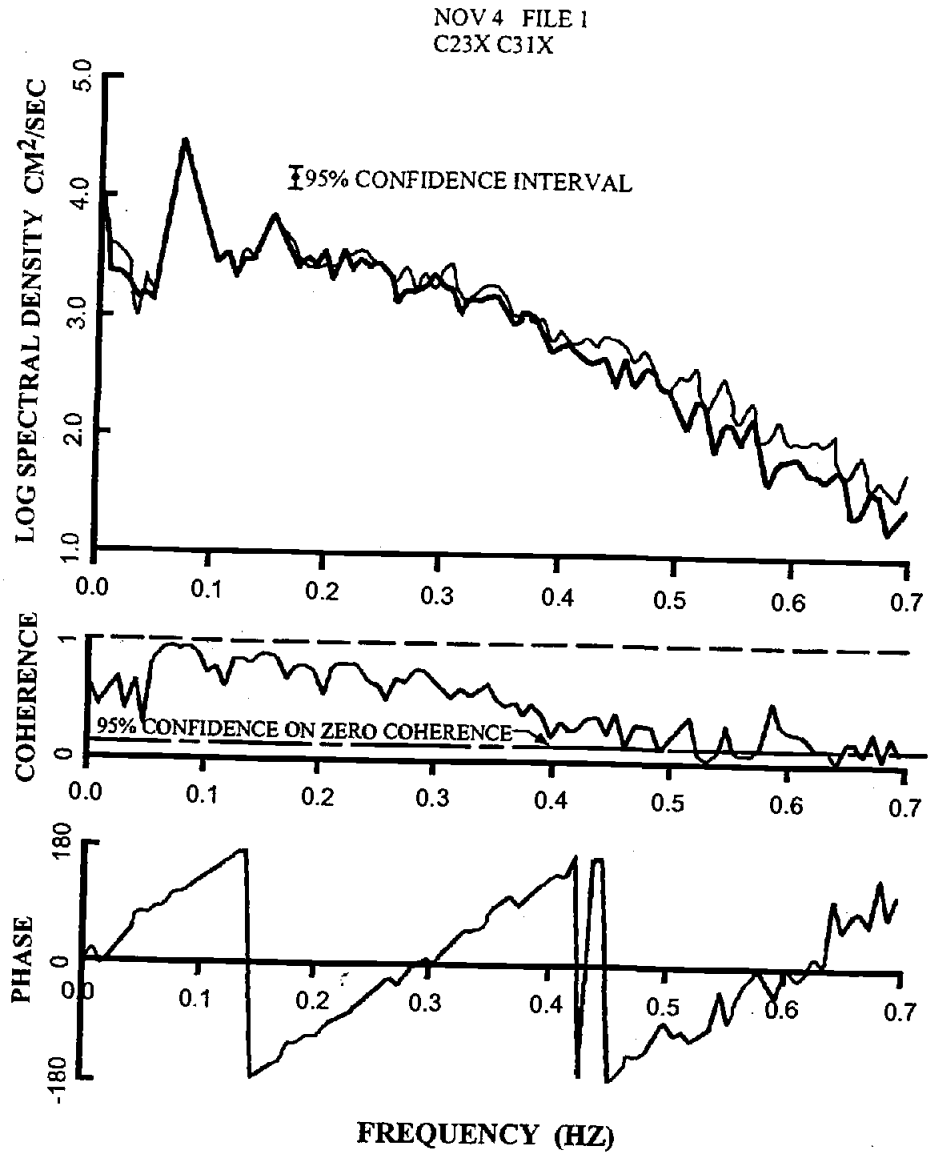

Figure 2.1 Energy density, coherence, and phase calculated from two spatially separated current meters as a part of the Nearshore Sediment Transport Study, November 4, 1978 (from Thornton and Guza, 1982).

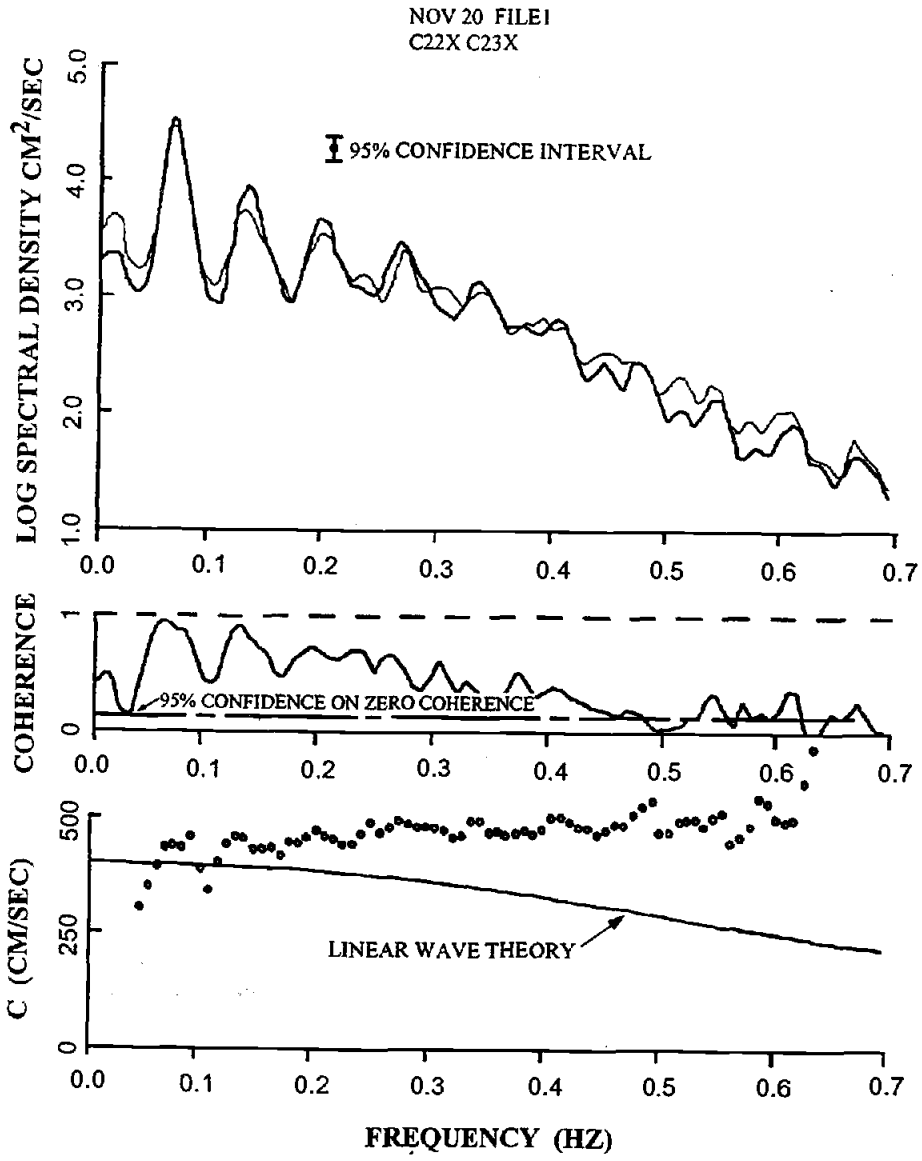

Figure 2.2 Energy density, coherence, and celerity spectra for current meters C22 (light line) and C23 (heavy line), November 20, 1978 (from Thornton and Guza, 1982).

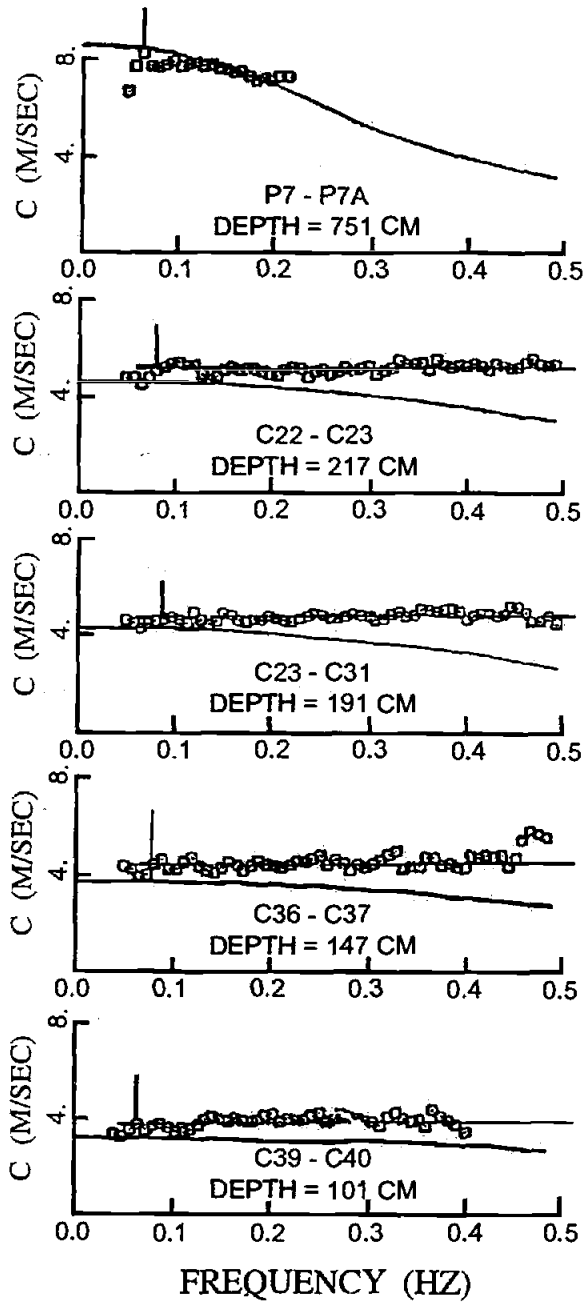

Figure 2.3 Celerity spectra at different water depths for narrow banded waves on November 20, 1978. The solid curved line corresponds to the theoretical dispersion relationship and the solid straight line represents the average celerity across the spectrum. Vertical arrows show the peak frequency of the incident waves (from Thornton and Guza, 1982).

to the true wave (known as a modulation transfer function) must be spatially constant, especially in phase since it is the phase structure that is used to measure celerity.

The observed relationship between the true wave signal and a remotely sensed video signal can be described by a modulation transfer function (MTF). A MTF is a linear spectral representation of the relative amplitudes and phases between an input signal and an output signal. The relationship between the Fourier transform of the input signal X(f) and the Fourier transform of the output signal G(f) can be expressed as

$$G(f) = M(f)X(f) \tag{2.9}$$

where the magnitude of M(f) is the modulation transfer function [*Gonzales and Woods*, 1992]. Thus, the complex gain function can be used to describe the relationship between both the phases and amplitudes of the visual signature of the waves and the true wave form. Techniques described in this paper will primarily be based on signal phases.

The brightness of the sky varies from very bright near the horizon to darker near zenith, a variation called the sky gradient [*Lynch and Livingston*, 1995]. Offshore from the breakpoint, a wave can be seen because of the specular (directional) reflection of the sky gradient on the slope of the sea surface. For example, when standing on the beach, onshore propagating waves can be identified by the dark front face of the wave (reflecting in the near zenith sky brightness) while the back face will be brighter, if not hidden from view. The angle of view of the surface then also determines how strong the visible wave signal will be. For example, if one were to look along a wave crest, there will be no sea surface slope component in the direction of view; therefore, the wave would not be as easily discernable as if the view were directly into the wave crest. In the region prior to wave breaking, the MTF is a spatially steady function with a fixed phase relationship between the visual representation of the waves and the true amplitude and phase, dependent on the angle between the camera and the wave approach.

Once waves move onshore and begin to break, individual wave crests can be recognized by diffuse (scattered) reflection from the white foam associated with the

turbulence of breaking. Since the signature of the wave is now marked by a white face rather than the darker faces observed outside of the break point, the MTF shows a different, yet still coherent, phase relationship between the remotely sensed signal and the true signal. Because the reflection is diffuse, there is no longer any dependence on viewing geometry.

Lippmann and Holman [1991] tested the relationship of remotely sensed video data to the actual wave form by comparing time series of pressure data and video pixel intensity taken at a position within the surf zone. A visual correlation between the co-located time series of video intensity and pressure in Figure 2.4 shows similar peaks marking the progression of wave crests. Cross spectra between video and pressure sensor data show a high coherence between the two in the incident frequency band (Figure 2.5) indicating that video may serve as a valid proxy for the phase progression of breaking waves [*Lippmann and Holman*, 1991].

Lippmann and Holman further tested the capability of video data analysis for estimation of phase speed and wave angle of individual breaking waves using data from the 1990 Delilah experiment in Duck, NC. Video data of the surf zone were collected from a northeast facing camera that was positioned on a tower approximately 43 meters above the beach. Using pixel intensity time series collected with a square array, 4m wide, composed of four pixel sensor locations, phase speeds and wave angles were calculated. The time lag of wave propagation past sensors that were spatially separated in the cross-shore was calculated in both the time and frequency domains. In the time domain, travel-time of the wave was calculated using a lagged cross-covariance function. In the frequency domain, cross-spectra were first computed and then time lags were derived from the linear ramp in the phase spectra (equation 2.8). The speed of the wave was then calculated as the separation distance divided by this time lag. Figure 2.6 indicates good agreement between the estimated celerity spectrum and that obtained from in-situ

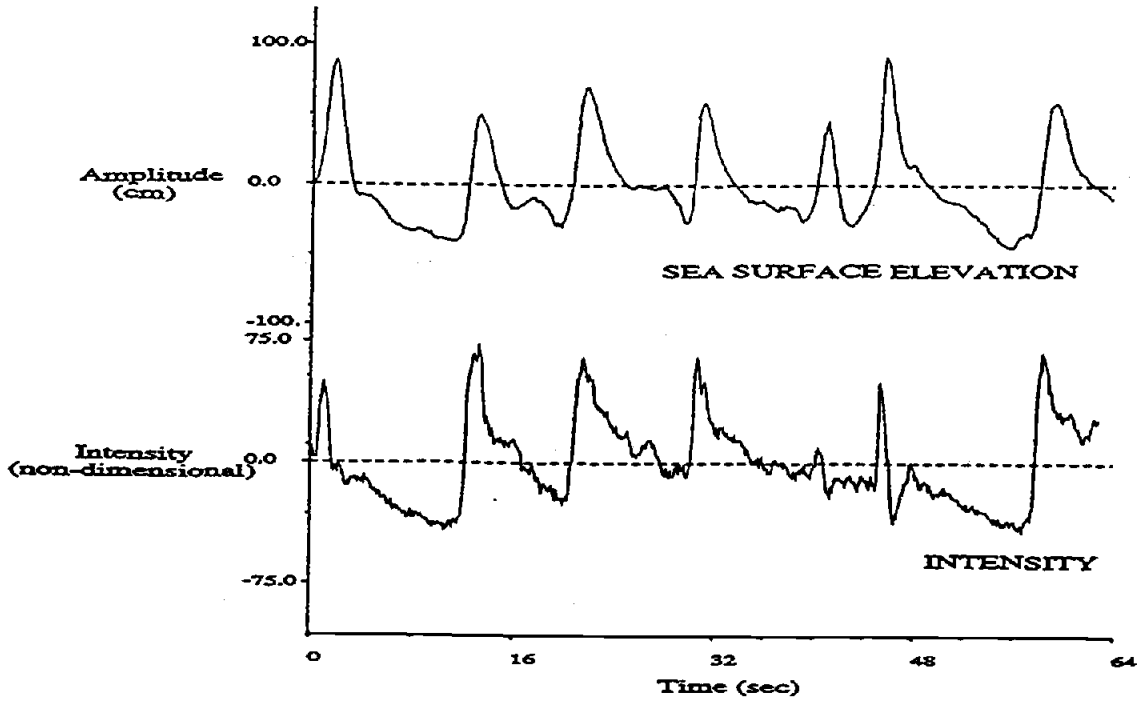

Figure 2.4 Example co-located pressure (top) and video intensity (bottom) time series from October 12, 1990 (from Lippmann and Holman, 1991).

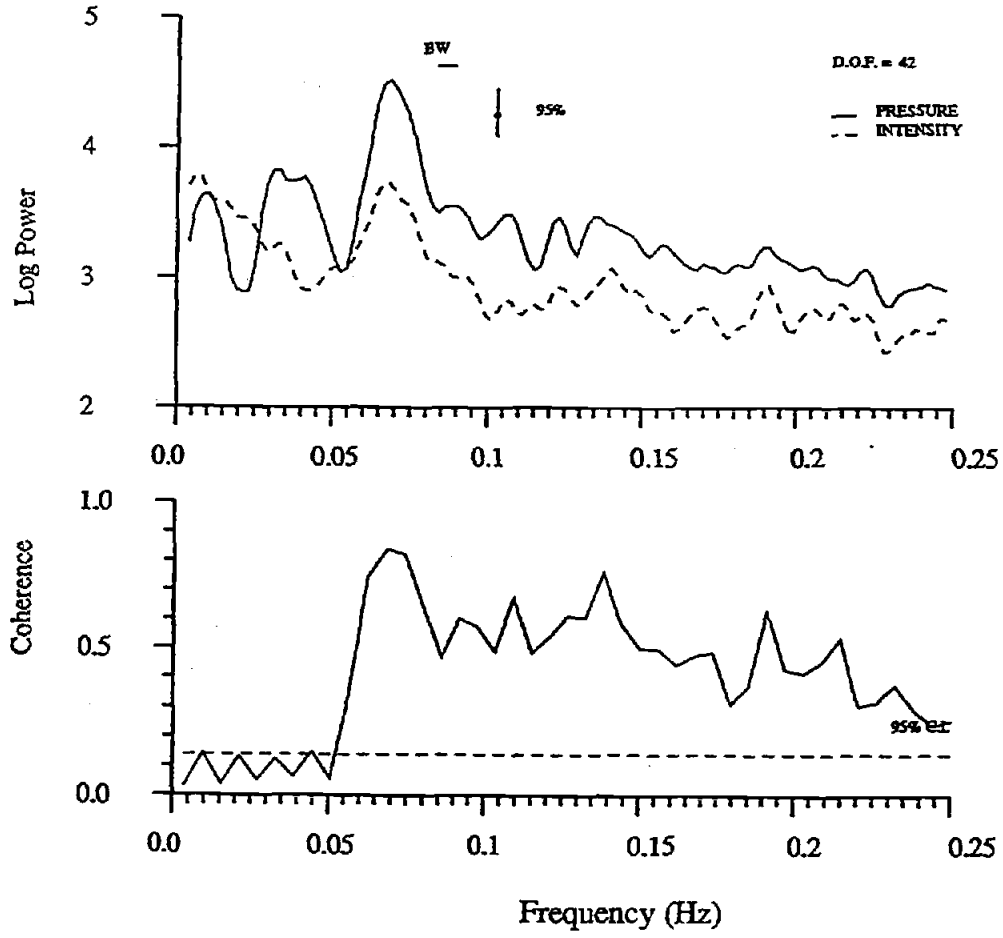

Figure 2.5 Cross-spectrum between a video intensity time series and an in-situ pressure gauge from the mid-surf zone. Power spectra are shown in the top panel and the coherence is shown in the lower panel (from Lippmann and Holman, 1991).

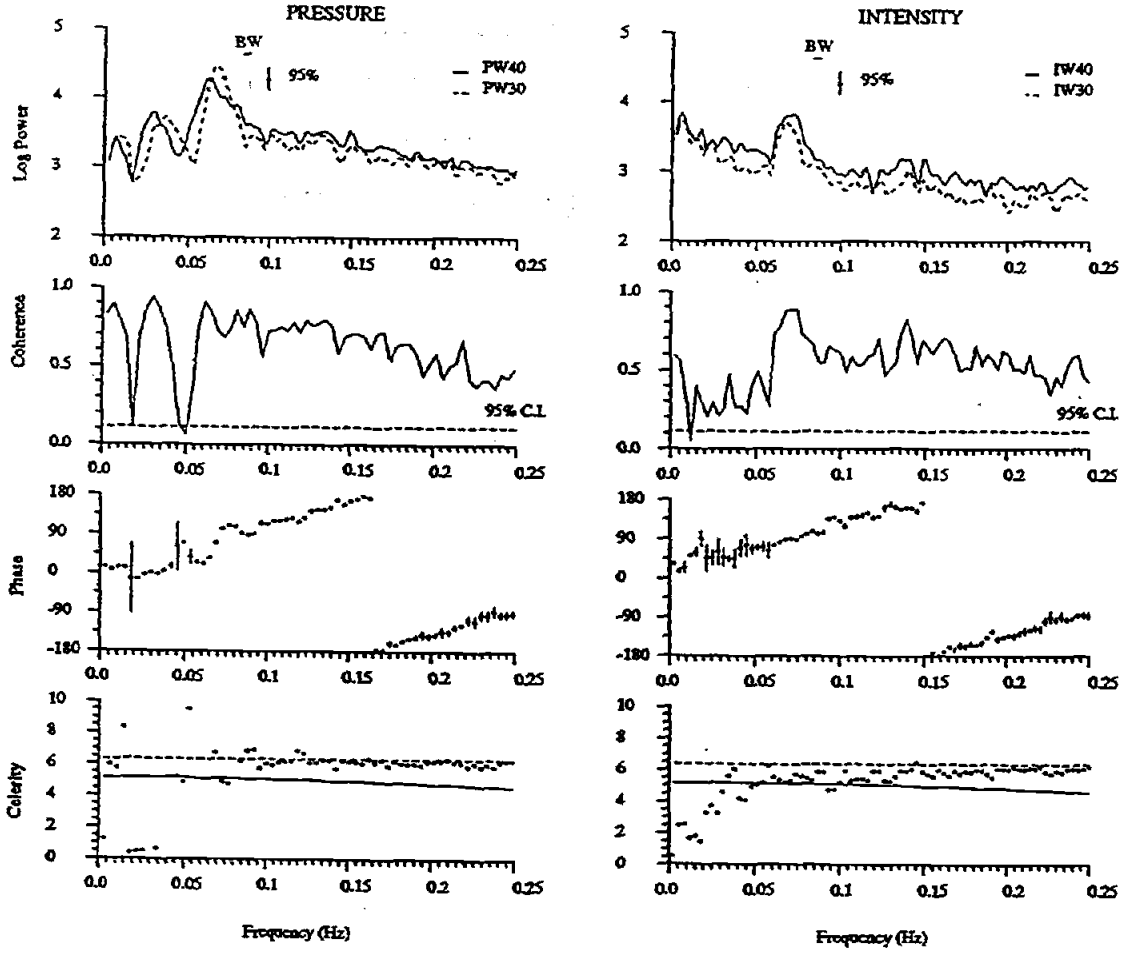

Figure 2.6 Amplitude, coherence, phase, and celerity spectra between time series collected from sensors separated 18m in the cross-shore for both pressure (left column) and intensity data (right column). All spectra were computed for 52 degrees of freedom. The linear (solid line) and solitary (dashed line) theory approximations are plotted on the celerity spectra for comparison (from Lippmann and Holman, 1991).

instrumentation. Celerities were reasonably consistent with the solitary wave theory estimate of phase speed, showing the presence of some amplitude dispersion [*Lippmann and Holman*, 1991].

It seems quite reasonable that the individual point estimates of celerity found by Lippmann and Holman could be extended to allow full cross-shore coverage. This involves the extension of the pair-wise calculation to an array of locations and then the estimation of wave phase speed along the transect. Once this measurement has been done, the automatic estimation of full transects of water depths can be calculated from phase speed based on linear theory.

3. VIDEO TECHNIQUE FOR BATHYMETRY ESTIMATION

From equation (2.3), the local water depth at cross-shore position, x, can be defined as

$$h(x) = \frac{\tanh^{-1}\left(\frac{\sigma^2}{gk(x)}\right)}{k(x)}. \tag{3.1}$$

The presence of the hyperbolic tangent in equation 3.1 makes the expression for depth complicated to work with. The shallow water expression for celerity may appear to provide an alternatively simple calculation of depth, but will yield errors that increase with depth.

Figure 3.1 presents a comparison between the full dispersion relationship and the shallow water approximation. In Figure 3.1(a), water depth normalized by the deep water wavelength is plotted versus the wavelength normalized by the deep water wavelength. The two curves begin to diverge visually at $L/L_o \sim 0.55$. This value can also be found theoretically from equation (2.2) as

$$\frac{L}{L_o} = \tanh\left(\frac{2\pi h}{L}\right) \approx 0.95\left(2\pi h \frac{h}{L_o}\frac{L_o}{L}\right) \tag{3.2a}$$

$$\left(\frac{L_o}{L}\right)^2 = 0.95\left(2\pi \frac{h}{L}\right) = (0.55)^2, \tag{3.2b}$$

making use of h/L = 1/20 and tanh(kh)~0.95(kh) as the shallow water limits. As L/L_o approaches 1, the ability to estimate water depth becomes very sensitive to errors in wavelength and the technique becomes unstable.

Figure 3.1(b) shows the relationship between the relative error in wavelength (dL/L) and the corresponding relative error in water depth (dh/h). For shallow water, errors in depth asymptotically approach a value twice the wavelength errors. For deeper water, the sensitivity to errors becomes infinite as L/L_o approaches 1. As a pragmatic decision, we choose to neglect any values for which the sensitivity exceeds 4, corresponding to

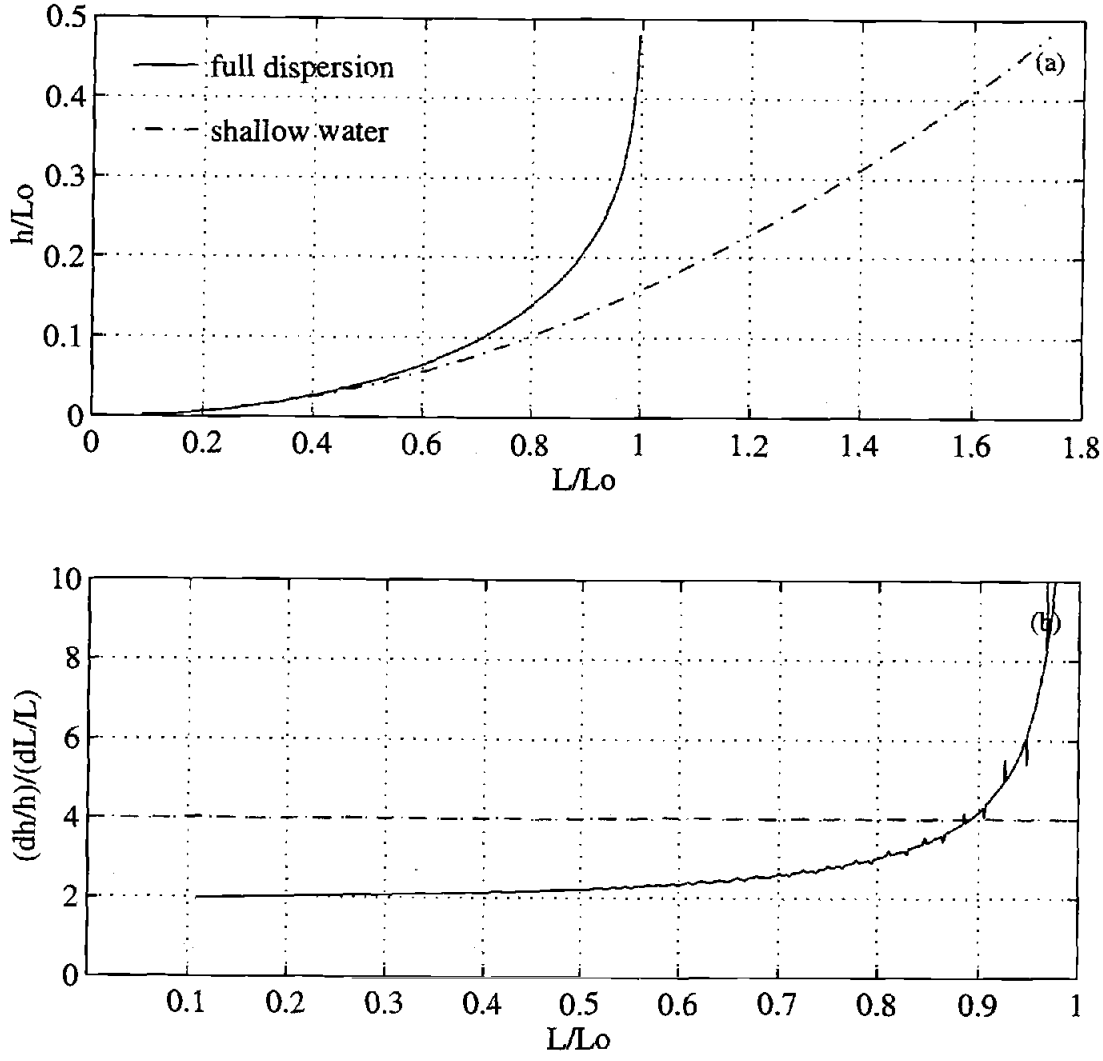

Figure 3.1 Sensitivity analysis of the dispersion relation based on deep water wavelength. Plot of the linear dispersion relation, comparing wavelength to local water depth, both normalized by the deep water wavelength (a). The solid line corresponds to the full dispersion equation, while the dashed line represents the shallow water approximation. The sensitivity of predicted depth to errors in estimated wavelength, both expressed as a percentage, versus relative wavelength (b). The dashed line at y = 4 indicates the cutoff value selected for this study.

$L/L_o > 0.9$. In order to obtain greater accuracy with the video technique, the full representation of the dispersion equation is used rather than the shallow water assumption.

Equation (3.1) can be expanded to allow for an oblique wave approach,

$$h(x) = \frac{\tanh^{-1}\left(\frac{\sigma^2}{gk(x)}\right)}{k(x)} = \frac{\tanh^{-1}\left(\frac{\sigma^2}{g\left(\sqrt{k_x(x)^2 + k_y(x)^2}\right)}\right)}{\sqrt{k_x(x)^2 + k_y(x)^2}}, \tag{3.3}$$

where $k_x(x)$ and $k_y(x)$ are the cross-shore and longshore components of wavenumber. The estimation of water depth is now reduced to measuring both wavenumber components and the incident frequency from pixel intensity data.

3.1 Estimation of Frequency

The methodology for the video technique first involves the collection of pixel intensity time series along a single cross-shore and multiple longshore arrays of pixel locations. Figure 3.2 presents a synthetic timestack for a shoreward progressive wave. The timestack illustrates the variations in wave amplitude (or for the video technique, pixel intensity) at each cross-shore location through time. The traces of wave crests can be used to estimate the speed of the waves.

The data are first smoothed with a high-pass filter to remove low frequency trends ($f<0.05\ s^{-1}$) and then again with a low pass filter to remove noise ($f>0.5s^{-1}$). Spectra are calculated at each cross-shore sensor location using a bandwidth of $0.0103s^{-1}$ and 42 degrees of freedom. An average spectrum is then calculated over all cross-shore locations. The spectral peak was selected as the frequency corresponding to the center of

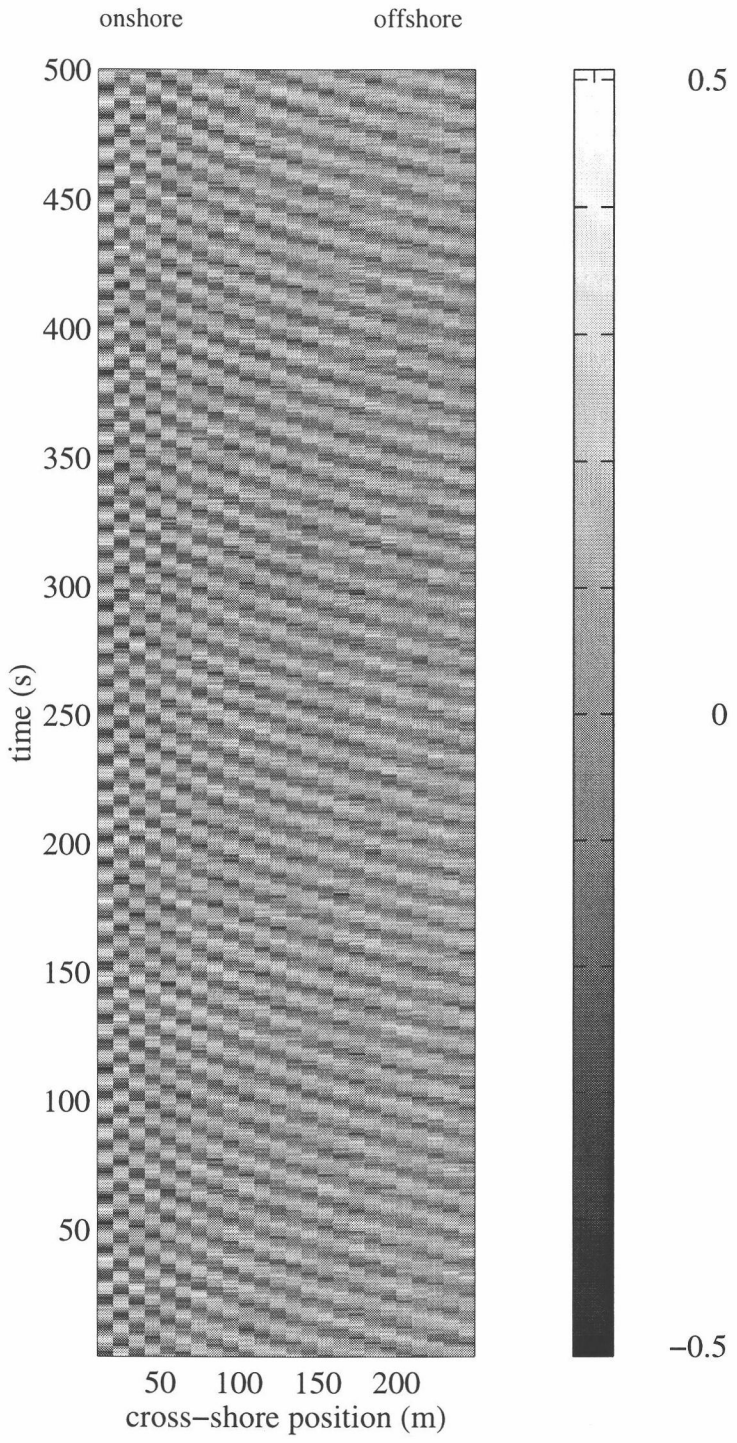

Figure 3.2 Timestack of a synthetic time series for a shoaling 10 second wave. The stack illustrates variations in wave amplitude (or intensity) at each cross-shore position (horizontal axis) through time (vertical axis). The slope of the wave crest traces represents the approximate speed of shoaling waves.

mass within a predefined incident frequency range of 0.05 - 0.20s^{-1}. The frequency of center of mass for the spectra is calculated as

$$f_{cm} = \frac{\sum_{i=1}^{N} S_i f_i}{\sum_{i=1}^{N} f_i}. \tag{3.4}$$

The incident peak is the only frequency considered in the calculation of phase speed because video is best capable of 'seeing' this one fundamental frequency. Additionally, in the nearshore region, the harmonics of the fundamental are locked to the peak frequency suggesting that the most accurate representation of the phase speed will be at the incident peak.

3.2 Estimation of Cross-shore Wavenumber

Once the peak frequency is selected, the remainder of the analysis is then limited to data within a frequency band centered around the incident peak. The cross-shore wavenumber is determined from analysis of wave phase structure using a frequency domain empirical orthogonal function (CEOF) of the data collected from the cross-shore array. The CEOF analysis is a method for detecting propagating signals from data collected over spatially separated sensors. The technique involves eigenvector analysis of the cross-spectral matrix within a frequency band of interest. This type of analysis allows waves of different frequencies to be resolved and then defines their amplitudes and phases through the first mode of the eigenvectors [*Wallace and Dickinson*, 1972].

For the video technique, the input signal is that of pixel intensity, I(x,t). The Fourier transform of the data is represented as

$$\mathrm{Y}(x,f) = FT(I(x,t)). \tag{3.5}$$

The cross-spectral matrix is then calculated as

$$Q_{ij}(f) = \left\langle \mathrm{Y}_i^* \mathrm{Y}_j \right\rangle, \tag{3.6}$$

where Y_i^* is the complex conjugate of the Fourier transform and < > represents an ensemble averaging, here approximated by averaging over the frequencies within the band of interest. The cross-spectrum is then normalized

$$Q' = \Omega^{1/2} Q \Omega^{1/2'} \tag{3.7}$$

by the diagonal matrix, Ω, which contains the variance $\sigma^2(x_i)$ at each position. Eigenvector analysis of the normalized cross-spectral matrix yields a normalized eigenvector,

$$\Lambda(f) = EOF(Q(f)'). \tag{3.8}$$

The percent variance explained by the first mode of Λ can be expressed as

$$V_1 = \frac{\lambda_1}{\sum_{i=1}^{N} \lambda_i} \tag{3.9}$$

where λ_i are the eigenvalues. The first mode generally contains the majority of the variability within the data set [*Merrifield and Guza*, 1990]. Therefore, we select the first mode, complex eigenvector

$$\Lambda_1 = a(x) + ib(x), \tag{3.10}$$

as the single mode to represent the cross-shore structure. The phase, ϕ, and amplitude, A, at each cross-shore position can be calculated as

$$A(x) = \sqrt{(a^2(x) + b^2(x))}, \text{ and} \tag{3.11}$$

$$\phi(x) = \tan^{-1}\left(\frac{b(x)}{a(x)}\right). \tag{3.12}$$

Finally wavenumber is calculated as the cross-shore gradient in phase

$$k_x(x) = \frac{d\phi}{dx} \tag{3.13}$$

[*Merrifield and Guza*, 1990].

For regions for which A(x) is large, the cross-shore phase structure of the mode is likely to be significant. Low amplitudes at the ends of the array and erratic fluctuations of amplitudes within the array are indications of a noisy signal and low coherence across the

array [*Merrifield and Guza*, 1990]. To avoid spurious results, a threshold amplitude was arbitrarily chosen as 0.70, below which the EOF structure was considered to be unreliable.

The proposed technique for estimating cross-shore wavenumber was tested using a synthetic time series based on a shore-normal ten second wave shoaling on a beach with a slope of 0.02. The amplitude structure (Figure 3.3a) shows that the first EOF explains approximately 100% of the variance uniformly across the beach. A phase ramp, shown to steepen onshore (Figure 3.3b), indicates a shoreward progressive wave whose phase speed decreases as it shoals. From the slope of this phase ramp, the cross-shore wavenumber (Figure 3.3c) is calculated. Knowing the wave period of this test a priori (or in the case on a natural beach, from the frequency selection described in section 3.1), the depth can then be estimated using equation (3.3) and compared to the input depth profile (Figure 3.3d). The close comparison between the two confirms the merit of the analysis approach.

3.3 Estimation of Longshore Wavenumber

On natural beaches, waves rarely approach from directly offshore. Therefore, the longshore component of wavenumber, k_y, must be estimated. The longshore wavenumber is determined by performing a similar CEOF analysis at each longshore array. The longshore wavenumber is calculated at the midpoint of each longshore array as the longshore gradient in phase, ϕ, associated with the first mode of the EOF

$$k_y(x) = \frac{d\phi}{dy}. \tag{3.14}$$

Knowledge of both the cross-shore and longshore components of wavenumber allows for the calculation of wave angle, α, at each point in the cross-shore array as

$$\alpha(x) = \tan^{-1}\left(\frac{k_y(x)}{k_x(x)}\right). \tag{3.15}$$

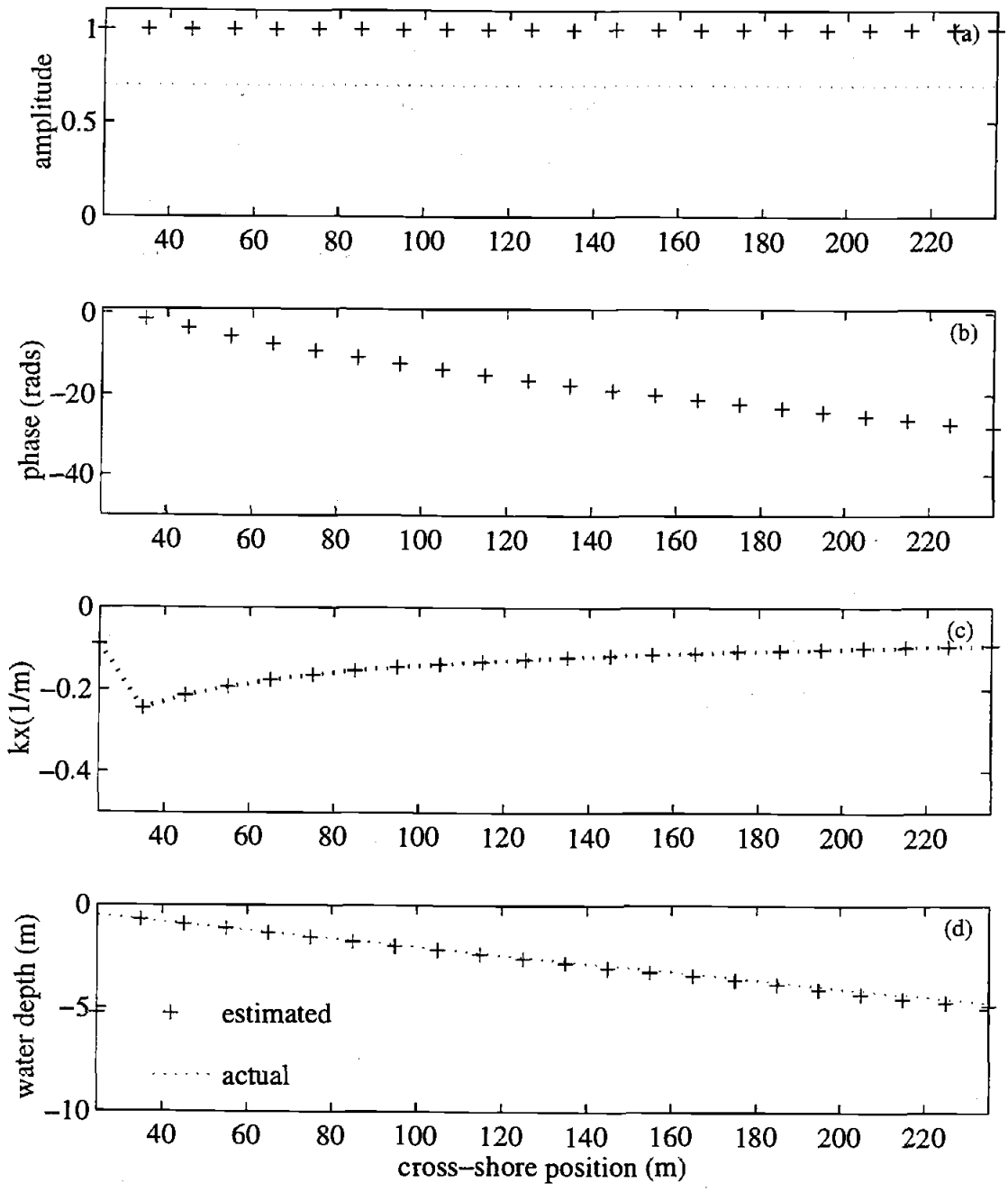

Figure 3.3 Synthetic series test for the extraction of cross-shore wavenumber. Amplitude (a), phase (b), cross-shore wavenumber (c), and estimated water depth (d) are presented as a function of the cross-shore position. The amplitude structure shows that the first EOF explains approximately 100% of the variance uniformly across the profile. From the slope of the phase ramp, the cross-shore wavenumber is calculated. Estimated depths are compared to the input depth profile.

4. FIELD TESTS

The development and initial tests of the video technique were performed with data from the Delilah experiment conducted during October 1990 at the U.S. Army Corps of Engineers Field Research Facility (FRF) located in Duck, North Carolina. One data run from Delilah will be used to first illustrate the technique and explain initial results. The technique was then further tested using data routinely collected from the remotely-operated video cameras deployed at the Argus Stations located in Duck, North Carolina and Agate Beach, Oregon.

4.1 The Delilah Experiment - Duck, North Carolina

The FRF site in Duck, North Carolina is an intermediate sloping beach dominated by incident wave energy. The offshore bathymetry is generally dominated by one or two offshore sand bars. Beach slopes typically range from 0.04 on the foreshore to approximately 0.02 offshore of the sand bar (Figure 4.1).

During the Delilah experiment, a video camera positioned on a tower 43 m above sea level was pointed in a northeast direction toward the surf zone to record the shoreward progression of waves (Figure 4.2). Video data were collected on tapes for a total of 16 days over a wide variety of wave conditions. The video tapes allowed for post-processing array design and data collection after the experiment had been completed. Video data collection and processing procedures are detailed in Lippmann and Holman [1989] and Lippmann and Holman [1991].

To illustrate the details of the technique, we will be using results from data collected on October 8, 1990 at 1612 EST. On this day, the significant wave height measured in 8 m water depth was 0.7 m, the peak wave period was 10.7 s and the wave approach was from the northeast. Time exposure images showed mild wave breaking over a sand bar

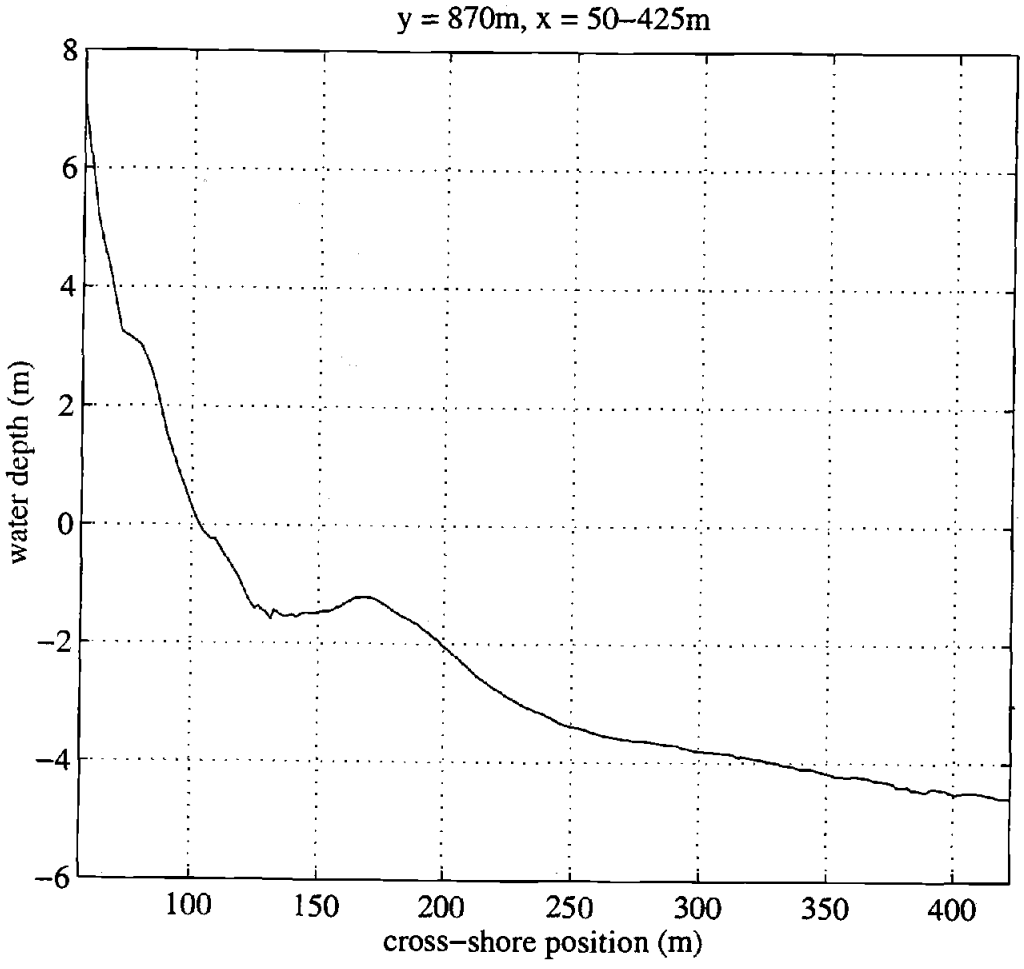

Figure 4.1 Offshore profile surveyed at Duck, North Carolina on October 8, 1990. Data shown were collected by the CRAB along y = 870 m in the FRF coordinate system and extend approximately 325 m offshore. In the coordinate system defined for this site, the shoreline is located at approximately x = 100 m.

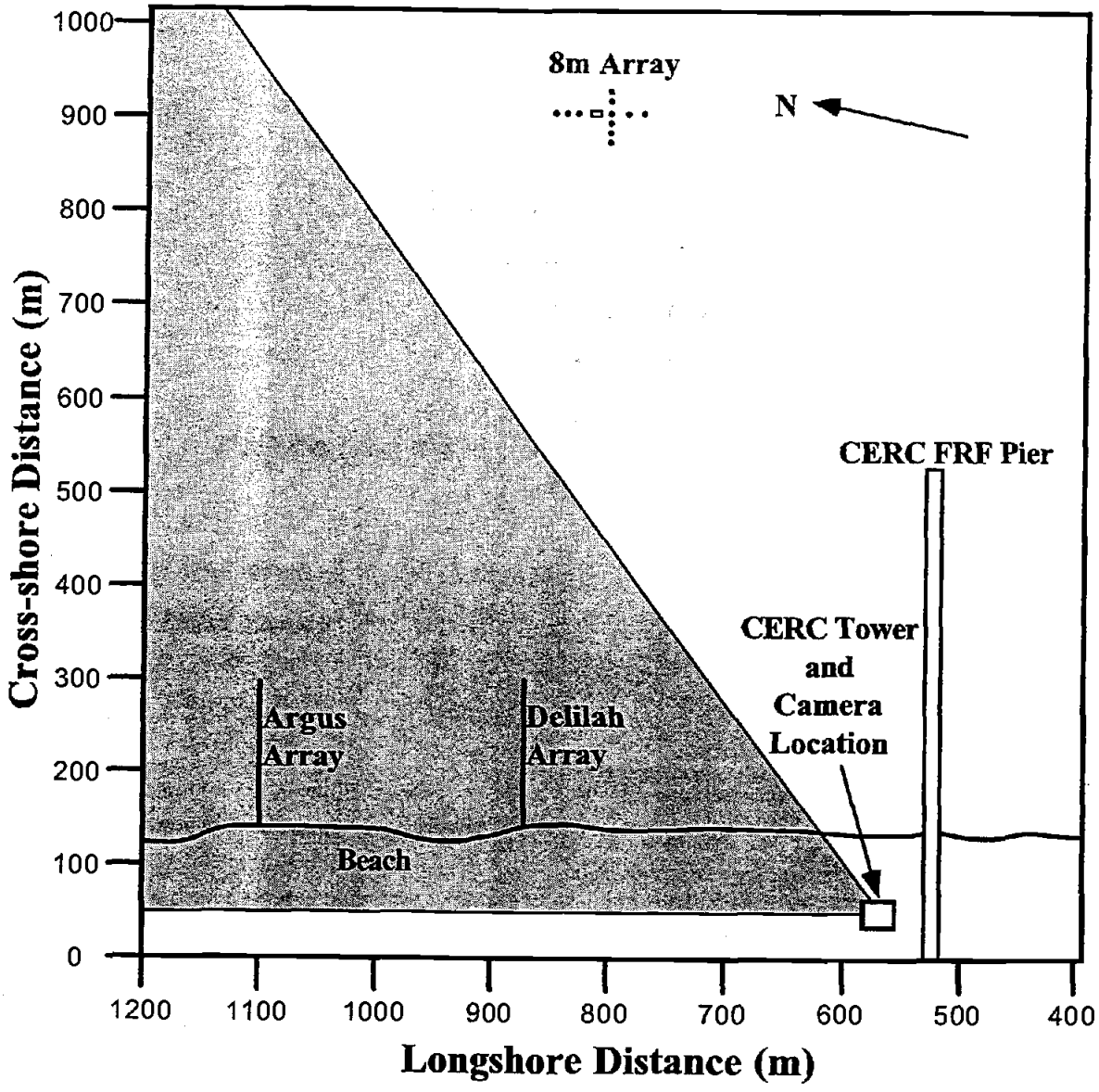

Figure 4.2 Map of the field site in Duck, North Carolina. Location of the Coastal Engineering Research Center (CERC) video tower, the FRF pier and the 8 m array are indicated. The locations of the cross-shore arrays for depth estimation for the Delilah experiment and for the Duck Argus are shown. The stippled area indicates the field of view of the camera.

located approximately 75 m offshore. The slope of the beach was approximately .08 in the inner surf zone and .02 offshore. The tidal range was of the order of 1 m.

4.1.1 Sampling Design

The pixel sensor spacing of the sampling array was selected to maximize the coherence between adjacent sensor locations, but also to allow enough distance between the sensors for the identification of a statistically significant phase lag. Because of wave refraction, wave-wave interaction, and wave breaking, coherence between sensors is not expected over very large spatial scales [*Lippmann and Holman*, 1991]. Therefore, a cross-shore sensor spacing of 5 m was used in the array design

The cross-shore pixel array shown in Figure 4.3 consists of 25 locations extending from 100 to 225 m in the cross-shore and is located at FRF longshore coordinate 870 m. Four longshore arrays, spaced 25 m in the cross-shore, contain six pixel sensor locations each and are centered about the cross-shore array. Vertical locations of the pixels were chosen at mean sea level.

Using the known geometry of the image, the list of sampling locations (x_i, y_i, z_i) was converted to a corresponding list of pixel coordinates (u_i, v_i) [*Holland, et al.*, 1997]. Timestacks of pixel intensity were then collected at each point in the array at a rate of 1 Hz for 34 minutes.

Figure 4.4 shows an example intensity timestack from October 8, 1990 at 1612 EST. Bright regions (high pixel intensity values) are generally associated with white foam that results as waves break over an underlying topographic high [*Lippmann and Holman*, 1989]. In this example, areas of increased intensity present at x = 110 m correspond to wave breaking on the shoreline. The timestack also gives clear evidence of a shallow feature located approximately at x = 170 m as breaking occurs over a sandbar located in this region. The

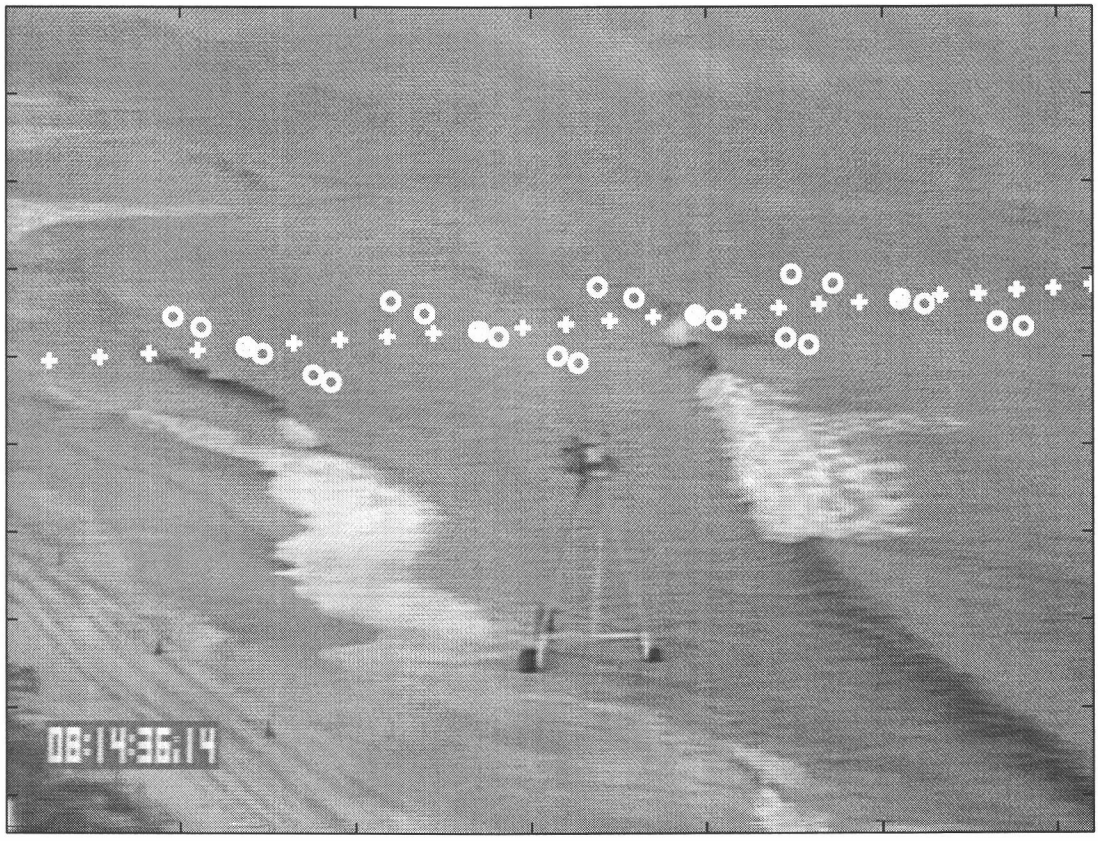

Figure 4.3 Pixel array for the Delilah experiment, Duck, North Carolina. The cross-shore array (+), located at FRF coordinate y = 870 m, consists of 25 pixel sensors spaced 5 m apart, extending approximately 125 m offshore. Four longshore arrays (O) are spaced 25 m in the cross-shore and contain six pixel locations each. The vehicle in the foreground is the FRF CRAB with a height of approximately 10 m.

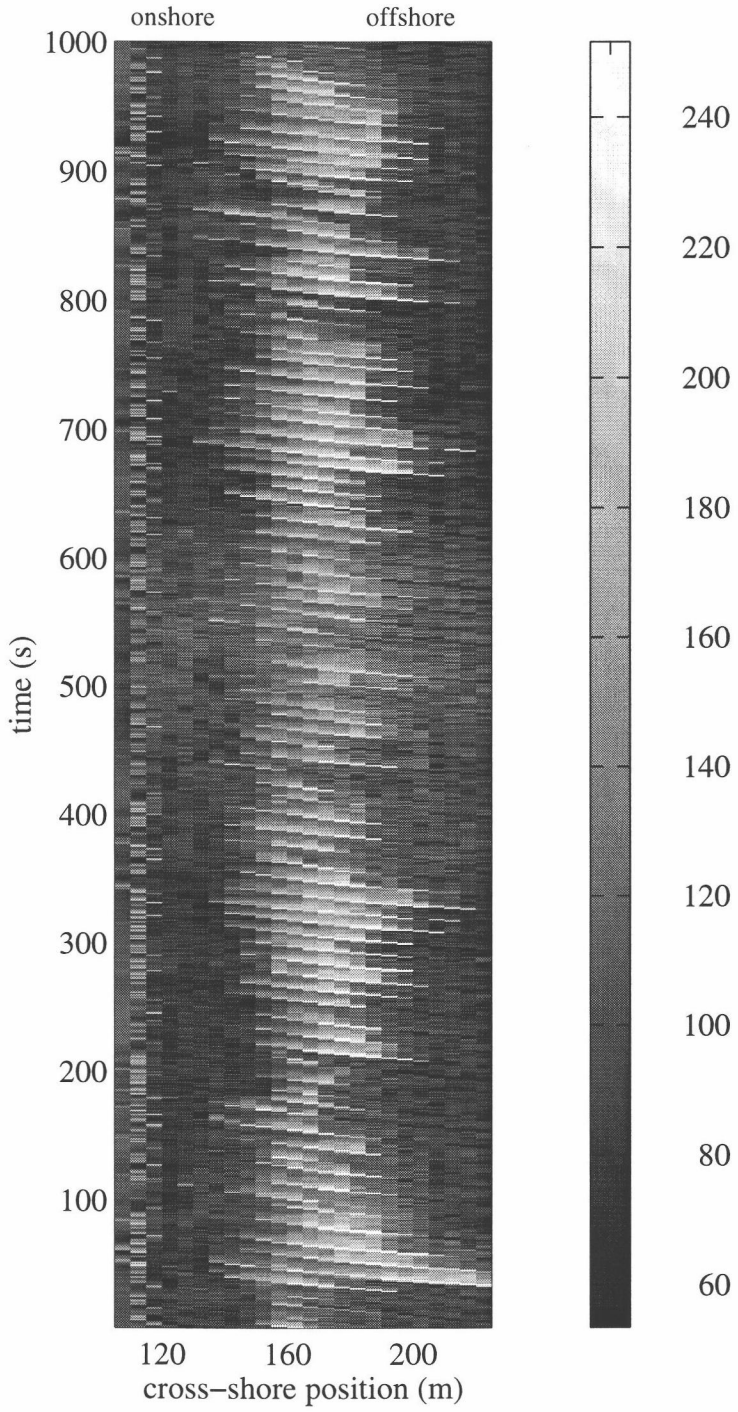

Figure 4.4 Intensity timestack from Duck, North Carolina, October 8, 1990 at 1612 GMT. Bright regions generally indicate wave breaking over an offshore sand bar. The slope of the wave traces can be used to compute the approximate speed of the shoreward progression of waves.

diagonal traces of the wave crests define the shoreward progression of the waves. The CEOF analysis is used to extract phase speed, and ultimately water depth, from these intensity data.

4.1.2 Results of Video Technique

Spectra were calculated using 42 degrees of freedom and a bandwidth of 0.0103 s^{-1} at each cross-shore position to identify the incident wave frequency. An average spectrum was calculated from the intensity spectra at all 25 cross-shore sensor locations and the peak frequency was calculated using equation (3.4).

A frequency-space plot showing the variability of the wave spectra at each cross-shore location (Figure 4.5) can be used to identify areas where the wave signal is best observed in the video data. The spectral peak is clearly defined between x = 140 m and x = 190 m due to a highly visible wave signal resulting from wave breaking over the bar. The absence of a spectral peak at some locations offshore of the breakpoint indicate that the wave signal is not as strong in this region.

Cross-spectra were computed between each pair of adjacent sensors. The coherence between each pair was used to test if the signal of the wave was being sensed at the incident frequency by each pixel in the array. A plot of the coherence between each pair of adjacent sensors at each frequency (Figure 4.6) reveals the areas where the incident waves are best detected by the pixel sensors . High coherence is found in the area associated with wave breaking over the sandbar, as the visible signature of the waves is strong in this region. Areas of low coherence will likely correspond to regions of poor performance of the video-based technique. High coherence throughout the incident band is generally required for an accurate estimation of water depth.

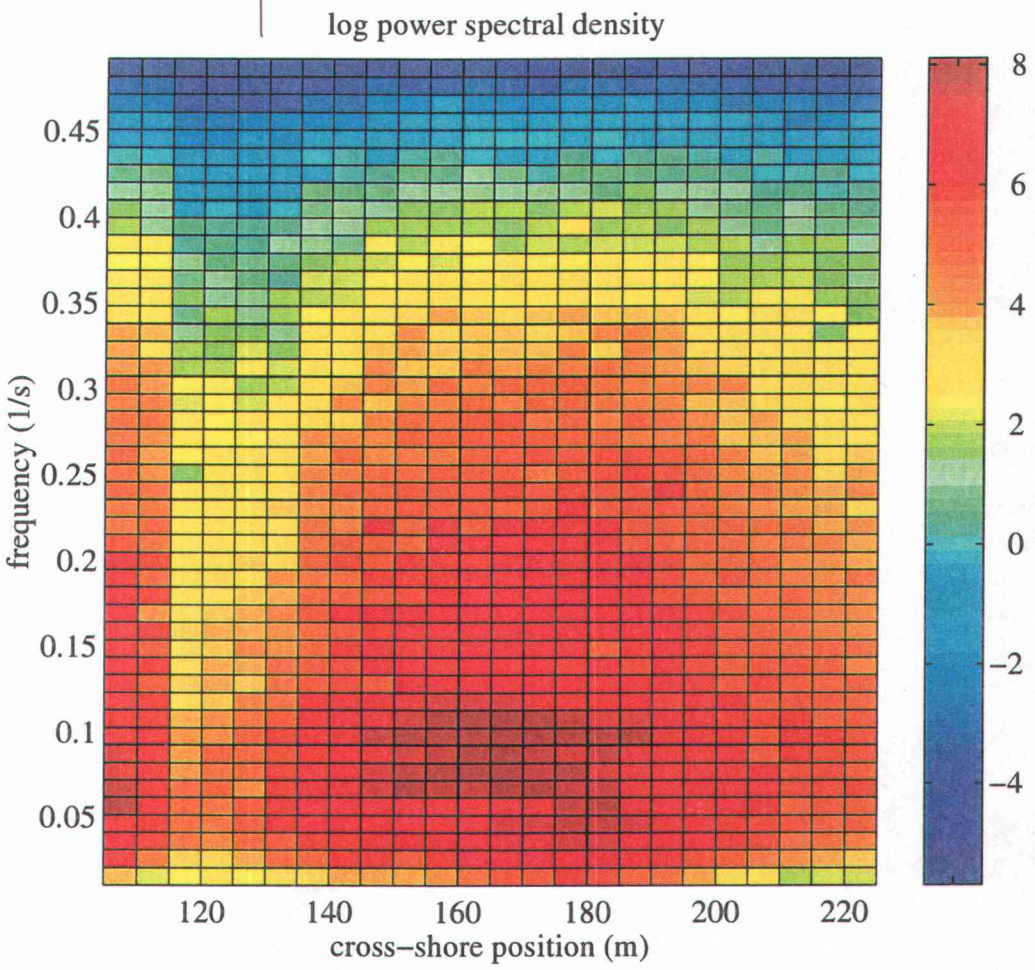

Figure 4.5 Frequency-space spectra of intensity data from October 8, 1990 at 1612 GMT. Spectra are calculated with 42 degrees of freedom and a bandwidth of 0.0103 s^{-1} at each cross-shore position. The peak in the spectra is located at 0.0918 s^{-1}. The offshore wave frequency as measured by the 8 m array at the FRF pier is 0.93 s^{-1}.

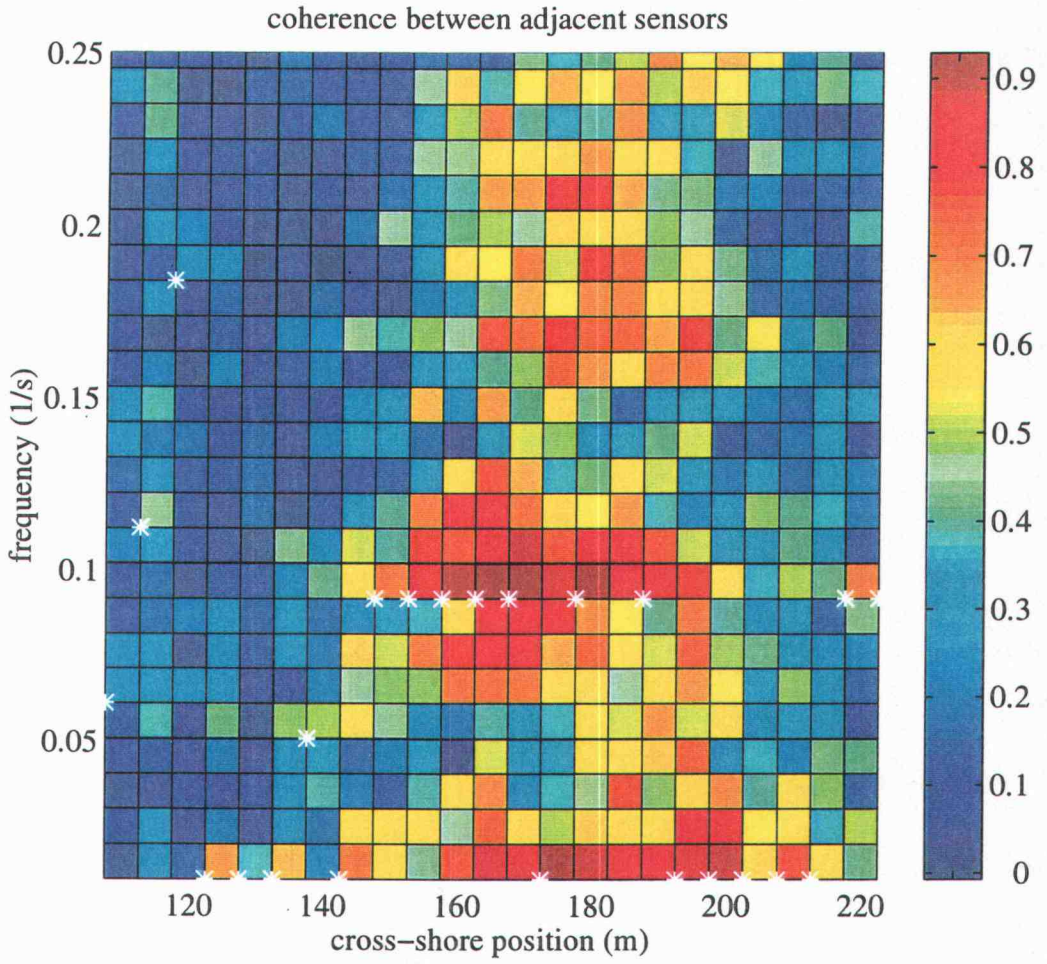

Figure 4.6 Frequency-space coherence between adjacent pixel sensors from October 8, 1997 at 1612 GMT. Cross-spectra were calculated between adjacent sensors to determine if the signal of the wave can be seen passing each consecutive pixel location. The coherence between each sensor pair is plotted for every frequency. White stars indicate the frequency of maximum coherence. The 95% confidence interval is 0.14.

The phase and celerity spectra were also examined for each pair of adjacent sensors. In order to obtain stable depth estimates, a clearly defined phase ramp should be present within the incident band. Similarly, the celerity spectra within the incident frequency band should be relatively constant over frequency at each sensor in the array since shallow water celerities are frequency non-dispersive and are solely a function of water depth. If this condition does not hold true, an accurate estimate of water depth would be sensitive to the choice of peak incident frequency.

Figure 4.7 shows the celerity spectra at each position in the cross-shore array. A general slowing of the wave is seen as it moves onshore past each sensor in the array. The celerity estimates within the incident frequency band (indicated by the two white horizontal lines) are relatively stable in the region of the profile where the coherence is high (x = 150-190 m). However in some regions offshore of the breakpoint, more variability is observed in the celerity profile making estimates of water depth in this region very sensitive to frequency selection.

In order to more closely examine specific areas along the profile, we have focused on the spectra, coherence, phase and celerity spectra calculated between two specific sensor pairs. Figure 4.8 presents the cross-spectra between sensor pairs located in the trough (x = 137.5 m) which is representative of an area of wave reformation. An incident peak can be identified within the incident frequency band (0.08 - 0.10 s^{-1}); however, the coherence (b) is low across all frequencies. Phases (c), plotted only for frequencies for which the coherence is significant, are erratic and do not indicate the presence of a progressive wave, while the celerity spectra (d) is very unstable across all frequencies. A reasonable estimate of water depth cannot be expected in this region where the coherence between adjacent sensors is not significant, as the calculation of an accurate phase speed is sensitive to the selection of one 'correct' frequency.

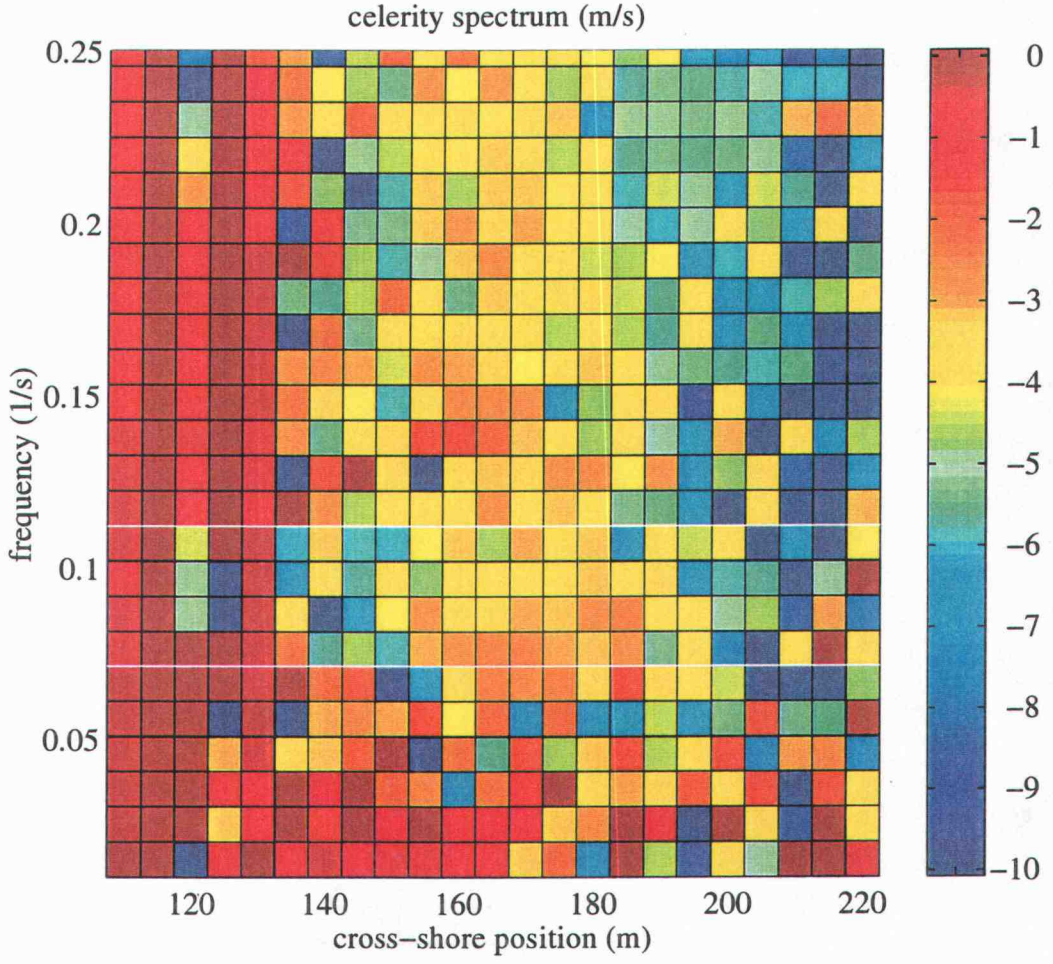

Figure 4.7 Frequency-space celerity spectra between adjacent pixel sensors from October 8, 1997 at 1612 GMT. In shallow water, celerity should be frequency non-dispersive and vary only as a function of water depth. While a relatively smooth structure is apparent, the celerity spectra measured from the intensity data does not show the same stability observed in observations from in-situ wave gauges. The incident frequency band lies between the two horizontal white lines.

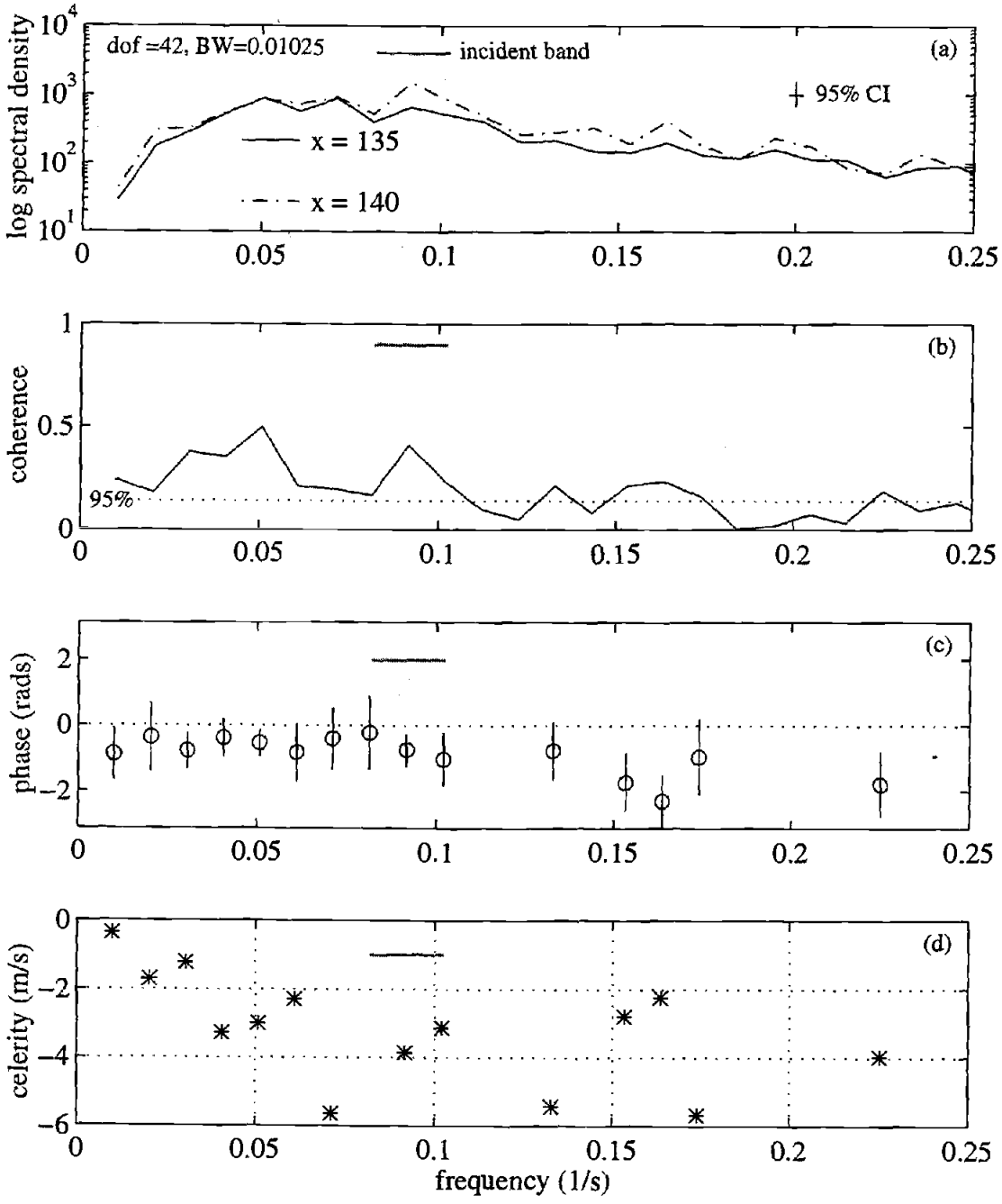

Figure 4.8 Cross-spectra between two pixels located over the trough, October 8, 1990 at 1612 GMT: log spectral density (a), coherence (b), phase (c), and celerity spectrum (d). Coherence is low within the incident frequency band (0.89 s^{-1} – 0.93 s^{-1}, indicated by the horizontal line in each plot). Phases are plotted only for those frequencies where the coherence was 95% significant. The resulting celerity spectrum is unstable across all frequencies.

Figure 4.9 presents the results of the cross-spectra between sensors located over the sand bar (x = 157.5 m) spaced 5 m apart. In this area, the video signal of the waves is strong due to prominent intensity patterns created by wave breaking. While the spectra (a) do not visually reveal a well-defined spectral peak, coherence (b) is very high throughout the incident frequency band. A well defined phase ramp (c) and stable celerity spectra (d) within the incident band are very likely to produce accurate estimates of water depth at this location.

The results of the CEOF analysis and the estimated profile for October 8, 1990 at 1612 EST are presented in Figure 4.10. The amplitude plot (a) shows that the first EOF explains approximately 90% of the variance over the bar and trough where wave breaking occurs. In other regions of low amplitude, reliable depth estimates are not expected. In areas where the amplitude is high, a clear phase ramp (b) is present indicating the shoreward progression of waves. From the slope of the phase ramp, the cross-shore wave number (b) is calculated using equation (3.13).

Wave angle is estimated from the longshore and cross-shore components of wavenumber based on equation (3.15). The sign and the magnitude of the estimated wave angle presented in Figure 4.11(a) are fairly consistent with that estimated in 8 m water depth (α~38). In Figure 4.11(b), estimated water depths calculated using equation (3.3) are compared to CRAB survey profiles that were collected daily during the Delilah experiment. The RMS difference error between the estimated and surveyed depths is 0.614 m over locations where the CEOF amplitudes are greater than 0.70.

Errors located in the region between x = 200 m and x = 190 m may be associated with either of two mechanisms associated with the onset of breaking: nonlinear evolution of the wave field and/or the existence of strong spatial gradients in the MTF. Both mechanisms are explained below.

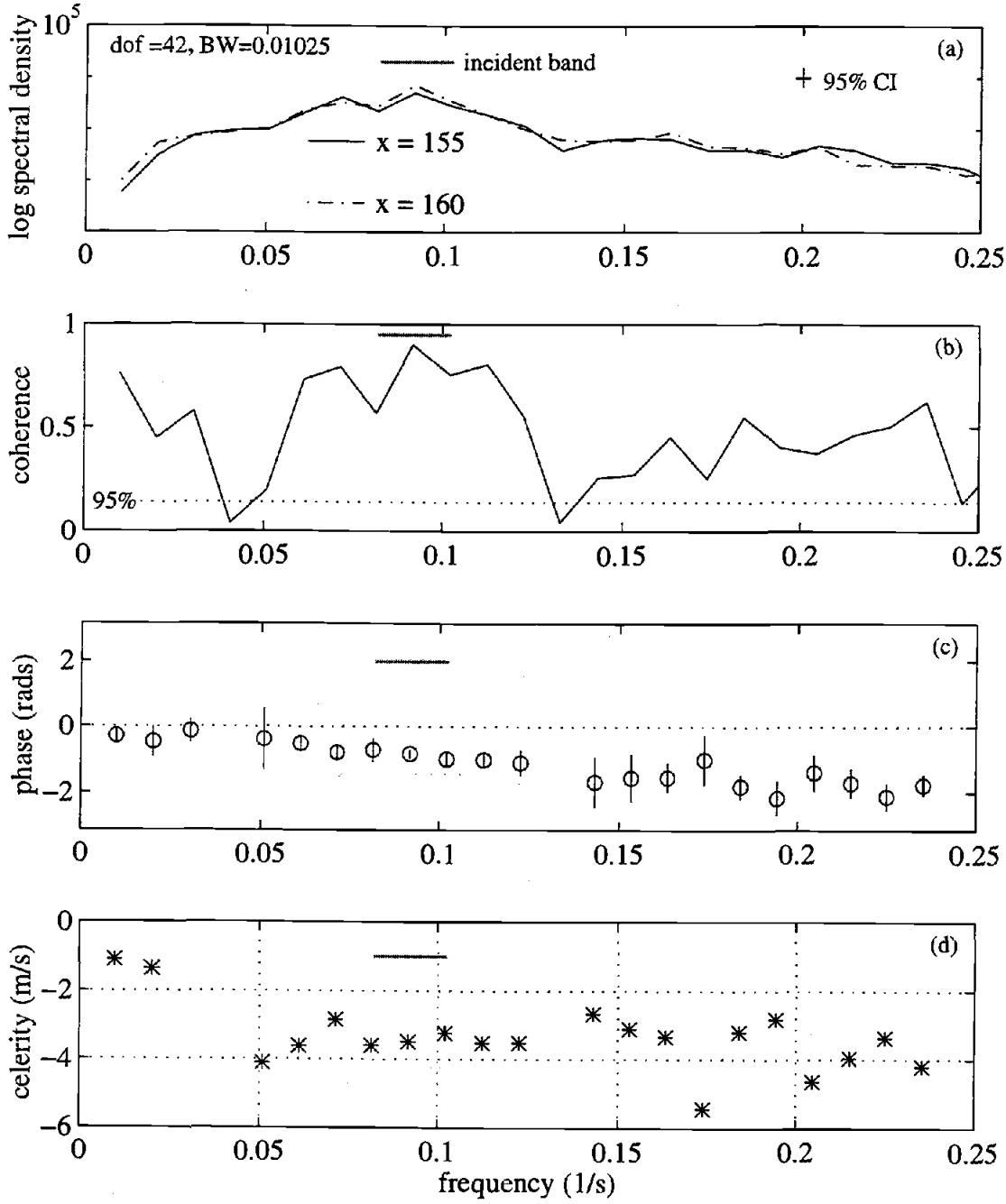

Figure 4.9 Cross-spectra between two pixels located over the sand bar, October 8, 1990 at 1612 GMT: log spectral density (a), coherence (b), phase (c), and celerity spectra (d). Coherence is high within the incident frequency band and the corresponding phase ramp is well defined. The celerity spectrum is stable across all frequencies greater than 0.05 s^{-1}.

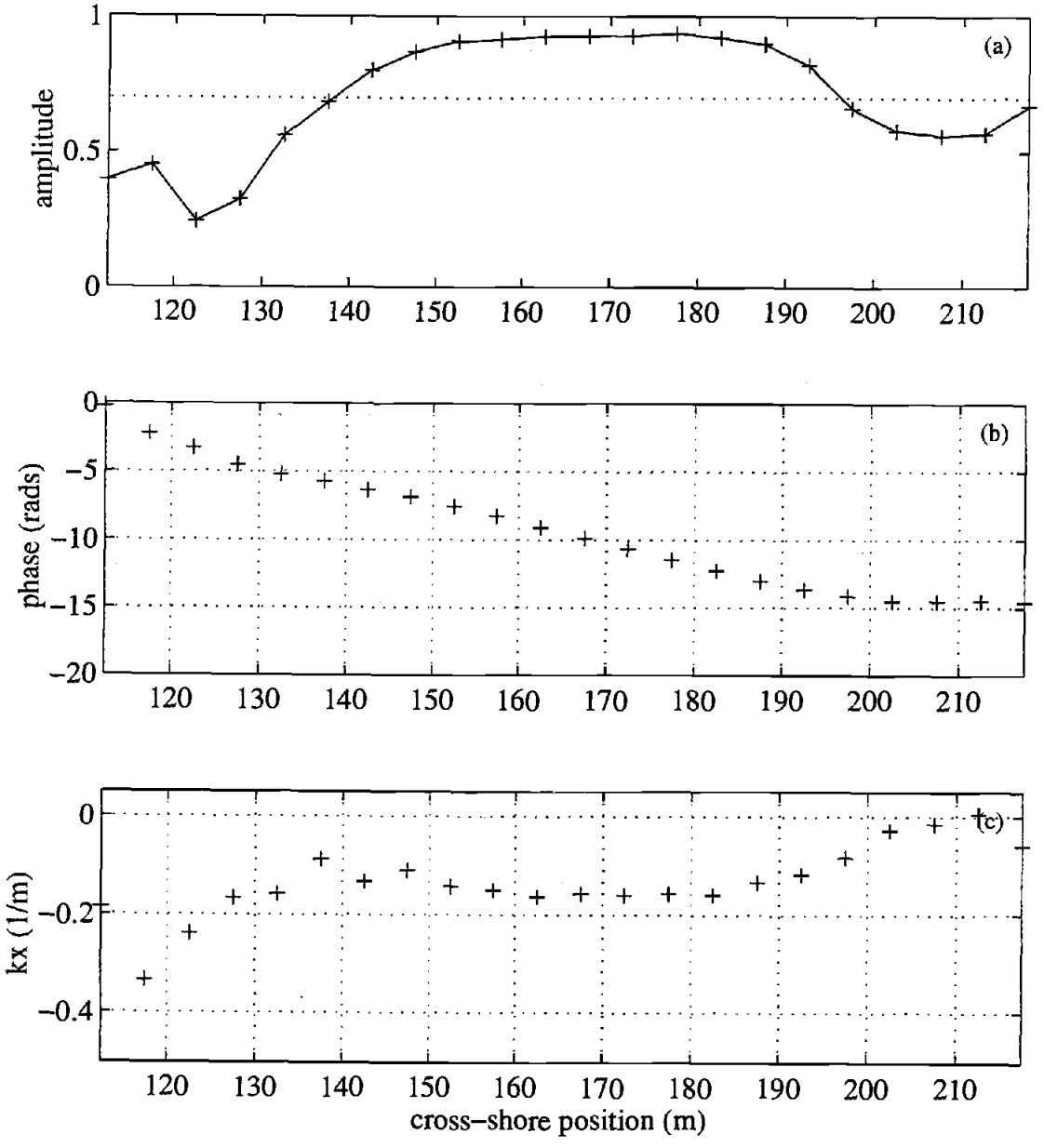

Figure 4.10 CEOF results for October 8, 1997 at 1612 GMT. Amplitude (a), phase (b), and cross-shore wavenumber (c) are shown as a function of cross-shore position. High amplitudes across the mid-surf zone indicate that the first EOF explains a significant amount of the variance in this region. Cross-shore wavenumber is calculated from the slope of the phase ramp.

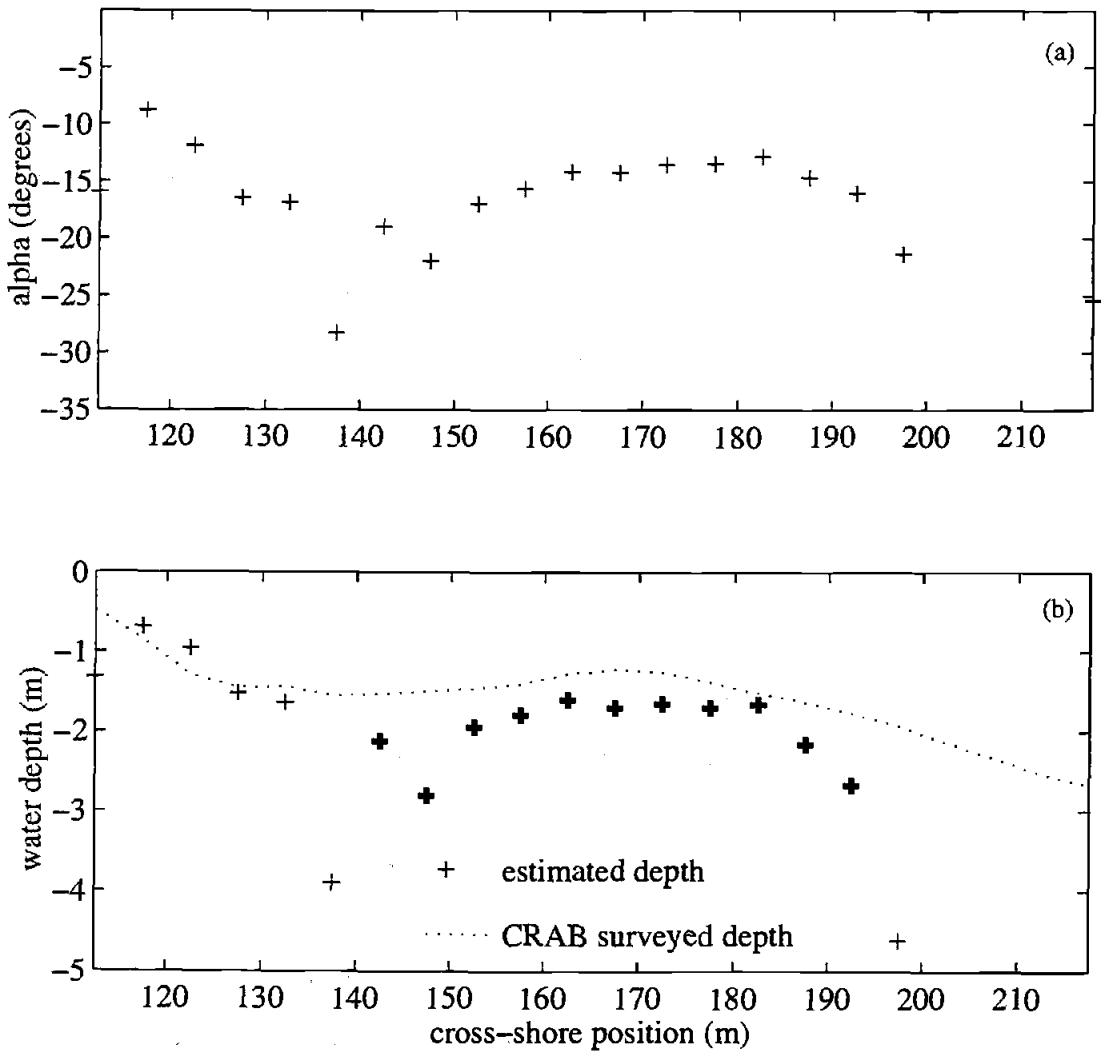

Figure 4.11 Wave angle (a) and water depth (b) estimates for October 8, 1990 at 1612 GMT. The wave angle (a) is shown to refract towards the shoreline as it shoals. Magnitude and sign are generally consistent with the wave angle measured in 8 m water depth (-35°). Estimated water depths (b) are shown to be consistent with surveyed water depths (RMS difference error = 0.613 m) in areas of the profile where CEOF amplitudes are greater than 0.70 (bold symbols).

In the area of the profile associated with the onset of breaking, waves evolve from a sinusoid to a steep and peaky form as they begin to shoal and break, and nonlinear mixing occurs between frequencies. Video techniques for detecting propagating waves are dominated by signals near the wave crest. Just before breaking, the peaky crests created by the harmonics of the fundamental frequency shift forward . The video techniques tend to track this forward pitching face of the wave rather than the wave phase associated with the fundamental frequency which actually lies seaward of the steep face. In this region, the phase speed as measured with video data will appear faster than the true speed of the incident waves due to the evolving form of the waves resulting from nonlinearities associated with shoaling.

The relationship between wave form and the intensity signal is described by a MTF. At the break point, the MTF phase changes rapidly from the specular offshore phase to the diffuse scattering signature in the surf zone. While both are coherent and spatially stable in phase, they are distinctly different and individual to the signature of the wave in each region. In the region of the profile marked by both breaking and non-breaking waves, a mix of the two different MTF's will beat down the coherence between adjacent sensors.

The region of the break point can be identified by areas of high intensity along a cross-shore transect. A peak in a plot of mean intensity across the array (Figure 4.12) defines the position of the break point to be located around x = 180 m over an offshore sand bar. In this region, the low amplitudes from the first mode of the CEOF and resulting poor depth estimates maybe be attributed to the strong shift in the MTF.

The location of the onset of breaking, where results are expected to be in error, shifts with tidal elevation. Thus, use can be made of estimates from a range of tides to provide stable measure of depth across the entire profile. Mean averages of depth estimates throughout one tidal cycle were compared to survey depths and the RMS difference errors were calculated (Figure 4.13). The depth at x = 142.5 m was generally overestimated with

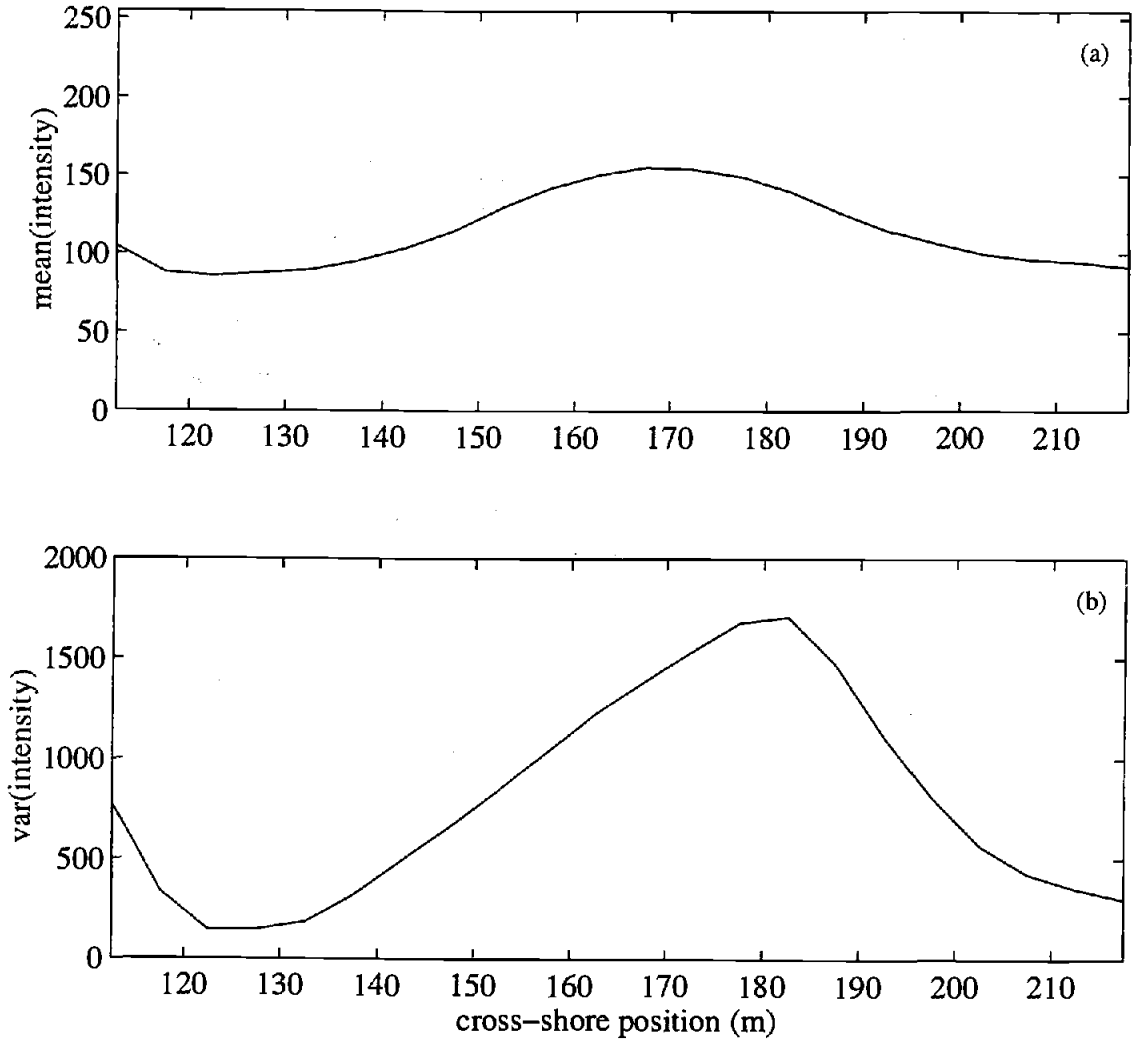

Figure 4.12 Mean (a) and variance (b) of pixel intensity at each cross-shore position for October 8, 1990 at 1612 GMT. The increasing mean intensity (a) observed at x = 190 m is associated with the onset of breaking. The region of breaking can also be seen in the increased intensity variance at x = 180 m.

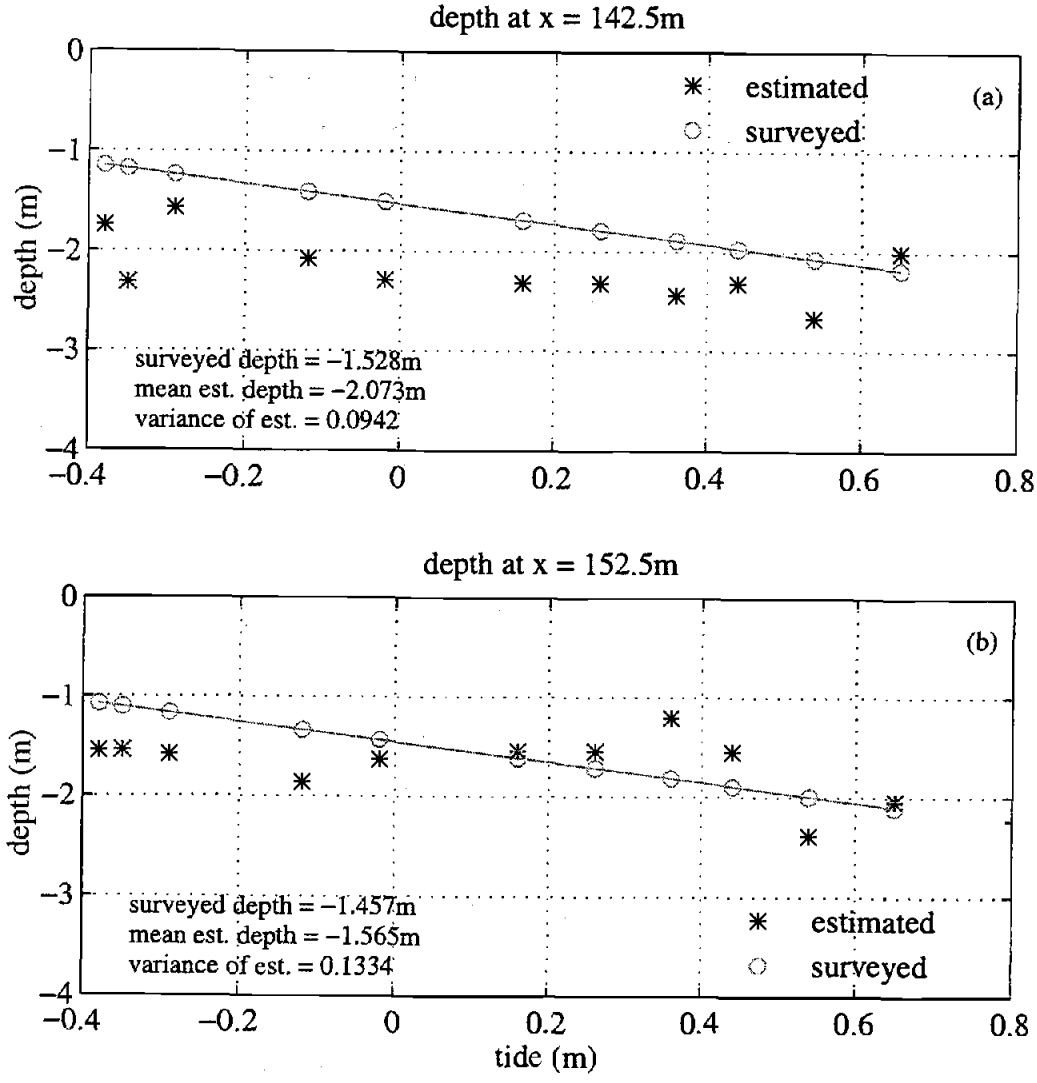

Figure 4.13 Variations of depth estimates from October 8, 1990 at x = 142.5 m (a) and x = 152.5 m (b) through a tidal cycle. Estimates at a particular location are shown to vary with the tide. Averaging estimated water depths over a tidal cycle results in a more reliable approximation of depth.

a mean water depth of –2.07 m. The variance of the estimates at this location was 0.094 and the RMS difference error was 0.73 m. The water depth estimated closer to the bar crest at x = 152.5 m was –1.57 m. The variance associated with the estimates at this location was 0.133 while the RMS difference error was 0.65 m. Estimates of depth at a particular cross-shore position were generally consistent with changes in the tide. For example, in Figure 4.13(a), the estimated depth at this location was deeper during high tide than during low tide. Averaging water depths over the tidal cycle is seen to result in a more reliable estimate of water depth as breaking patterns change with the tide.

4.2 Duck, North Carolina Argus Station

The accuracy of the technique was tested using intensity data routinely collected from the Argus Station located in Duck, North Carolina. An Argus Station is a long-term remotely-operated video camera connected to a PC-based image processor. Hourly snapshots and time exposures of the surf zone are downloaded to a central computer each night and added to a continually growing database of video images [*Holman, et al.*, 1993]. Argus Stations are currently located in Oregon, North Carolina, California, Hawaii, the Netherlands, England, and Australia. The site in Duck provides an excellent place to test the video technique because regular bi-weekly offshore surveys are conducted at the site and can serve as ground truth for estimated depths. In March 1997, the collection of intensity timestacks was incorporated into the hourly sampling routine of snapshots and time exposures at Duck. This will continue to be an ongoing part of the automatic video data collection at the site.

The results presented here are from data collected between April 1 and June 17, 1997. Each timestack of intensity data represents a 17 minute run sampled at a rate of 1 Hz. During this three month period, a total of 794 data runs were analyzed, spanning a wide variety of wave conditions and beach morphologies.

Six CRAB surveys of offshore bathymetry were conducted during the study period on April 3, April 5, April 30, May 14, June 10 and June 17, 1997 (Figure 4.14). These surveys serve as ground truth for the profiles estimated during the three month study period. Vertical changes in the offshore profile during the five CRAB surveys exceeded 1 m in some locations along the profile (b).

Wave data for this period were obtained from the 8 m array located slightly northeast of the FRF pier (Figure 4.2). Data on incident frequency, wave height, and wave angle were computed as means over three-hour sampling periods (Figure 4.15). Tide data were available for this period from the NOAA tide gauge located at the end of the pier. The ready-availability of these data at the site provides an ideal opportunity for ground truth testing of the technique.

The pixel sampling array designed for the Duck Argus Station camera C0 (Figure 4.16) is centered at FRF coordinate y = 1100 m. The cross-shore array, composed of 19 sensors spaced 10 m apart, extends 180 m offshore from the shoreline location at approximately x = 110 m. Six longshore arrays were evenly spaced 25 m apart throughout the cross-shore array. Each longshore array contained six pixel locations spaced 10 m apart.

4.2.1 Water Depth Analysis

Water depths were calculated at each position in the array for every timestack collected between April 1 and June 17, 1997 using the techniques described in Chapter 3. The analyses were conducted similarly to those completed for the Delilah data set; however, the spectra were calculated using 42 degrees of freedom and a bandwidth of 0.0205 s^{-1}. For each of the 18 cross-shore position pairs, depth estimates were made for all of the 794 times resulting in approximately 12704 independent realizations of water depth. Before examining the statistics of the whole set of results from the Duck Argus

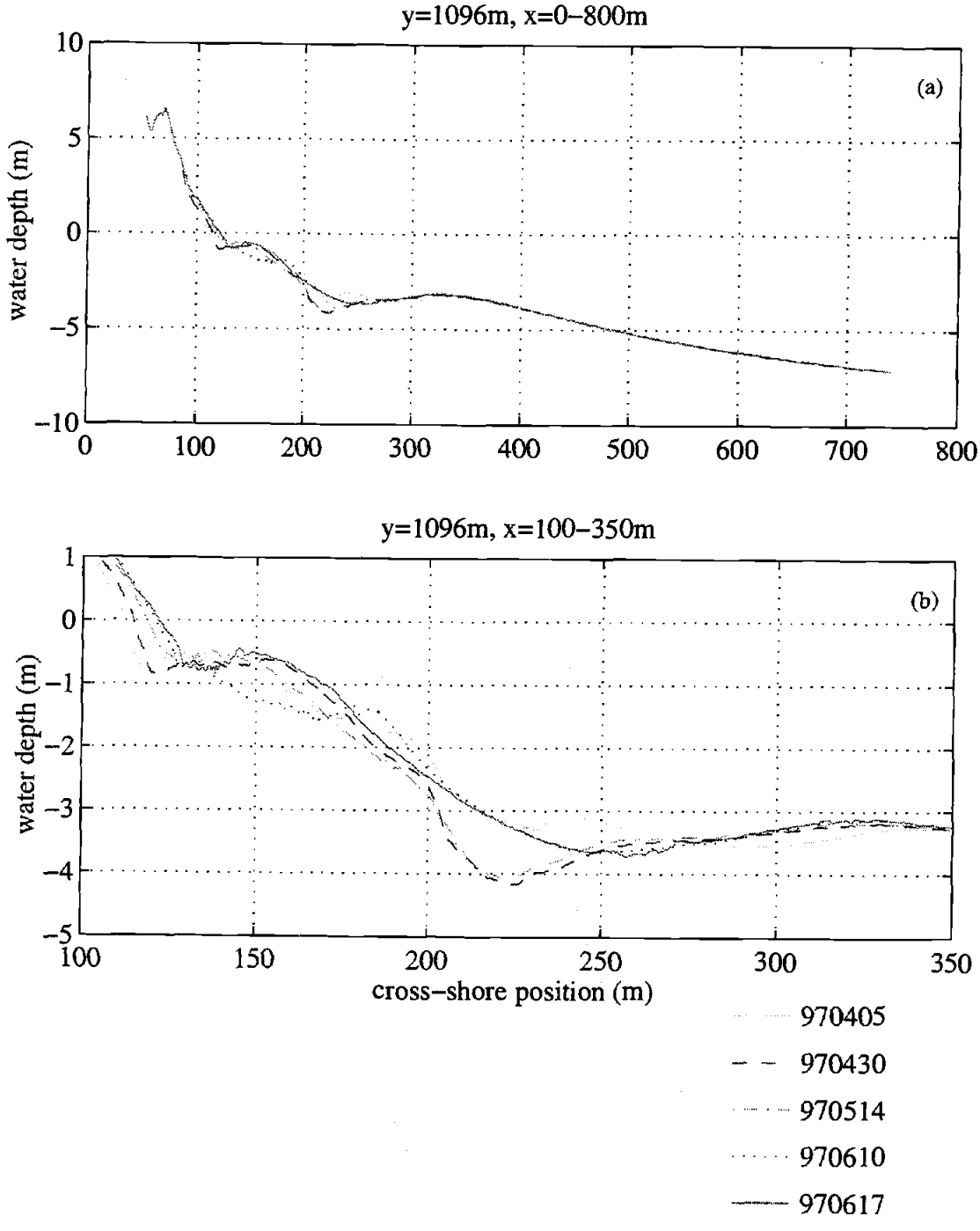

Figure 4.14 CRAB surveyed profiles at Duck, North Carolina from April 4, 1997 to June 17, 1997. The survey line, located along the north property line at the FRF (y = 1096 m), extends approximately 650 m offshore (a). Changes of up to 1 m are observed in the region of focus for this study (b).

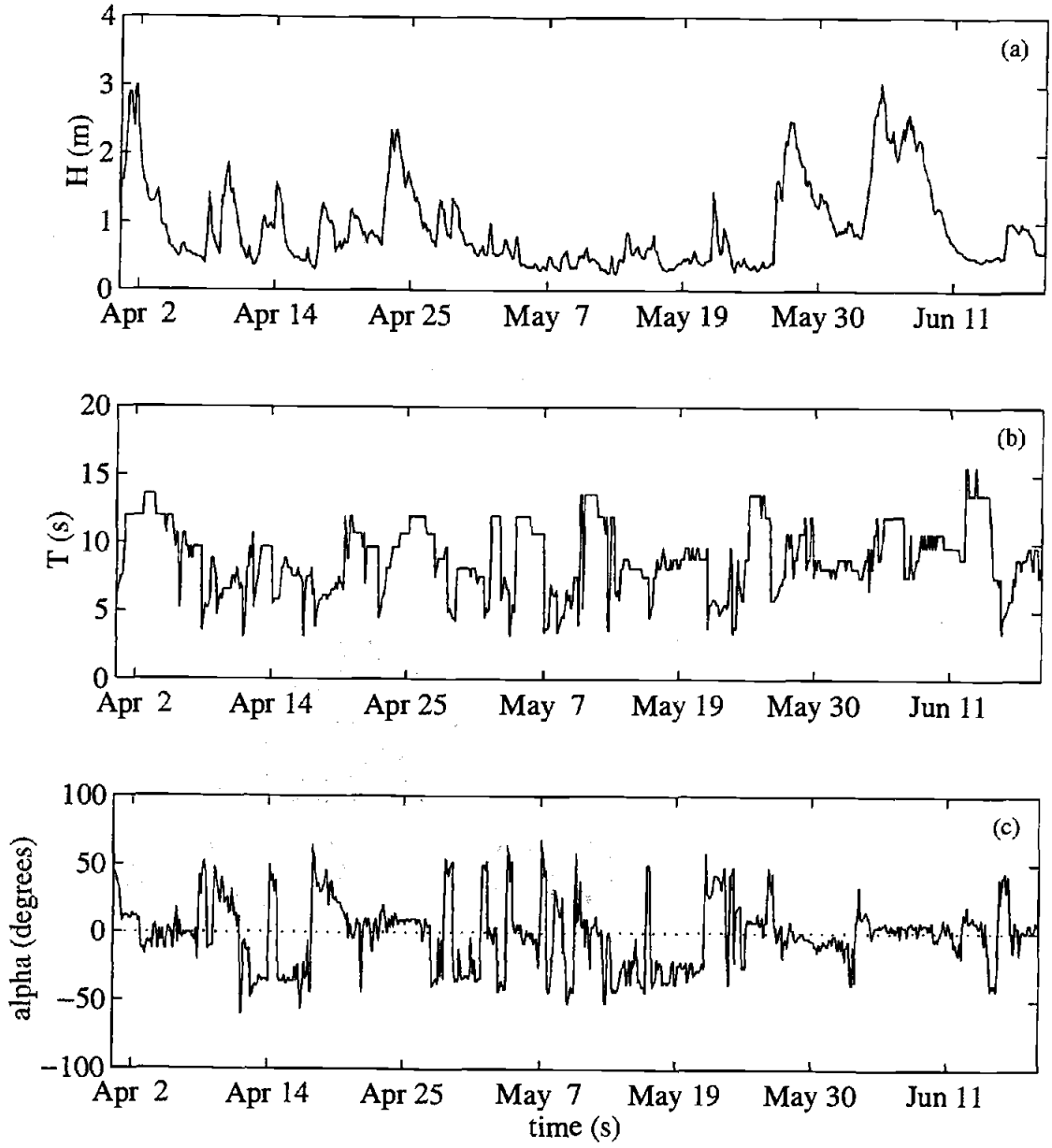

Figure 4.15 Significant wave height, wave period, and wave angle measured in 8 m water depth in Duck, North Carolina from April 1 to June 17, 1997.

Figure 4.16 Pixel array for the Argus Station in Duck, North Carolina. The cross-shore array (+), located in the longshore at y = 1100 m (just north of the property line at the FRF), consists of 19 pixel sensors spaced 10 m apart, extending 180 m offshore. Four longshore arrays (O) are spaced 25 m in the cross-shore and each contain six pixel locations also spaced 10 m apart.

Station, the data were screened based on three criteria that eliminated physically impossible or statistically unstable estimates:

1. The first criteria was that only onshore phase speed would be used in the estimation of water depth. In the coordinate system defined for Duck, a wave moving towards the shore would be moving in a negative x direction corresponding to a negative wavenumber. We limited our depth estimates to those instances where the wavenumbers calculated from the CEOF were negative.

2. Second, analysis was limited to deep water waves. Therefore, wavelengths were only considered if they were less than 0.9 times the theoretical deep water wavelength (see previous discussion in Chapter 3).

3. Finally, estimated depths were only considered for which the corresponding amplitude from the CEOF was greater than 0.70. Low amplitudes may be an indication of a very noisy signal or low coherence between adjacent sensors.

Screening the initial results using the above criteria eliminated approximately 75% of the estimates from the data set. The remaining 3000 points were used to calculate bulk statistics on the accuracy of the technique. These statistics were used to determine confidence intervals for the estimates and to examine the validity of the technique and the conditions under which the estimates were most consistent with ground truth data.

4.2.2 Definitions of Statistics Describing Performance

The data set was sub-divided into one week periods of time; therefore, at each cross-shore position, from a few to as many as 100 tide-corrected depths, $h_i(x)$, were estimated. There are a variety of possible methods to best determine a single estimated depth, $\hat{h}(x)$, from the set of individual estimates collected over the week's span.

The most obvious way is to first look at the mean water depth at each location, $\bar{h}(x)$, which is defined as

$$\hat{h}(x) = \bar{h}(x) = \frac{1}{N}\sum_{i=1}^{N} h_i(x) \tag{4.1}$$

where N is the number of observations of depth at each cross-shore position [*Bendat and Piersol*, 1986].

By nature of the video analysis, depths are constrained to always be less than zero (depth is defined as a negative value). Thus, estimates can only be slightly too shallow but, potentially, can be much too large. Averaging by an arithmetic mean can therefore be biased too deep. An alternate method for obtaining a single value from a set of estimates and for helping to reduce the bias is to calculate the geometric mean. The geometric mean is simply the sample mean calculated in log space and can be defined as

$$\hat{h}(x) = \bar{h}_g(x) = \exp\left(\frac{1}{N}\sum_{i=1}^{N} \ln(h_i(x)\ )\right). \tag{4.2}$$

The geometric mean is useful when looking at data whose values are constrained at one end.

Two further measures can be defined from the probability distribution function (pdf) of the estimates for any one location. The median is the value for which 50% of the estimates are greater and 50% of the estimates are less [*Davis*, 1973]. It is often considered to be the most robust measure since it is less sensitive to outliers. The mode is the value that occurs with the greatest frequency and can be identified by the peak of a probability density function. The mode, while being the most probable value, is also the values that is most sensitive to details in the pdf; therefore, it is the least stable estimate.

For a symmetric frequency distribution, the mean, median and mode are the same value. However, for an asymmetric frequency distribution, as is the case with the depth estimates, the mean, median and mode represent three distinct values. In order to

determine the best representation for the suite of water depths at each cross-shore position, averaged weekly profiles are calculated using each method and then bulk error statistics are used to evaluate the performance of each estimator.

Any approximation of a single value from a set of values will have a confidence interval about the estimate based on the variance of the data around the estimate. The central limit theorem states that the mean of a set of N random variables will be normally distributed with an expected value of μ, the population mean, and a variance of s^2/N, where the sample variance s^2 is calculated as

$$s^2(x) = \frac{1}{N}\sum_{i=1}^{N}(h_i(x) - \bar{h}(x))^2 \tag{4.3}$$

[*Bendat and Piersol*, 1986].

The confidence interval of the estimate is then calculated as the probability with which the estimated value will be within one standard deviation of the true value. Based on the central limit theorem, an error associated with the estimates, E(x), can be defined as

$$E(x) = \frac{1.96s(x)}{\sqrt{N}} \tag{4.4}$$

where s is the standard deviation of the estimates. A 95% confidence interval for the mean true water depth, $h_t(x)$, based on an estimated mean water depth, $\bar{h}$, and the sample variance is given by the following probability statement

$$P\left\{\bar{h}(x) - E < h_t(x) < \bar{h}(x) + E\right\} = 0.95 \tag{4.5}$$

[*Bendat and Piersol*, 1986]. This definition is only valid for confidence intervals for the arithmetic mean. However, we also used this value as a proxy for the confidence interval for the geometric mean, median and mode. $E(x)$ provided us with a useful measure of the spread in the estimates, $\hat{h}$, around the central value and allow for the creation of confidence intervals around each estimate.

Each seven-day average estimate was compared to CRAB surveyed profile data to examine the accuracy of the video technique. However, CRAB surveys were collected on

average only every three weeks. As a results, some of the estimated profiles may potentially be compared to a CRAB profile that is out of date. Based on the evolution of the profile between successive surveys, an error on the ground truth data was created to serve as a measure of the validity of the ground truth for the estimates to which it is being compared. The error in the ground truth data at each cross-shore position, x, for each time, t, is defined to be

$$\Delta(x,t) = \left(h_t(x,t_2) - h_t(x,t_1)\right)\left(\frac{t-t_1}{t_2-t_1}\right) \tag{4.6}$$

where $h_t(x,t_1)$ is the survey being compared to the estimates, $h_t(x,t_2)$ is the next closest survey, t_1 is the time of the comparison survey, and t_2 is the time of the next closest survey (which may proceed or follow t_1). Negative error is indicative of erosion between successive surveys while a positive error is representative of accretion. On plots of the estimated profile compared to the surveyed profile, the $\Delta(x,t)$ is plotted to provide an envelope of possible true depths represented by the two surveys.

Once the average estimated profile had been determined, confidence intervals established, and an error on ground truth defined, bulk statistics on the estimated profile were calculated to evaluate the performance of each of the four techniques for estimating water depth (mean, geometric mean, median and mode). Two basic quantities were used to investigate the accuracy of the estimates: a ratio error and a difference error.

The first statistic is a direct comparison between the estimates and the true values, a normalized depth estimate,

$$R(x) = \frac{\hat{h}(x)}{h_t(x)}, \tag{4.7}$$

where a value of 1 is representative of perfect agreement between the estimates and the true value. The mean ratio error can be calculated across the entire profile for each weekly estimate by

$$\overline{R} = \frac{1}{N_x}\sum_{i=1}^{N_x} R(x_i) \tag{4.8}$$

where N_x is the number of cross-shore locations. A weighted mean can also be calculated across the profile as

$$\overline{R}_w = \frac{\sum_{i=1}^{N_x} R(x_i) \Big/ \mathrm{E}(x_i)}{\sum_{i=1}^{N_x} 1 \Big/ \mathrm{E}(x_i)}. \tag{4.9}$$

This estimate de-weights the values that have high error bars associated with them (those in which you have little confidence) and puts more weight on the estimates with narrower confidence intervals.

The second quantity investigated is a difference error which is defined to be

$$D(x) = \hat{h}(x) - h_t(x) \tag{4.10}$$

Based on this definition, a difference error of 0 indicates total agreement between the estimates and the ground truth. A negative value of D indicates an overestimate, as water depths in this study are defined to be negative. A mean difference across the profile and a weighted mean difference can be calculated following the formulation above, equations (4.8) and (4.9).

Finally, estimates can have zero bias but still be noisy. The root mean square (rms) error of the differences, calculated as

$$D_{rms} = \sqrt{\frac{1}{N}\sum_{i=1}^{N} D(x_i)^2}, \tag{4.12}$$

is used to measure the scatter of mean differences. A weighted rms error is calculated to account for the varying degree of confidence in each estimate. The weighted rms difference error is calculated as

$$\overline{D}_{w\_rms} = \frac{\sqrt{\frac{1}{N_x}\sum_{i=1}^{N_x} D(x_i)^2 \Big/ \mathrm{E}(x_i)^2}}{\sqrt{\frac{1}{N_x}\sum_{i=1}^{N_x} 1 \Big/ \mathrm{E}(x_i)^2}}. \tag{4.13}$$

These six bulk statistics were calculated for each profile estimated using the four techniques previously described. They serve to evaluate the performance of the estimators and allow the selection of one method as the most appropriate estimator for future analyses.

4.2.3 Evaluation of Depth Estimators

For each weekly subset of depth data, a single water depth was calculated at each cross-shore position using the four techniques described in section 4.2.1. Figure 4.17 presents the estimated profile based on the four methods for April 8, 1997. Panels show estimates derived, top to bottom, from the arithmetic mean, the mode, the geometric mean, and the median. The mean and geometric mean of the estimated depths are shown to be more biased towards the deeper water depths than the median. In this example, $(\overline{R}_w)_{mean} = 1.156$ while $(\overline{R}_w)_{median} = 1.059$. In this case, the mode, $(\overline{R}_w)_{mode} = 1.039$, and the median more accurately estimated the true water depth. In general, the most accurate estimates tended to occur where the confidence interval were the smallest, and consequently were the most believable of the estimates.

Figure 4.18 presents an example from May 6, 1997 that illustrates the more dramatic differences between the four techniques resulting from the anomalously large error bars associated with this time period. The most variability was seen at locations where error bars were high. For example, at x = 185 m, the water depth was estimated to be too deep and the error bars were large. The mode estimates brought the value at this location closer to the true depth while moving other estimates further from the true depth. The geometric mean generally brought all estimates closer to the survey profile, but there was still a small bias towards the deeper estimates. The median, however, generally provided a more robust estimate for the true water depth, $(\overline{R}_w)_{median} = 1.526$ and $(\overline{D}_{w\_rms})_{median} = 1.289$ m, for all eleven estimated profiles.

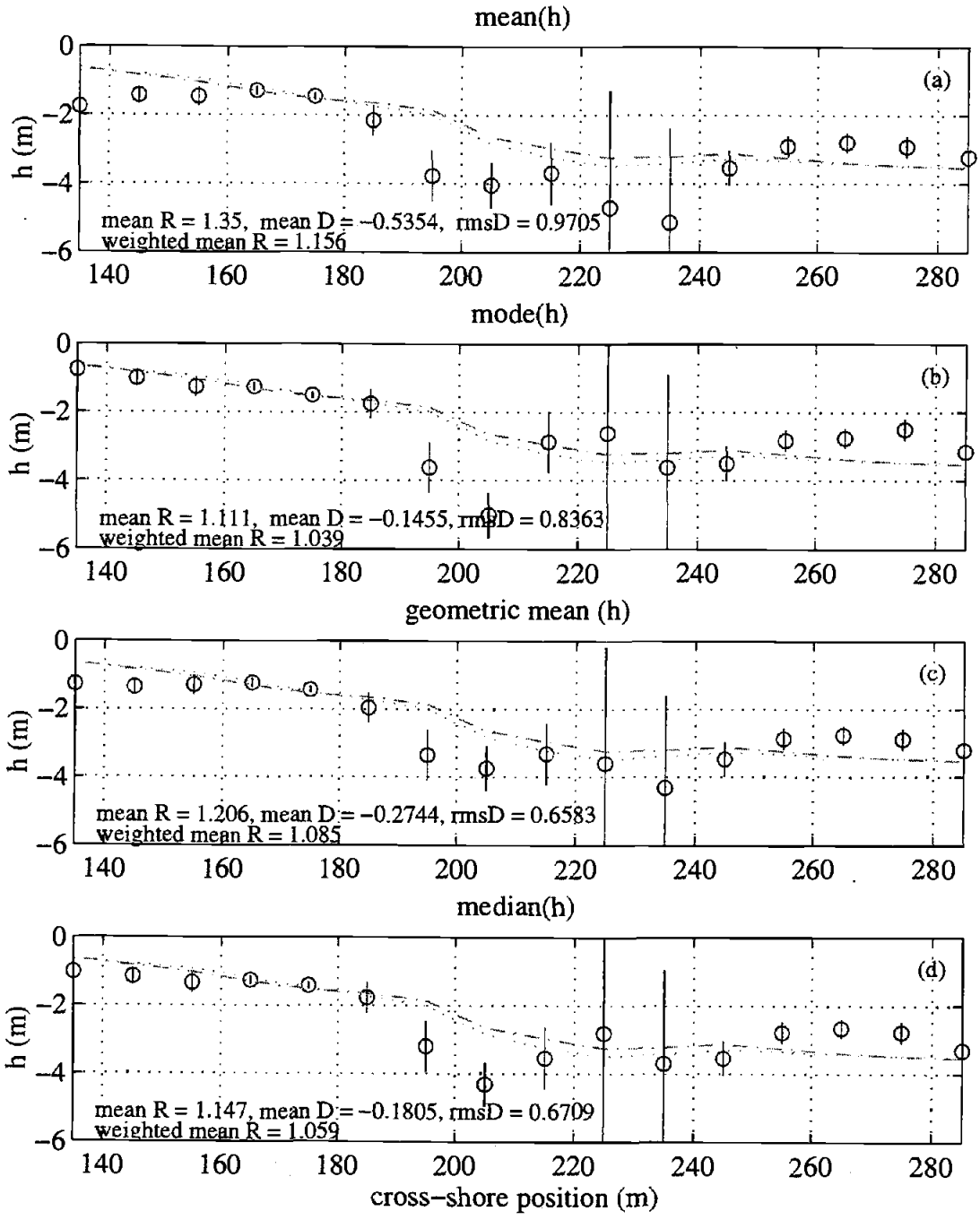

Figure 4.17 Estimated offshore profile at Duck, North Carolina for April 8, 1997. The four profiles represent a seven-day averaged profile calculated as the mean (a), the mode (b), the geometric mean (c), and the median (d) of all estimates at cross-shore position x. Error bars on depth represent the 95% confidence interval based in the standard deviation of the estimates about the mean. The dashed line shows the surveyed profile, the dotted line is an error bound on the ground truth, R represents the ratio of estimated water depth to true water depth, and D represents the difference between the two measures.

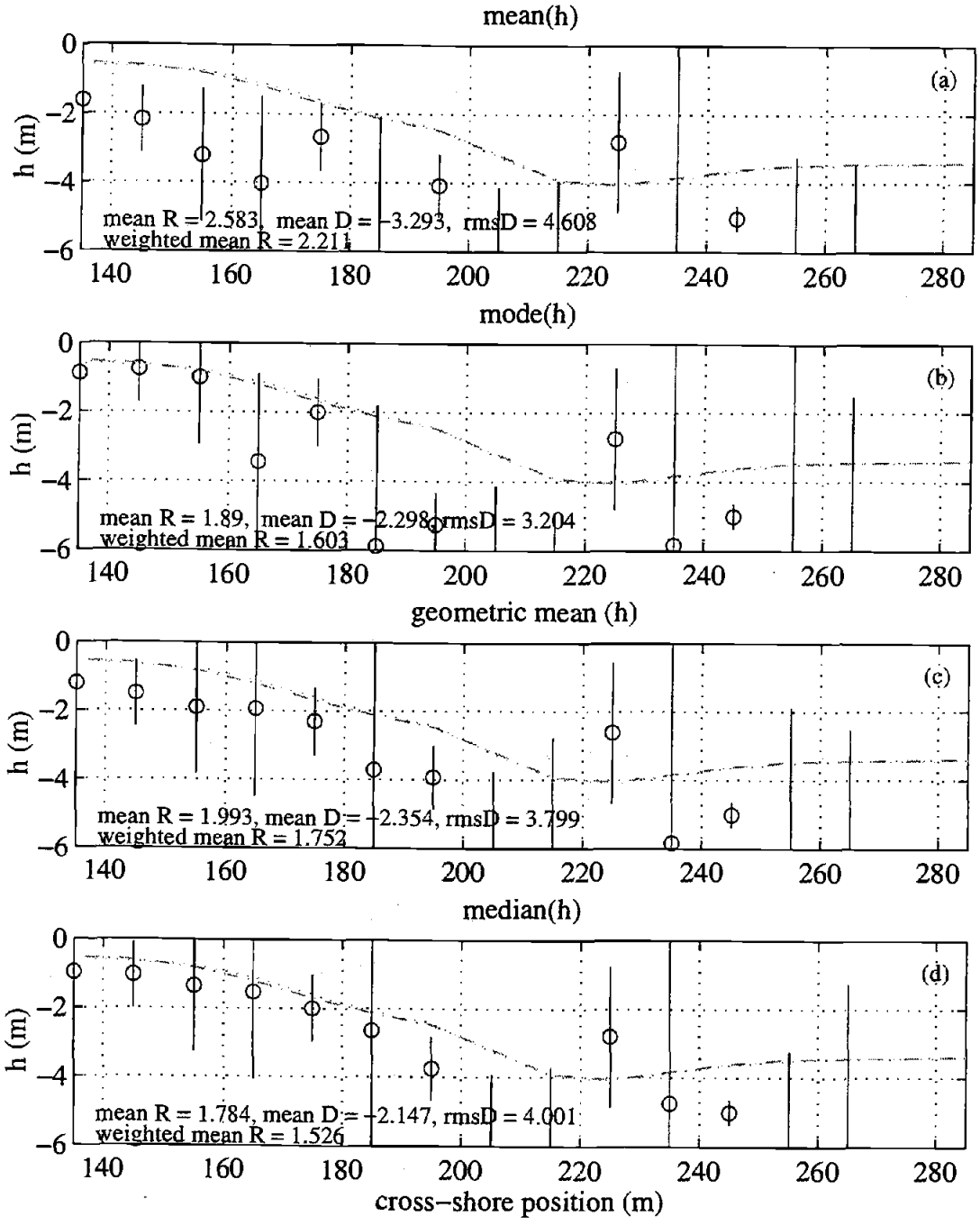

Figure 4.18 Estimated offshore profile at Duck, North Carolina for May 6, 1997. The four profiles represent an averaged weekly profile calculated as the mean (a), the mode (b), the geometric mean (c), and the median (d) of all estimates at cross-shore position x. Error bars on depth represent the 95% confidence interval based in the standard deviation of the estimates about the mean. Note the variability of the profile as calculated by the four different estimators.

Bulk statistics for the ratio errors are presented in Table 4.1. The median is generally shown to provide a more accurate estimate of the water depth over all times. The mean of the $\overline{R}$ calculated over all times was closest to 1, an indication of an accurate estimate, using the median depth as the representation for the set of estimates, $mean(\overline{R})_{median}$ = 1.448. However for the weighted estimates (Table 4.1.b), both the mode and the median provided equally accurate estimates of depth.

Mean difference errors and weighted mean difference errors are presented in Table 4.2. Using this measure of error, values closer to 0 are indicative of more accurate estimates. According to this statistic, the median value was a more accurate measure of water depth based on a $mean(\overline{D})_{median}$ = -0.942 m and a $mean(\overline{D}_w)_{median}$ = -0.407 m.

Finally the rms difference errors and weighted rms difference errors are presented in Table 4.3. The rms error measures the scatter of the estimates about the true value. Again, the median value provided the most accurate estimate of water depth as seen by the low mean value, $mean(D_{w\_rms})_{medan}$ = 0.672 m, over the eleven week span.

The tables presented indicate that the best method for selecting a single depth estimate out of a suite of estimates is to determine the median of the values. The mean ratio error between the median depth and the true depth was 1.49 over the eleven week period. The ratio error weighted by the confidence interval associated with each depth was 1.34. Generally, the estimated water depths were 34% deeper than the actual surveyed water depths. The time-averaged difference error, ideally equal to 0, was -0.942 m while the weighted value was -0.407 m. Negative rms errors indicate that the video technique generally overestimated the true water depth. Finally, the eleven week averaged rms difference error for the median was 1.864 m and the corresponding weighted error was 0.672 m. Video-based depth estimates calculated as the median depth at each cross-shore location can be expected to be within approximately 70 cm of the true water depth.

Table 4.1.a. Mean Ratio ($\overline{R}$)

Date	Mean	Mode	Geometric mean	Median
Apr01 - Apr07	1.585	1.142	1.304	1.238
Apr08 - Apr14	1.350	1.111	1.206	1.147
Apr15 - Apr21	1.581	1.604	1.433	1.337
Apr22 - Apr28	1.767	1.630	1.514	1.451
Apr29 - May05	1.759	1.626	1.506	1.479
May06 - May12	2.583	1.890	1.992	1.784
May13 - May19	1.766	1.274	1.445	1.270
May20 - May26	2.332	1.636	1.843	1.712
May27 - Jun02	1.606	1.589	1.510	1.446
Jun03 - Jun09	2.627	1.831	1.981	1.958
Jun10 - Jun16	2.169	1.870	1.714	1.549
mean($\overline{R}$)	1.921	1.564	1.587	1.488

Table 4.1.b. Weighted Mean Ratio ($\overline{R_w}$)

Date	Mean	Mode	Geometric mean	Median
Apr01 - Apr07	1.270	1.056	1.146	1.111
Apr08 - Apr14	1.156	1.039	1.085	1.059
Apr15 - Apr21	1.188	1.120	1.118	1.084
Apr22 - Apr28	1.637	1.526	1.476	1.481
Apr29 - May05	1.475	1.420	1.395	1.420
May06 - May12	2.211	1.603	1.752	1.526
May13 - May19	1.573	1.250	1.404	1.318
May20 - May26	1.650	1.325	1.457	1.342
May27 - Jun02	1.418	1.366	1.374	1.366
Jun03 - Jun09	1.922	1.415	1.555	1.456
Jun10 - Jun16	1.971	1.594	1.676	1.553
mean($\overline{R_w}$)	1.589	1.338	1.403	1.338

Table 4.2.a. Mean Difference Error ($\overline{D}$)

Date	Mean (m)	Mode (m)	Geometric mean (m)	Median (m)
Apr01 - Apr07	-0.705	-0.113	-0.341	-0.230
Apr08 - Apr14	-0.535	-0.145	-0.274	-0.181
Apr15 - Apr21	-0.696	-0.762	-0.400	-0.228
Apr22 - Apr28	-1.576	-1.319	-0.964	-0.737
Apr29 - May05	-1.159	-0.986	-0.729	-0.653
May06 - May12	-3.293	-2.298	-2.354	-2.147
May13 - May19	-1.362	-0.624	-0.764	-0.328
May20 - May26	-3.115	-1.664	-2.028	-1.876
May27 - Jun02	-1.271	-1.164	-1.049	-0.866
Jun03 - Jun09	-3.358	-2.250	-2.302	-2.409
Jun10 - Jun16	-1.906	-1.392	-1.073	-0.705
mean($\overline{D}$)	-1.725	-1.156	-1.120	-0.942

Table 4.2.b. Weighted Mean Difference Error ($\overline{D}_w$)

Date	Mean (m)	Mode (m)	Geometric mean (m)	Median (m)
Apr01 - Apr07	-0.307	0.009	-0.136	-0.084
Apr08 - Apr14	-0.136	0.007	-0.032	-0.008
Apr15 - Apr21	-0.059	0.025	0.063	0.127
Apr22 - Apr28	-0.670	-0.445	-0.409	-0.328
Apr29 - May05	-0.399	-0.297	-0.292	-0.283
May06 - May12	-1.770	-1.351	-1.277	-1.085
May13 - May19	-0.660	-0.298	-0.437	-0.279
May20 - May26	-0.812	-0.525	-0.608	-0.501
May27 - Jun02	-0.530	-0.408	-0.447	-0.399
Jun03 - Jun09	-1.820	-1.128	-1.221	-1.109
Jun10 – Jun16	-1.090	-0.746	-0.705	-0.530
mean($\overline{D}_w$)	-0.750	-0.469	-0.500	-0.407

Table 4.3.a. RMS Difference Errors (D_{rms})

Date	Mean (m)	Mode (m)	Geometric mean (m)	Median (m)
Apr01 - Apr07	1.146	0.746	0.689	0.647
Apr08 - Apr14	0.970	0.836	0.658	0.671
Apr15 - Apr21	1.633	2.335	1.242	1.031
Apr22 - Apr28	2.335	2.993	1.551	1.392
Apr29 - May05	2.423	2.805	1.575	1.675
May06 - May12	4.609	3.204	3.799	4.001
May13 – May19	1.777	1.694	1.059	0.658
May20 - May26	4.563	2.194	2.871	3.251
May27 - Jun02	2.354	2.860	2.030	1.810
Jun03 - Jun09	4.796	4.021	3.684	4.333
Jun10 - Jun16	2.294	2.805	1.256	1.036
mean(D_{rms})	2.627	2.409	1.856	1.864

Table 4.3.b. Weighted RMS Difference Errors (D_{w_rms})

Date	Mean (m)	Mode (m)	Geometric mean (m)	Median (m)
Apr01 - Apr07	0.514	0.344	0.436	0.363
Apr08 - Apr14	0.366	0.385	0.320	0.339
Apr15 - Apr21	0.624	0.552	0.602	0.588
Apr22 - Apr28	0.795	0.920	0.656	0.721
Apr29 - May05	0.483	0.523	0.427	0.476
May06 - May12	1.569	1.519	1.348	1.289
May13 - May19	0.667	0.489	0.544	0.482
May20 - May26	0.595	0.463	0.472	0.433
May27 - Jun02	0.668	0.653	0.626	0.628
Jun03 - Jun09	1.859	1.718	1.438	1.541
Jun10 - Jun16	0.827	0.870	0.606	0.534
mean(D_{w_rms})	0.815	0.767	0.680	0.672

4.2.4 Algorithm Performance

In order to investigate the details of when the technique is most accurate and under what conditions the technique may fail, the difference error and the variance associated with each estimate were examined for dependencies on environmental conditions.

First, the accuracy of the technique was examined relative to actual water depths to determine if the technique works better in one region of the profile over another. A gentle trend was observed in the relationship of difference errors to true water depth (Figure 4.19). In shallow water, the technique tended to overpredict the water depth as indicated by the negative values of D. In deeper water, water depths were generally underpredicted as seen the cluster of positive difference errors located between h = -3 m and h = -4 m. This figure also reveals a region of true water depths (h = -1.75 to -3.0 m) where stable estimates are not likely to occur. These depths are associated with the shoreward break in slope just prior to the steeper slopes associated with the presence of a sand bar (Figure 4.14).

The averaged profiles from the Duck Argus Station revealed a visual correlation between overestimates of depth on the steep negative slopes of the seaward face of the sand bar and a corresponding underestimate on the positive sloping shoreward face of the sand bar. Figure 4.20 shows a comparison of the difference errors and the variance of the estimates to beach slope. Figure 4.20(a) reveals that underestimates of depth generally occur on the positively sloping shoreward face of the bar while some of the larger overestimates occur on the steepest, negatively sloped areas of the profile. The smallest errors were associated with the low magnitude, negative slopes (between 0 and -0.02) that represent the majority of the shoaling beach profile.

As mentioned in the results from the Delilah experiment (section 4.1), depths appeared to be overestimated in the region associated with the onset of breaking, a consequence of the spatial shift in the MTF phase as the wave changes form from sinusoid to saw-tooth

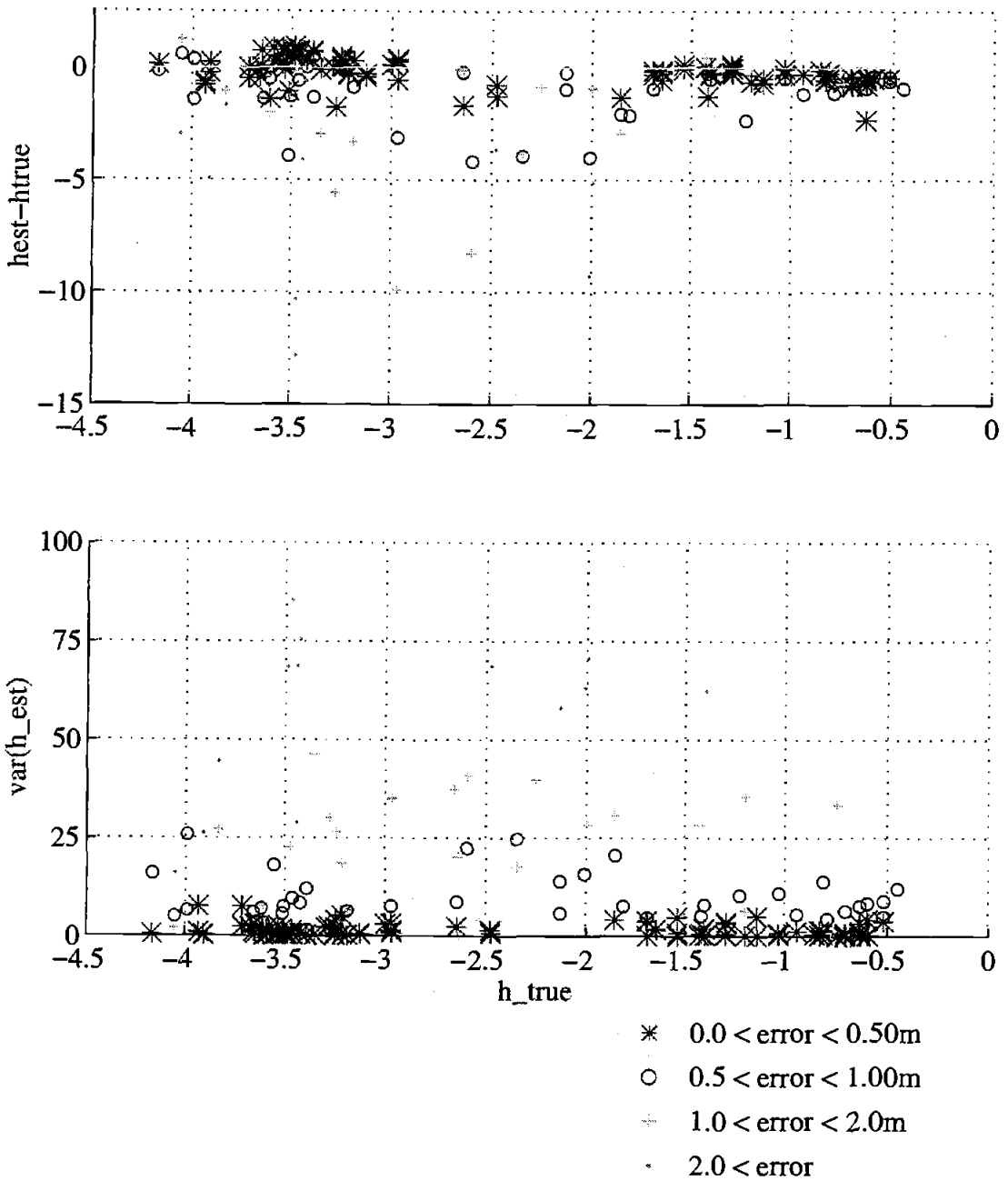

Figure 4.19 Estimated depth error versus true water depth. Estimates are generally overpredicted in shallow water (negative difference errors) and underpredicted in deep water (positive difference errors). Different symbols indicate the confidence interval about each estimate.

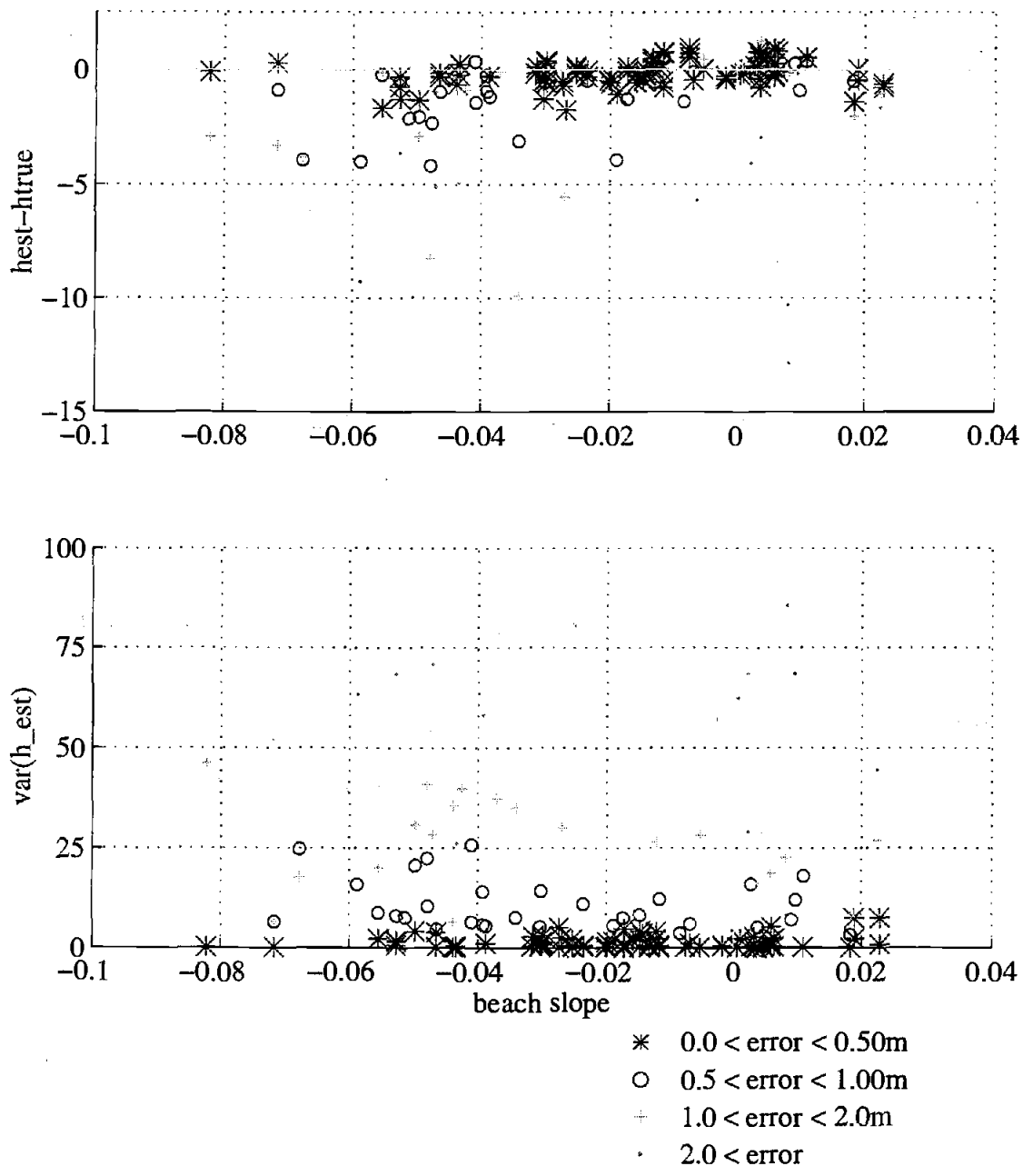

Figure 4.20 Estimated depth error versus beach slope. Difference errors (a) and the variance for each estimate (b) are greater for steep, negative beach slopes associated with the seaward face of the sand bar and the shoreface. Large errors are also observed for positive slopes which represent the shoreward face of the sandbar. The smallest errors occur over less steep negative slopes indicative of a gently shoaling bathymetry.

like. To investigate this phenomenon and the effects on the estimated water depths, difference errors and estimate variance were plotted against the gradient in mean intensity between adjacent cross-shore positions, $d\bar{I}/dx$ (Figure 4.21). The onset of breaking is identified by a high magnitude, negative gradient in intensity, as the signature of the wave changes from a dark face to white foam associated with breaking. A positive gradient is generally associated with wave reformation within the surf zone after breaking. Errors were expected to increase as the magnitude of the negative gradients increased. While this was not observed in the data, Figure 4.21 does illustrate that the variance of the estimates was significantly more scattered for negative gradients than for positive gradients where the corresponding difference errors were generally low, on the order of 1 m.

It also has been hypothesized that water depth may be overestimated in regions where finite amplitude effects are significant. In these regions, the speed of the wave may be dependent not only on the water depth but also on the local wave height. To investigate the possible effects of finite amplitude, errors were examined with respect to the standard deviation of intensity at each cross-shore position. High standard deviation at one point represents a wide range of intensity values that may serve as a proxy for the progression of high amplitude waves past that point. Figure 4.22 shows the relationship between the difference errors and the variance of the estimates to the standard deviation of intensity. The expected relationship between high standard deviations and the high errors was not observed in either figure.

Figure 4.22, in fact, reveals an opposite relationship between intensity standard deviation and errors in that the highest errors were associated with the lowest standard deviations of intensity. A possible explanation for this relationship may be that if the standard deviation of the intensity is too low, the propagation of waves may not have been detected by the video and, in that case, an accurate estimate of phase speed will not be obtained. Figure 4.21 illustrates that large errors O(5 m) occurred where the gradient of intensity was just less than zero. This relationship may provide additional evidence that

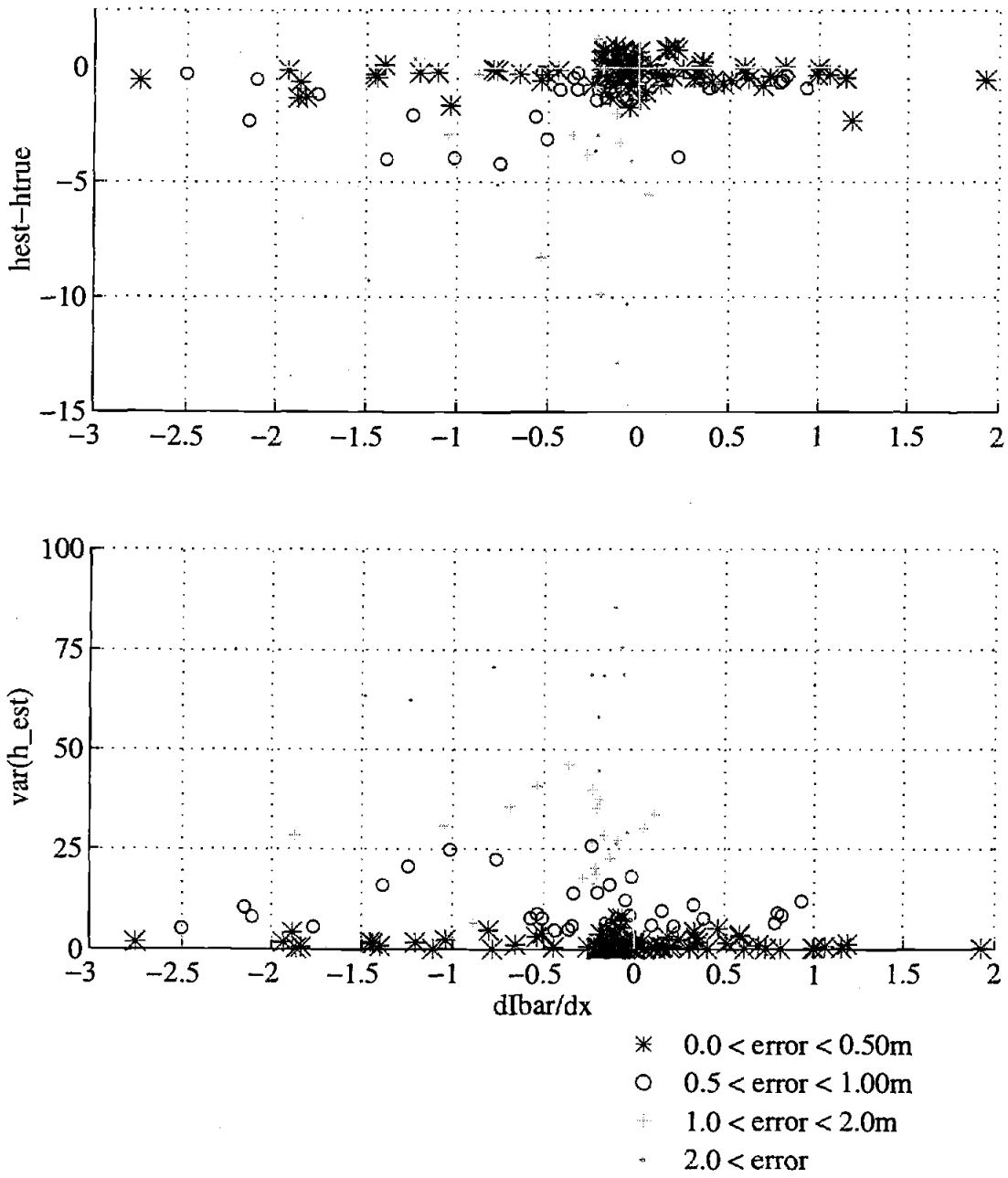

Figure 4.21 Estimated depths error versus the cross-shore gradient in mean intensity. Difference errors (a) and the variance associated with each estimate (b) are greater for negative gradients in intensity. Steep negative gradients in intensity are representative of the onset of wave breaking.

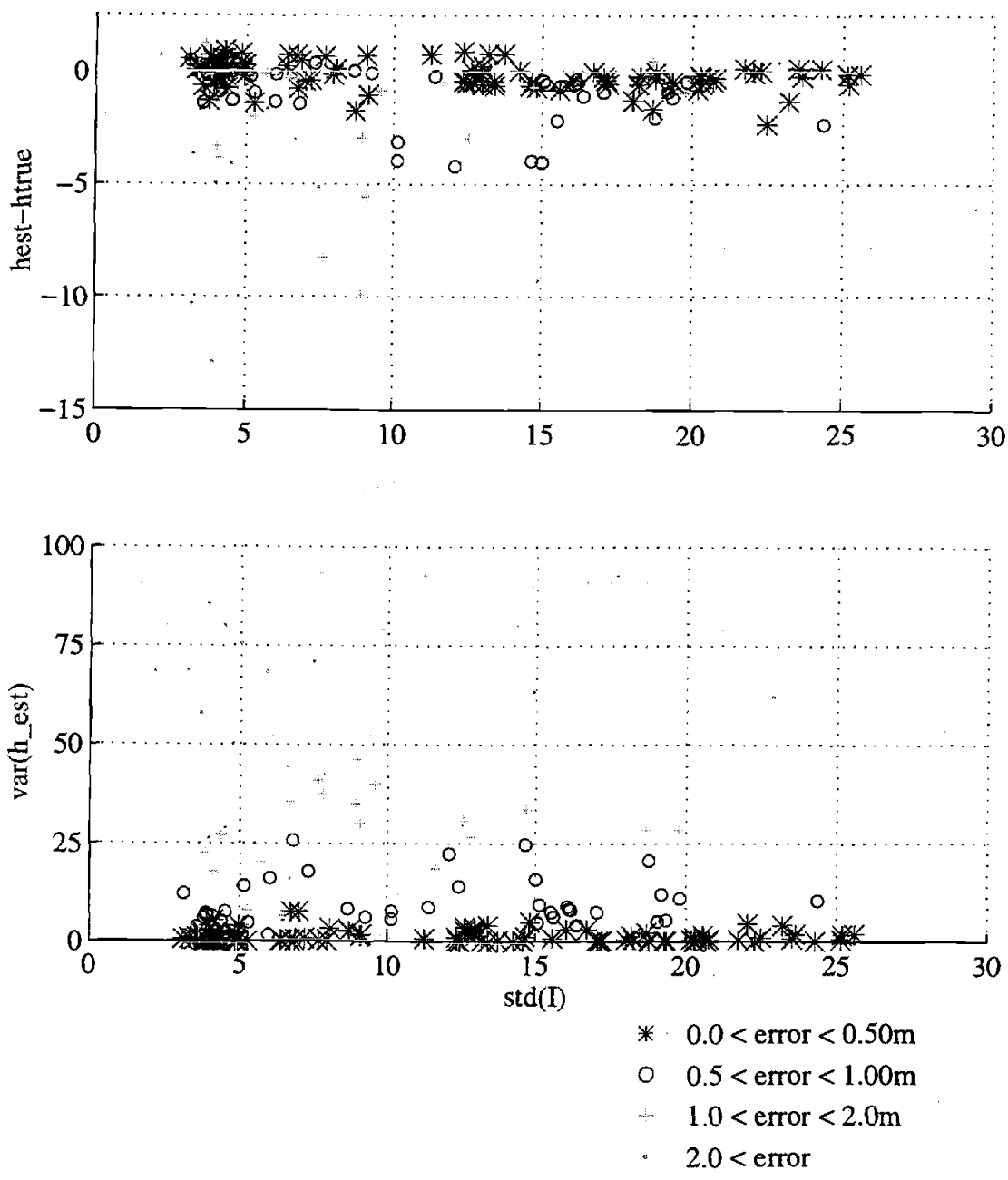

Figure 4.22 Estimated depth error versus standard deviation of intensity, std(I). Difference errors (a) are higher at lower values of std(I). The variance associated with each depth estimate also increases as std(I) decreases (b).

under some wave conditions, correct depth estimates may not be achieved if waves cannot be detected by video through variations in pixel intensity.

The data from the Duck Argus Station provided an excellent opportunity for ground truthing the video technique. Seven-day averages were calculated over a period of eleven weeks using the median depth value at each cross-shore position. This method was shown to improve the accuracy of the estimated profile by reducing the bias towards deeper water depths.

4.3 Agate Beach, Oregon Argus Station

The performance of the depth estimation video technique was also tested on a high energy site in Agate Beach, Oregon using the Argus Station located approximately 122 m above sea level on Yaquina Head. Agate Beach is generally a low sloping, dissipative beach with a broad surf zone that can reach widths up to 1 km. The profile is usually marked by the presence of several offshore sandbars. An oblique time exposure and the rectified plan view, created by mapping the oblique pixel locations onto a scaled grid, shown in Figure 4.23, reveal underlying topography at the site including the presence of a low tide terrace at x = 500 m and a offshore sand bars located at x = 650 m. The spring tide range at this beach can exceed 3 m.

The pixel sampling array designed for the Yaquina Head Argus Station (Figure 4.24) was located at 300 m in the longshore, approximately 250 m south of Yaquina Head. Thirty-one cross-shore sensors, spaced 15 m apart, extended to approximately 300 m offshore. Six longshore arrays were spaced 45 m in the cross-shore. Each array contained nine pixels evenly spaced 15 m apart, centered on the cross-shore array.

The collection of video timestacks at the above described array was added to the routine sampling of snapshots and time exposures of Agate Beach on March 4, 1997 and

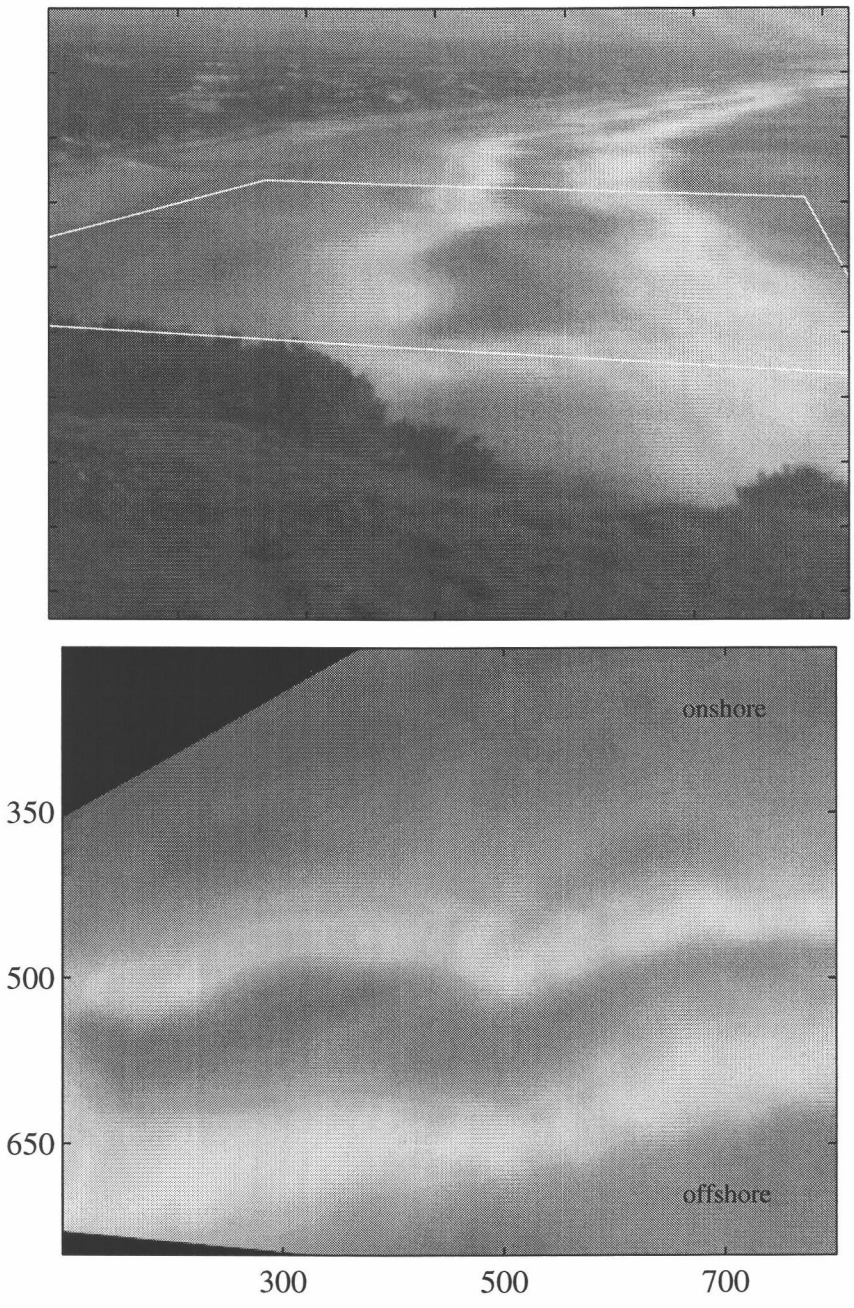

Figure 4.23 Oblique (a) and rectified (b) time exposure from Agate Beach, Oregon on April 4, 1997. The rectified image shows the presence of a shallow terrace near the shoreline at x = 500 m and an offshore sand bar located at x = 650 m.

Figure 4.24 Pixel array for the Argus station in Agate Beach, Oregon. The cross-shore array (+) consists of 31 pixel sensors spaced 15 m apart, extending approximately 450 m offshore. Six longshore arrays (O) are spaced 45 m in the cross-shore and each contain nine pixel locations also spaced 15 m apart.

will continue to be an ongoing part of the video collection at the site. Timestacks are collected every hour at a sampling rate of 1 Hz for 17 minutes. The data analyzed in the following sections were collected between April 1 and June 17, 1997. There are no ground truth surveys available for this site.

4.3.1 Estimated Depths

Water depths were estimated at each cross-shore position in the array for 806 timestacks using the techniques described in Chapter 3. The large data set was then subdivided into eleven one-week long periods to determine an averaged profile for each week. The best estimate for depth at each point in the array was selected as the median of the suite of estimates at each locations (based on the analysis in Section 4.2.3).

Since ground truth data are not available for this site, the performance of the technique was evaluated based on the estimate of a reasonable slope for the profile in addition to consistency between successive estimates. Figure 4.25 contains five of the averaged profiles for April 11, April 28, May 9, May 23 and June 9, 1997. All of the estimates are tide corrected which, due to the large positive tides in the area, can result in both positive and negative water depths. The estimated profiles were remarkably consistent and stable through time as seen by the constant slopes and elevations located between x = 300 m and x = 500 m. Error bars are generally small compared to the span of depths, except in the region of an apparent trough near x = 550 m.

4.3.2 Evaluation of Consistency of Estimates

To examine the consistency of the estimates, a surface mapping of each profile was created to show the evolution of the estimated profile through the eleven week period (Figure 4.26). This figure reveals a region of relative estimated profile stability from about x = 325 – 475 m and a second region further offshore from x = 600 – 700 m. More

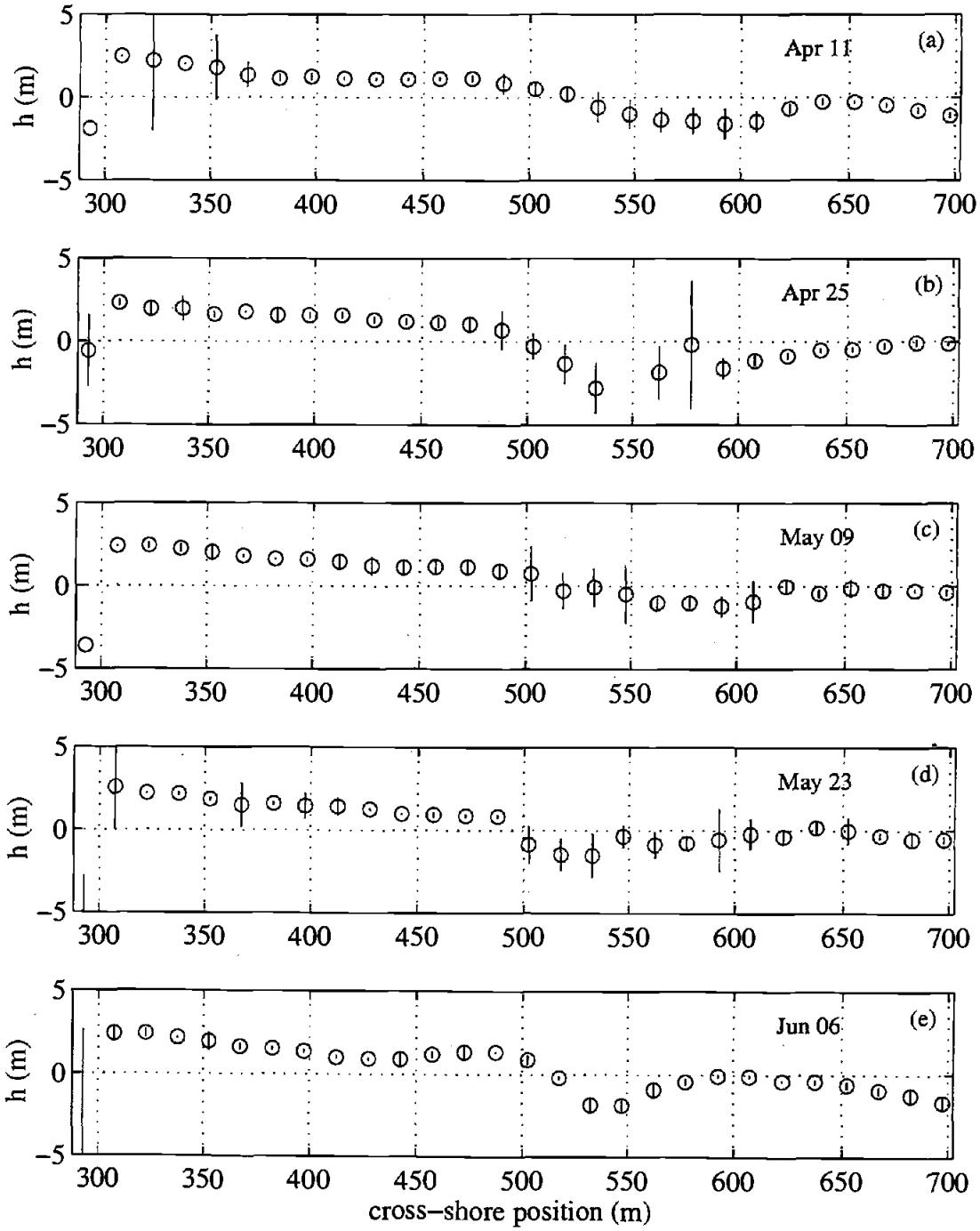

Figure 4.25 Estimated profiles at Agate Beach, Oregon from April 11 to June 6, 1997. The six profiles presented are seven-day averaged profiles calculated using the median estimated value at each cross-shore position. Error bars represent the 95% confidence interval for each estimate based on the standard deviation about the mean. The estimated beach slopes are consistent with those typically observed at the site (β=0.01).

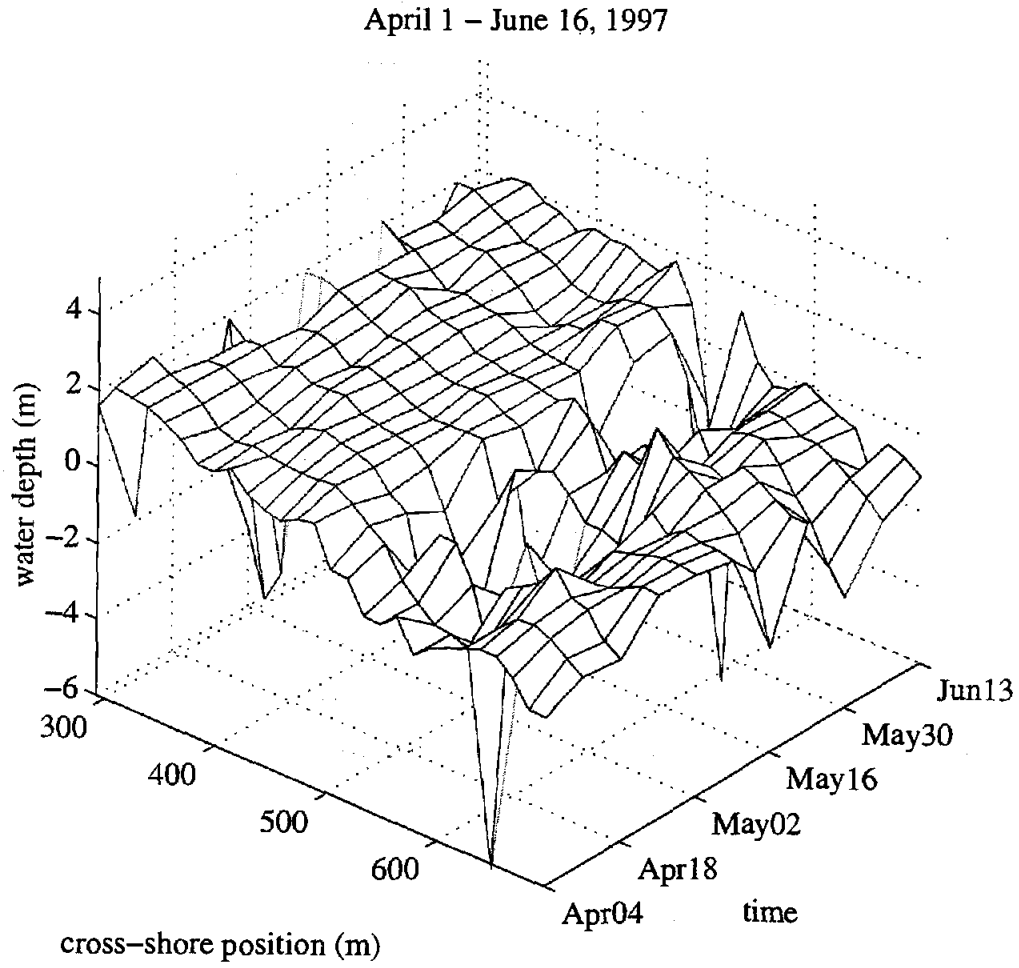

Figure 4.26 Time-space map of estimated profiles at Agate Beach, Oregon from April 1 to June 16, 1997. Estimated water depths are plotted at each cross-shore position through time. The estimated foreshore profile is very consistent and stable through the eleven week study period. Estimates are noisy and highly variable around x = 500 m.

variation is observed between x=500 m and x=600 m, perhaps due to complications associated with wave breaking and reformation over some local bathymetric feature.

To gain insight on the true profile being estimated, the rectified time exposures collected during the time of the estimates were examined. Lippmann and Holman [1989] suggest that white bands present on a ten-minute time exposure are indicative of intensified wave breaking over offshore sand bars. Figure 4.27 presents a rectified time exposure and estimated profile from April 11, 1997. An estimated offshore sand bar (x = 640 m) and a low tide terrace (x = 480 m) coincide with shallow features revealed in the time exposure. Additionally, the trough located in the estimated profile at x = 575 m coincides with an apparent trough observed in the time exposure.

Figure 4.28 presents a comparison between a rectified time exposure and the estimated profile for April 25, 1997. In this case, large error bars are present for depth estimates located between x = 515 m and x = 580 m. From the extent of white areas in the time exposure, it may be concluded that the wave heights were large during the time of this estimate. The large errors in this region are assumed to be associated with a mix of breaking and non-breaking waves in the trough during wave reformation in the trough after breaking over an offshore sand bar.

The stability of the estimates through time was investigated by looking at time slices of the map in Figure 4.26. Figure 4.29 presents the time series of water depth measured at six positions in the cross-shore, progressing from onshore (a) to offshore (f) down the page. The first plot (a) presents depths measured from a more onshore sensor location and shows remarkable stability through time. In the second plot (b), the beach is shown to gradually accrete over approximately four weeks, then remain constant for about four weeks, then slowly erode again. This pattern may be representative of gradual accretion and erosion occurring on the foreshore. The variability of water depth observed at fourth and fifth cross-shore locations appears to be more noisy; however, the estimates at these

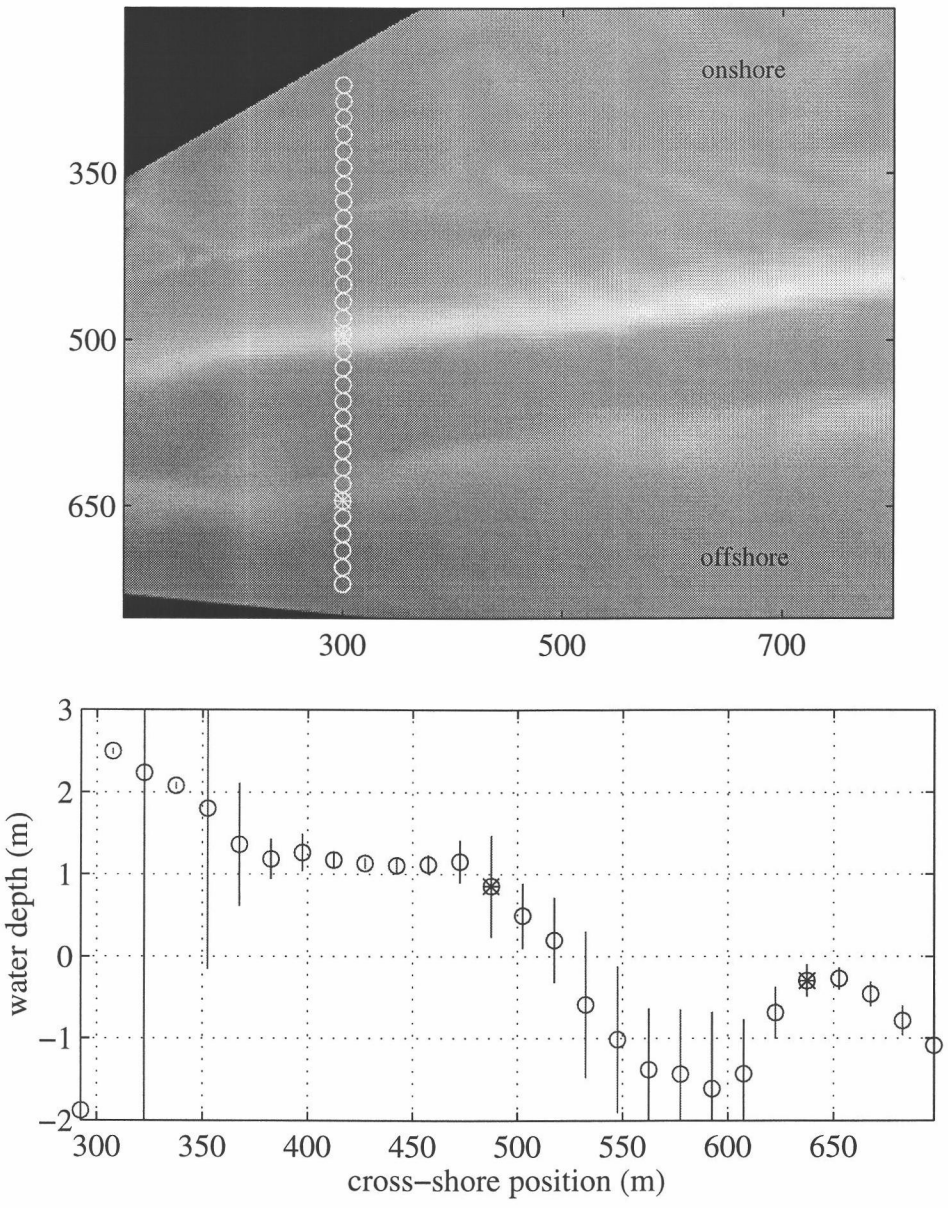

Figure 4.27 Rectified time exposure (a) and estimated profile (b) from Agate Beach, Oregon on April 11, 1997. Predicted sand bar locations coincide with sand bar locations revealed in the time exposure. Asterisks (✳) indicate co-located positions on the estimated profile and on the array shown in the rectification.

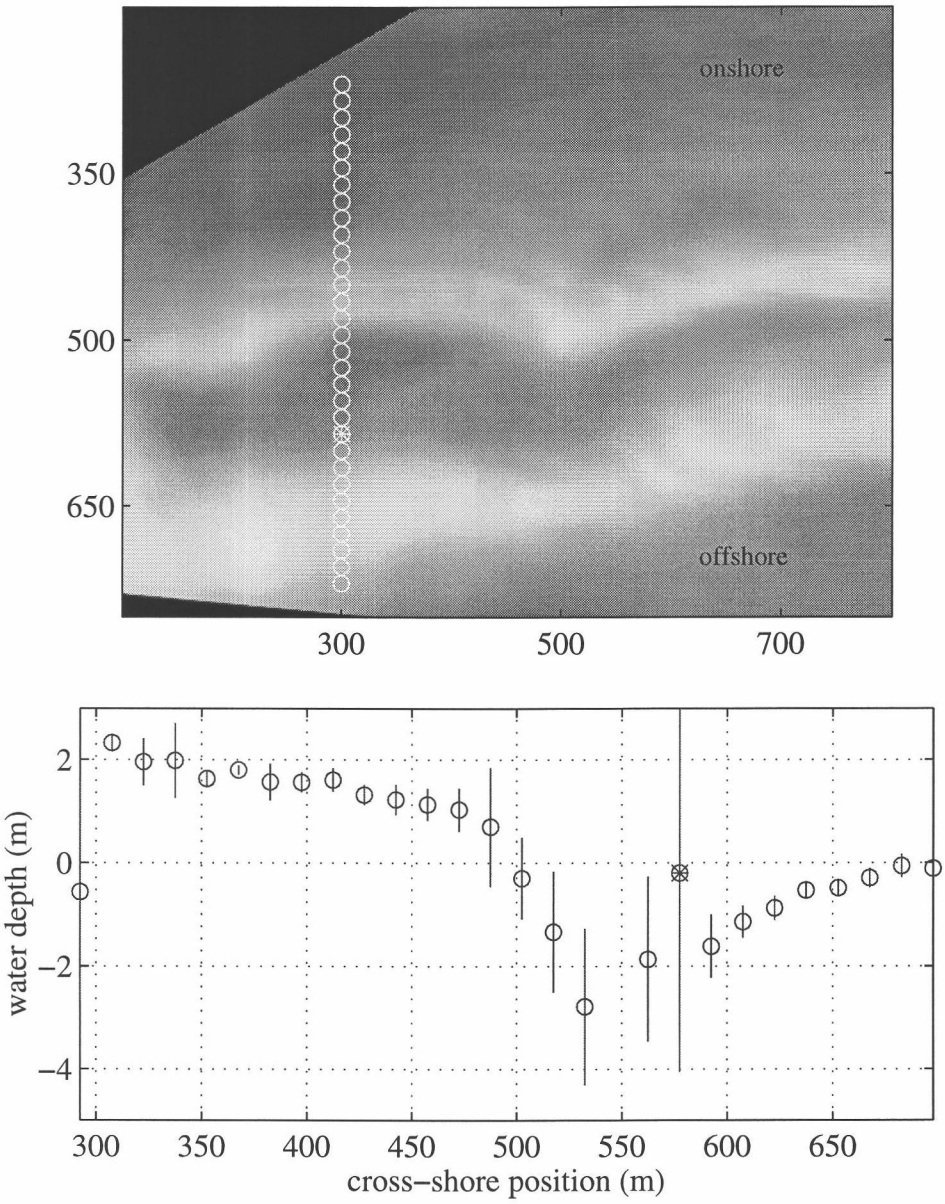

Figure 4.28 Rectified time exposure (a) and estimated profile (b) from Agate Beach, Oregon on April 25, 1997. Large error bars are associated with depths in the trough, following wave reformation after breaking on an offshore bar. The asterisk (*) indicates the co-located position of the trough on the estimated profile and on the array shown in the rectification.

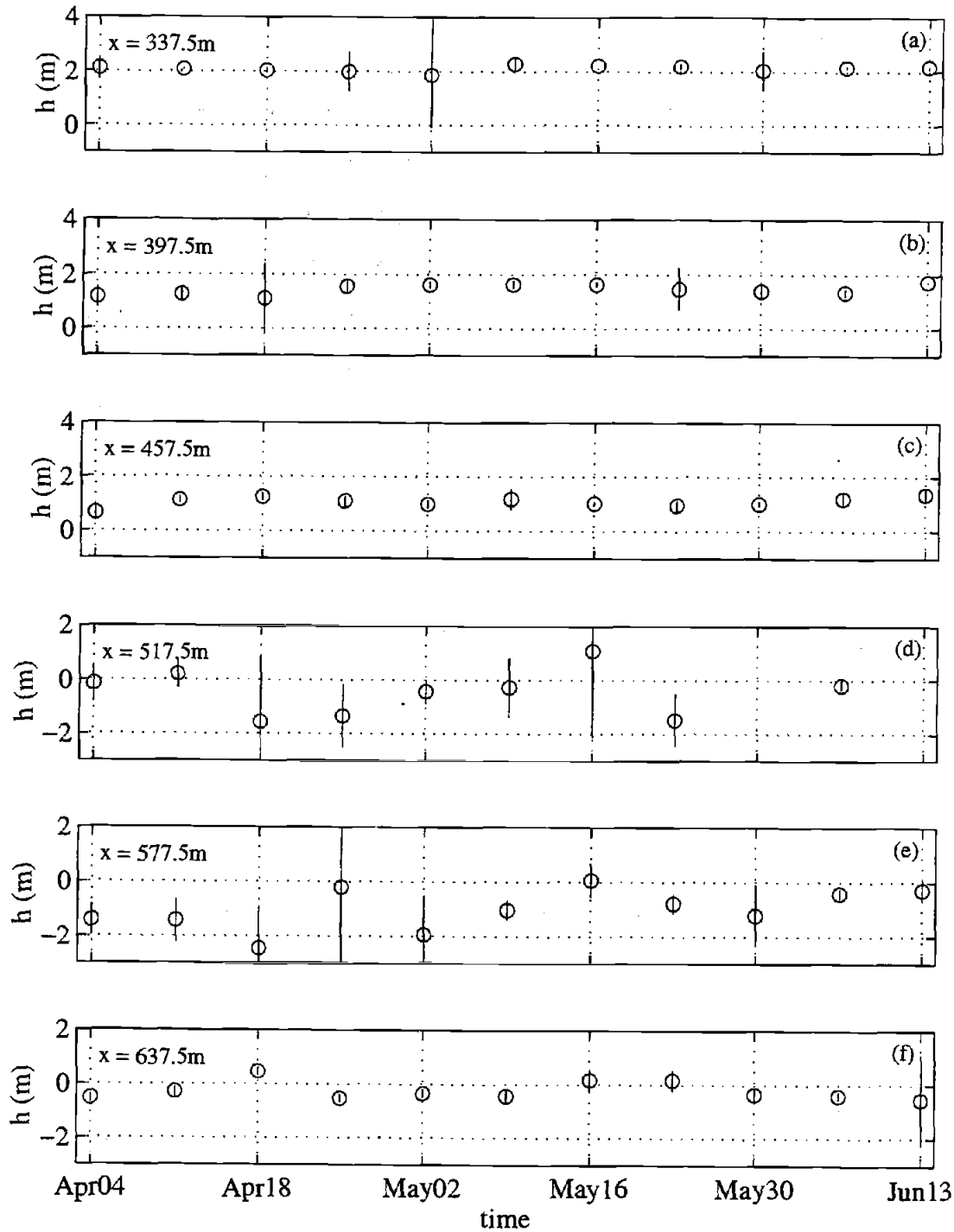

Figure 4.29 Time series of depth estimates at six cross-shore positions at Agate Beach, Oregon. Estimates with relatively small confidence intervals are shown to be more stable throughout the eleven week study period (a, b, c, and f) while those estimates with large error bars are noisy through time (d and e).

offshore locations are also associated with the largest error bars. The seaward-most location again shows smaller error bars and increased stability.

From the eleven week profile map (Figure 4.26) and the time slices (Figure 4.29), it becomes apparent that the greatest variations in the depth estimates occur where the errors bars on depth are the largest. Figure 4.30 presents a time-space mapping of the errors associated with the estimated depths for each weekly profile. The largest errors were observed around the most onshore sensors (x = 300 m to 350 m) as well as further offshore between x = 525 m and x = 600 m. Large errors at the shoreline may be attributed to the large tidal range at this site. During low stages of the tide, these points may no longer be underwater, resulting in a low number of individual depth estimates in this region. Large errors located further offshore may be attributed to wave breaking and reformation just shoreward of a sand bar visible in this location through the time exposures (Figure 4.23). In this region, the effects of finite amplitude, wave breaking and reformation, and nonlinear interactions may all serve to decrease the accuracy of the estimates.

While we do not have ground truth data for this particular site, the consistency of the results is encouraging. The ability to predict similar beach slopes and consistent water depths signifies that the technique is robust for identifying the wave phase on low sloping, high energy beaches. However, ground truth data are essential for determining the expected accuracy of the video technique under these high energy conditions.

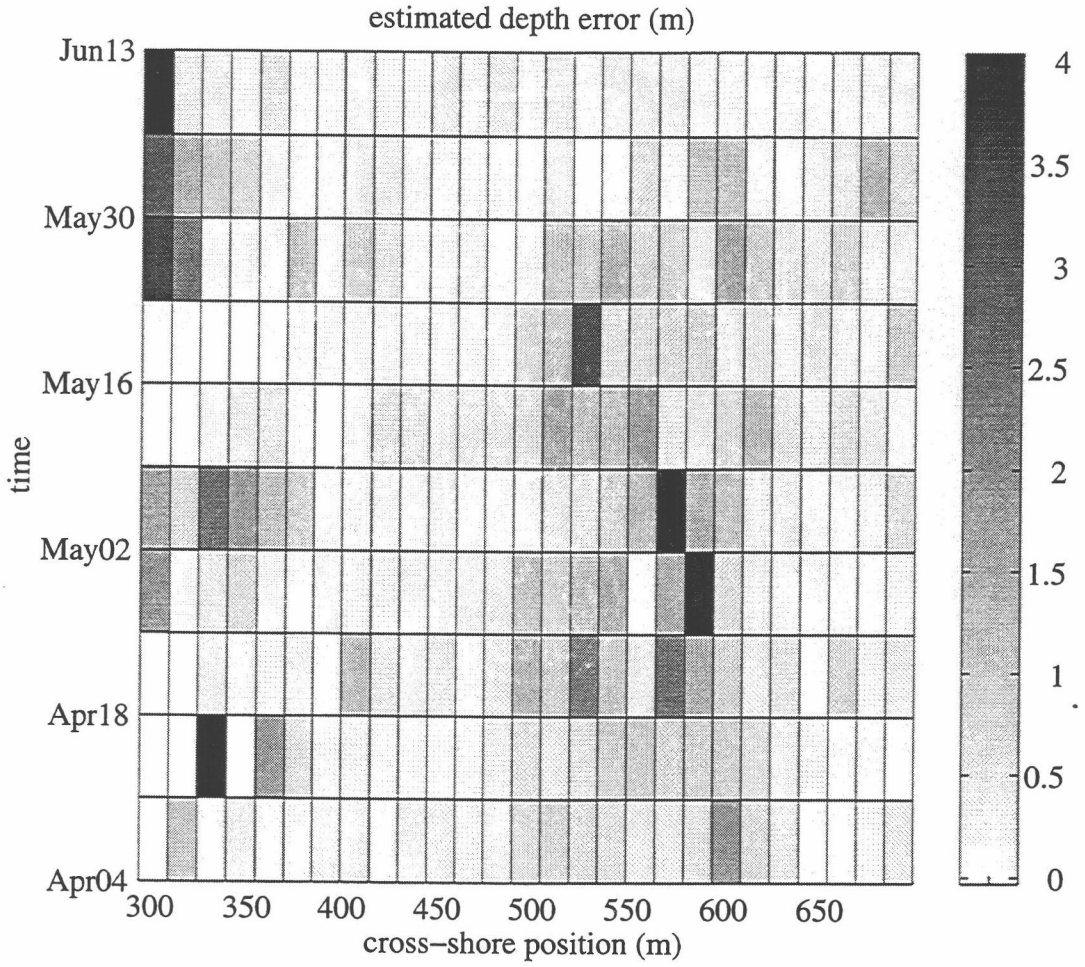

Figure 4.30 Time-space map of estimated confidence intervals at Agate Beach, Oregon from April 4 – June 13, 1997. The highest errors are found at the shoreline (x = 300 to 350 m) and in the region of the profile from x = 500 to x = 600 m.

5. DISCUSSION

The video-based technique was shown to be most accurate when the median of a suite of estimates at one particular cross-shore position was chosen as the representative water depth. Based on results of the analysis of approximately three months of data from the Duck Argus Station, the bulk weighted RMS difference error for the video technique was 0.672 m. The bulk weighted ratio error comparing estimates directly to true values was 1.34, indicating, on average, a 34% overestimation of water depth.

5.1 When to Expect Reliable Depth Estimates

The most accurate results should be obtained from the video technique when the waves are clearly visible to the video camera. The environmental conditions during the time of sampling play a large role in the collection of meaningful timestacks. Rain, fog, and poor lighting conditions all obscure the visual impression of the waves. Additionally, the angle of the sun, or time of day, plays an important role in that the sun can serve to highlight the face of wave crests making them easy to identify or alternately, at a different time of the day, to mask the signal of the waves due to a glare created on the ocean's surface.

The position of the camera contributes directly to the visibility of the waves, and hence, to the accuracy of the technique. For example, if the camera were aligned to look directly offshore, then the face of the waves becomes more obvious. In an oblique or alongshore view, as is the case with the Duck and Agate Beach Argus Stations, the camera may be oriented along-wave so that the signature of the waves becomes lost, as the wave crests are not as easily discernible from the rest of the ocean surface. Additionally, an ideal sampling scenario would involve positioning the camera relatively close to the area of interest to improve pixel resolution. For more distant cameras, pixel resolution decreases as does the accuracy of the estimation of phase speed and

bathymetry. At Duck, the pixel resolution for the cross-shore array is approximately 0.6m/pixel while the resolution at Agate Beach is slightly greater, 0.4m/pixel.

Certain wave conditions are more advantageous for use with the video technique. A clean narrow banded swell makes the task of identifying a peak frequency rather straight forward. A broad banded or directionally spread spectra contains many different wave frequencies and wavelengths, making it difficult to resolve the frequency of interest. Additionally, low amplitude waves (H<0.25 m) may be difficult to detect from long distances, especially if in the presence of superimposed wind chop. However under clean waves conditions, some low amplitude swell can be quite visible and produce very reliable depth estimates that will not be contaminated by finite amplitude dispersion effects. The environmental conditions present at during the time of sampling will play an important role in the collection of a meaningful timestack.

After the intensity timestacks have been collected and depths have been estimated using the video technique, it is important to have indicators of when the results are reliable. In section 4.2.1, three criteria were introduced for screening the data for physically impossible or statistically meaningless estimates. Depth estimations were limited only to cases where: (1) the wavenumber was negative indicating shoreward progressive waves; (2) the wavelength was less than 0.9 times the deep water wavelength; and (3) the corresponding CEOF amplitude was greater than 0.70. However, in the examples presented here, the data were not pre-selected against a number of known potential sampling problems. In the future, it may be possible to implement a number of pre-filters so that stable depth estimates can be more readily achieved.

It is first important to determine if the waves are visible to the camera. One parameter to examine would be the mean pixel intensity at each location in the array. Images with significantly low mean intensities ($\bar{I} < 25$) correspond to dark or foggy images and should automatically be excluded from all calculations.

The variance of the pixel intensity at each cross-shore position also provides an indication as to whether the waves are visible to the camera. The propagation of a wave past a single pixel location is observed through the variations in pixel intensity at that point (see section 2.3 for details). Hence, very low variance magnitudes indicate that the signal of the wave is not well defined visually and accurate estimates of wave phase will be difficult to obtain.

A final possible pre-filter for the data would be to examine the pair-wise coherence between adjacent pixel locations along the array. High coherence between two sensors within the incident band is an indication that the wave signal has been detected by the remote sensing techniques and a stable estimate of phase can then be expected.

5.2 Possible Explanations for Incorrect Estimates

There are three major reasons why the video techniques explained here may provide incorrect estimates of depth. The first is that the relationship between the wave form and the video signal of the wave may not be adequately understood or properly defined. Other possible errors may reside in the analysis techniques chosen to extract phase information from the intensity data. A third possibility is that the phase speed estimated by the video technique may be inconsistent with the theoretical expression for shallow water phase speed.

5.2.1 Video Related Error

One explanation for incorrect depth estimates may be that in some areas of the profile the remotely sensed wave signal is not truly representative of the actual wave form, for example, in the region of the profile near the break point. Here, both breaking and non-breaking waves are present, each having its own distinct visual manifestation of the true

wave. In this region, a single MTF cannot be identified to represent the signal due to the non-coherent interaction of phases from two individual MTFs.

Additional problems will arise as waves shoal and become highly nonlinear. Here, the video signal of the wave is marked by the leading crest of the wave. In this case, the phase of the MTF is not spatially stable because as the wave form evolves, the visual signature also begins to change as the crest shifts forward. Hence, the MTF may be dominated by this distinctive, leading wave crest and not faithfully describe the fundamental frequency of the true wave signal.

5.2.2 CEOF Related Error

The CEOF analysis is a robust method for determining the phase relationship across a spatial array; however, it may be sensitive to array length and sensor spacing. The CEOF fails in some regions of the profile because it is not able to detect the propagating signal at each location. Figure 5.1 shows the sensor by sensor coherence for the example from the Delilah experiment. The coherence is high towards the center of the array but drops off as the sensor spacing increases. Merrifield and Guza [1990] showed that for a fixed wavenumber band of interest, the recovery of the signal at the ends of an array reduced with increasing array length and found that the performance of the CEOF analysis depends on the spread in wavenumber relative to the array size. To obtain the most accurate results using long spatial arrays, a narrow wavenumber band should be investigated. Alternately, if a broad wavenumber band is of interest, a shorter array may be used to retain maximum coherence between the endpoints of the array. This indicates that a piecewise approach to the CEOF may be a viable alternative. By separating the array into smaller areas of interest, perhaps greater coherence can be achieved between sensors and the percentage of the variance explained by the first mode of the EOF will increase, thus increasing the accuracy of the estimates.

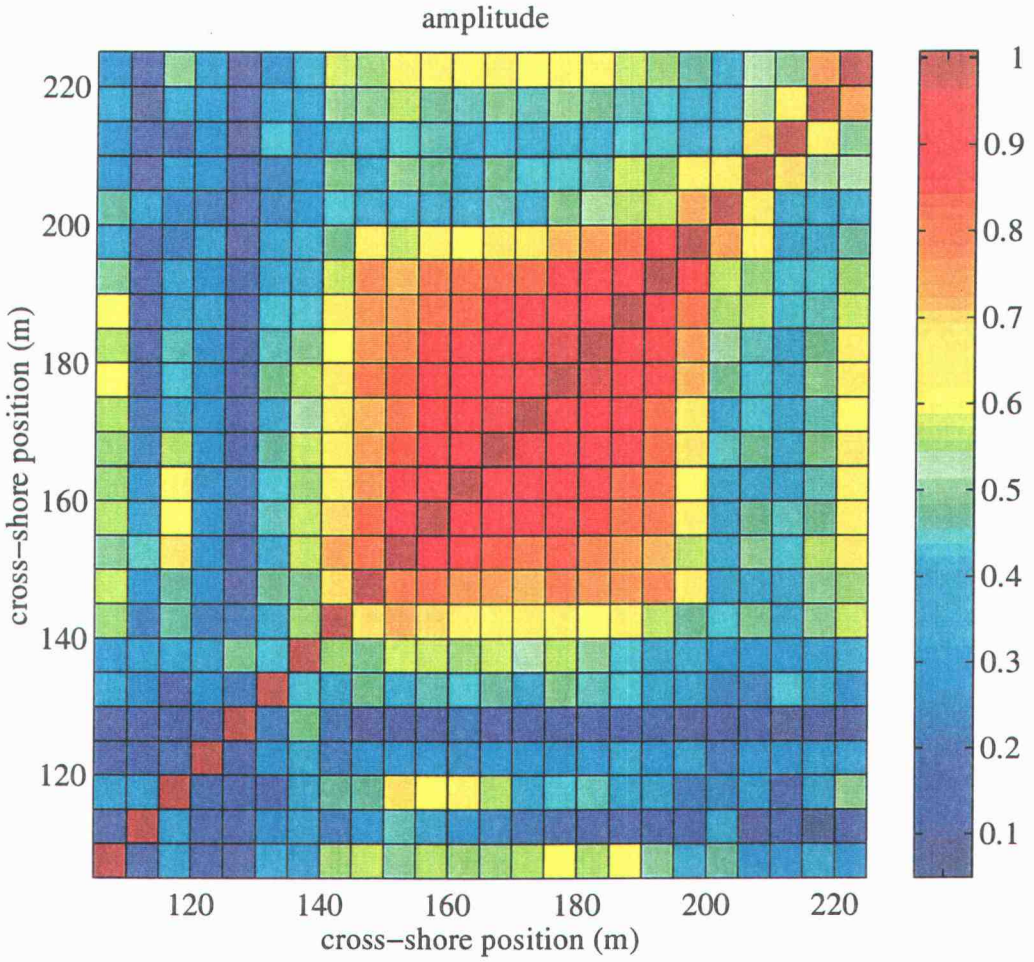

Figure 5.1 Amplitudes from the cross-spectral matrix of intensity data for October 8, 1990 in Duck, North Carolina. Amplitude values of 1 are found along the diagonal where there is perfect coherence between each sensor and itself. Amplitudes are seen to decrease for sensor spacing greater than approximately 40m. Amplitudes are also low at the ends of the array where coherence between sensors drops significantly.

5.2.3 Discrepancies Between Estimated and Theoretical Phase Speed

Another possible alternative for discrepancies between the estimated and the true profiles may be rooted in the physics of wave phase speed rather than the techniques used to measure it. In some cases, the phase speed measured using the video technique may not agree with the theoretical representation of phase speed. Phase speeds in the nearshore can be affected by many physical processes such as surface drift currents, mean flows, and rip currents [*Plant and Wright*, 1980], the directional spread of wave energy [*Huang and Tung*, 1977], and the presence of shorter waves traveling on low frequency long waves [*Phillips*, 1981].

Estimated phase speeds may also be compared to those predicted by solitary theory which accounts for the effects of finite amplitude dispersion. While linear wave theory is generally accurate within a first order approximation, some data have suggested that solitary theory may be a more appropriate and accurate estimator of phase speed at shallower locations within the surf zone [*Thornton and Guza*, 1982]. The potential errors associated with inferring water depths from linear theory (h_l) rather than solitary theory (h_s) can be calculated from equations (2.6) and (2.7) as

$$\frac{h_l}{h_s} = \frac{\left(\frac{c^2}{g}\right)}{\left(\frac{c^2}{g\left(1+H/h\right)}\right)} = \frac{\left(\frac{c^2}{g}\right)}{\left(\frac{c^2}{1.42g}\right)} = 1.42 \qquad (5.1)$$

where the ratio H/h is taken to be 0.42 in the saturated surf zone [*Thornton and Guza*, 1982]. If finite amplitude effects are significantly present, water depths estimated within the surf zone using linear theory may be wrong by a factor of 1.42. At the break point, the ratio of H/h may be as high as 0.76, resulting in larger areas in the region of breaking.

5.3 Future Work

Future field work is planned for the continued development and ground truthing of the video technique. In September 1997, additional field tests will be carried out in Duck, North Carolina as a part of the SandyDuck experiment. During this experiment, in-situ instrument arrays of pressure sensors and current meters will be deployed and detailed surveys will be collected daily by the CRAB. This will provide an excellent opportunity for obtaining ground truth for water depths estimated from timestacks collected from the Argus Station already in operation at the site.

Several changes in the sampling technique will be employed during SandyDuck. First, an offshore looking camera will augment existing views for collection of timestacks. The angle of the camera into the face of the waves will improve the visual signature of the waves.

The cross-shore pixel array will be more densely sampled using a smaller sensor spacing (i.e., dx = 2.5 m). This will allow for greater flexibility during the CEOF analysis when choosing the optimal spacing between sensors for achieving the greatest coherence. Additional cross-shore transects will be added to the pixel array design in order to examine the longshore stability of phase speed and bathymetry estimates. Depth estimates will then be compared to daily CRAB surveys to obtain greater insight on the expected accuracy.

Finally, an array of pixels will be co-located with a cross-shore array of in-situ instrumentation both inside and outside of the surf zone. Using data collected from pressure sensors or current meters, a direct comparison can be made between the video estimated phase speeds and those measured using data from the wave gauges. Using these data, the phase relationship between video data and broken waves and, especially, video data and unbroken waves can be more closely examined. Additionally, it may be possible to determine whether overestimated water depths are related to errors within the selected

analysis for the video estimation technique or to discrepancies between measured and theoretical expressions for phase speed.

6. CONCLUSION

The accuracy of the video technique for estimating water depth was tested using three sets of data from two beaches. Initial tests using Delilah data showed the RMS difference error between the estimated and true water depths for the profile on October 8, 1990 to be 0.613 m for those depths where the corresponding CEOF amplitudes were greater than 0.70. During this data run, the cross-shore region prior to wave breaking appeared to be a difficult area of the profile over which to estimate phase speed and water depth due to the changing phase relationship between the video signal and unbroken waves and the video signal and steepening, breaking waves. Averaging the depth estimates over a tidal cycle has been shown to ameliorate the problems in this transition region by shifting the breakpoint to various regions along the profile.

Timestacks collected from the Duck Argus Station allowed for the development of an automated technique and for the estimation of long term profile evolution. Weekly averaged profiles were calculated by calculating the median depth at each cross-shore position along the array. Confidence intervals were determined for each estimated depth by measuring the standard deviation of all the estimates about the mean. The weighted, time-averaged ratio error was 1.34 and the weighted RMS difference error was 0.672 m over the eleven week study period. This indicates that depth estimates are generally within 34% of the true water depth.

Using timestacks from the Agate Beach Argus Station, the stability of each profile estimate and the consistency between estimates was examined. Again, one week average profiles were calculated using the median water depth at each location and confidence intervals were determined from the standard deviation of the estimates at each location. The elevation and slope of the foreshore remained very consistent and stable through time. The foreshore slope of the estimated profiles was consistent with beach slopes previously observed at the site (β=0.01). Additionally, comparisons of the estimated profiles to the

locations of sand bars present in the rectified time exposures from the same day suggest that the topography revealed in the estimates may be a good first order approximation of the offshore profile. The estimated depths at cross-shore positions where the error bars were small (~0.3m or less) were relatively stable through time. These results indicate that the technique is capable of producing consistent and reasonable results on high energy beaches. However, ground truth data are essential for critically evaluating the performance and establishing the accuracy of the technique.

The preliminary results of this technique are promising. They demonstrate that an array of pixel locations can be used similarly to an array of in-situ wave gauges to gather information on wave phase. They also show that remotely-sensed video data can be used as an alternate to traditional surveying methods for obtaining a first order approximation of nearshore bathymetry. Additional work is needed to increase the accuracy and reduce the associated error bars before the estimated profiles can be used as data for nearshore modeling or in shoreline/profile monitoring programs. However, the results presented in this thesis provide reason to continue work on developing this technique and encouragement that it will provide a useful tool for nearshore oceanographers and coastal managers.

BIBLIOGRAPHY

Bascom, W., *Waves and Beaches*, Anchor Books, Garden City, N.Y., 1954.

Bendat, J. S. and A. G. Piersol, *Random Data: Analysis and Measurement Techniques*, 2nd ed., 566 pp., Wiley-Interscience, New York, 1986.

Birkemeier, W. A., K. K. Hathaway, J. A. Smith, C. F. Baron and M. W. Leffler, DELILAH experiment: Investigator's summary report, Coastal Engineering Res. Center, Field Res. Facil., U.S. Army Eng. Waterw. Exp. Sta., Vicksburg, MS, 1991.

Birkemeier, W. A. and C. Mason, The CRAB: A unique nearshore surveying vehicle, *Journal of Survey Engineering*, *110*, 1-7, 1984.

Brillouin, L., *Wave Propagation and Group Velocity*, Academic Press, New York, 1960.

Bryan, K. R. and A. J. Bowen, Edge wave trapping and amplification on barred beaches, *J. Geophys. Res.*, *101*(C3), 6543-6552, 1996.

Davis, J. C., *Statistics and Data Analysis in Geology*, 550 pp., John Wiley & Sons, Inc., New York, 1973.

Elgar, S. and R. T. Guza, Shoaling gravity waves: Comparisons between field observations, linear theory, and a nonlinear model, *J. Fluid Mech.*, *158*, 47-70, 1985.

Fuchs, R. A., Depth determination on beaches by wave velocity methods, *74,1*, University of California, Berkeley, 1953.

Gonzales, R. C. and R. E. Woods, *Digital Image Processing*, 716 pp., Addison-Wesley Publishing Company, Inc., Reading, 1992.

Holland, K. T., R. A. Holman, T. C. Lippmann, J. Stanley and N. Plant, Practical use of video imagery in nearshore oceanographic field studies, *IEEE Journal of Oceanic Engineering*, *22*(1), 81-92, 1997.

Holland, K. T., B. Raubenheimer, R. T. Guza and R. A. Holman, Runup kinematics on a natural beach, *J. Geophys. Res.*, *100*(C3), 4985-4993, 1995.

Holman, R. A. and A. J. Bowen, Edge waves on complex beach profiles, *J. Geophys. Res.*, *84*(C10), 6339-6346, 1979.

Holman, R. A., A. H. Sallenger, T. C. Lippmann and J. W. Haines, The application of video image processing to the study of nearshore processes, *Oceanography*, 6(3), 78-85, 1993.

Huang, N. E. and C. C. Tung, The influence of the directional energy distribution on the nonlinear dispersion relation in a random gravity wave field, *J. Phys. Oceanogr.*, *7*, 403-414, 1977.

Komar, P. D., *Beach Processes and Sedimentation*, 429 pp., Prentice-Hall, Englewood Cliffs, N.J., 1976.

Lippmann, T. C. and R. A. Holman, Quantification of sand bar morphology: A video technique based on wave dissipation, *J. Geophys. Res.*, *94*(C1), 995-1011, 1989.

Lippmann, T. C. and R. A. Holman, The spatial and temporal variability of sand bar morphology, *J. Geophys. Res.*, *95*(C7), 11,575-11,590, 1990.

Lippmann, T. C. and R. A. Holman, Phase speed and angle of breaking waves measured with video techniques, in *Coastal Sediments, '91*, Edited by N. Kraus, pp. 542-556, ASCE, New York, 1991.

Longuet-Higgins, M. S., Longshore currents generated by obliquely incident waves, 1, *J. Geophys. Res.*, *75*, 6778-89, 1970.

Lynch, D. K. and W. Livingston, *Color and Light in Nature*, 245 pp., Cambridge University Press, Cambridge, 1995.

Merrifield, M. A. and R. T. Guza, Detecting propagating signals with complex empirical orthogonal functions: a cautionary note, *J. Phys. Oceanogr.*, *20*, 1628-1633, 1990.

Oltman-Shay, J. and P. A. Howd, Edge waves on nonplanar bathymetry and alongshore currents: a model and data comparison, *J. Geophys. Res.*, *98*(C2), 2495-2507, 1993.

Phillips, O. M., The dispersion of short wavelets in the presence of a dominant long wave, *J. Fluid Mech.*, *107*, 465-485, 1981.

Plant, N. G. and R. A. Holman, Intertidal beach profile estimation using video images, *Mar. Geol.*, in press.

Plant, W. J. and J. W. Wright, Phase speeds of upwind and downwind traveling short gravity waves, *J. Geophys. Res.*, *85*(C6), 3304-3310, 1980.

Suhayda, I. N. and N. R. Pettigrew, Observations of wave height and wave celerity in the surf zone, *J. Geophys. Res.*, *82*(9), 1419-1424, 1977.

Thornton, E. B. and R. T. Guza, Energy saturation and phase speeds measured on a natural beach, *J. Geophys. Res.*, *87*(C12), 9499-9508, 1982.

Wallace, J. M. and R. E. Dickinson, Empirical orthogonal representation of time series in the frequency domain, Part I: Theoretical considerations, *J. Appl. Meteorol.*, *11*(6), 887-892, 1972.

Whitford, D. J. and E. B. Thornton, Longshore current forcing at a barred beach, in *21st Coastal Engineering Conference,* ASCE, Tourmellinos, 1988.

Wiegel, R. L. and R. A. Fuchs, Wave velocity method of depth determination for non-uniform short crested wave systems by aerial photography, *74, 9*, University of California, Berkeley, 1953.

Wright, L. D. and A. D. Short, Morphodynamic variability of surf zones and beaches: A synthesis, *Mar. Geol.*, *56*, 93-118, 1984.